Development of Modified ZrO2 Catalysts for the Production of Levulinic Acid Esters

Von der Fakultät für Mathematik, Informatik und Naturwissenschaften der RWTH Aachen University zur Erlangung des akademischen Grades eines Doktors der Naturwissenschaften genehmigte Dissertation

vorgelegt von

M.Sc. Wirawan Ciptonugroho

aus Jakarta, Indonesien

Berichter: Universitätprofessorin. Dr.rer.nat. Regina Palkovits

Professor. Dr. Johannes H Bitter

Tag der mündlichen Prüfung: 30.03.2017

Diese Dissertation ist auf den Internetseiten der Universitätsbibliothek online verfügbar.

I hereby declare, that I have written this work independently and have used only the specified sources and resources. The work has not been presented to any examining office, but parts of the work have already been published in scientific journals or as conference contribution (see "List of Publications").

Versuche nicht ein Erfolgreicher,

sondern ein wertvoller Mensch zu sein

(*Janganlah berusaha untuk menjadi seorang yang sukses,*

melainkan jadilah seorang yang berharga)

Albert Einstein

ACKNOWLEDGMENT

ABSTRACT

WO$_x$/ZrO$_2$ catalysts have been synthesized with different tungsten loadings and calcination temperatures via one-pot evaporation induced self-assembly (EISA) technique. The tungsten contents and calcination temperatures greatly influence the textural properties of the material. The crystallinity and surface state of materials are confirmed by X-ray diffraction and Laser Raman spectroscopy. The surface acidity of the materials are evaluated by NH$_3$-temperature programmed desorption (NH$_3$-TPD) and diffuse reflectance Fourier transform (DRIFT) with adsorbed pyridine. The catalysts containing 20-25 wt%. WO$_3$ demonstrate the highest surface acidity and population of Brönsted acid centers. The activity of catalyst was tested for Levulinic acid (LA) esterification with 1-butanol (1-BuOH) with mole ratio 2 to 1. The only products after the reaction are pseudo- (*p*-BL) and normal-butyl levulinate (*n*-BL). The highest total yield of esters (67%) and selectivity towards *n*-BL (97%) can be attained over 20 wt.% WO$_x$/ZrO$_2$ catalyst calcined at 800 °C. A strong correlation between the population of Brönsted acidity and catalytic activity could be affirmed.

The second part of this work elaborates the production of levulinic esters via addition reaction of alpha-angelica lactone (a-AL) with 1-BuOH over Amberlyst-36. Full conversion with 97% selectivity towards the ester can be achieved by performing the reaction with stoichiometric amount of the reactants at a milder condition. The reaction mechanism for the ester formation has been confirmed revealing that *p*-BL is the intermediate during the transformation of a-AL to *n*-BL. Different alcohols have also been studied suggesting the effect of linearity and the length of alkyl chain influence the reaction. This study eventually indicates that a-AL can be used as a better candidate to substitute LA for the synthesis of levulinic acid esters. Different type solid acid catalysts have been tested suggesting that strong acidity is required to allow the addition reaction.

Despite possessing strong acid sites, not all acid catalyst can apparently catalyze the addition reaction. The third part of this work is intended to examine the influence of acid species on the addition of a-AL. To realize the investigation, WO$_x$/ZrO$_2$ with adjustable Brönsted population was prepared via EISA and impregnation route. Both methods result in the catalyst with similar textural properties. Raman spectroscopy and X-ray diffraction demonstrated that catalysts prepared by EISA are able to retain meta-stable tetragonal phase of ZrO$_2$ as well as delay the development of WO$_3$ nanoparticles. NH$_3$-TPD and DRIFT with adsorbed pyridine were employed to evaluate the surface acidity. The spectra from pyridine adsorbed at 150°C reveal that the highest Brönsted acid concentration occurs at 15 and 20 wt.% WO$_3$ for the catalysts prepared by impregnation and EISA respectively. The catalysts were employed in the addition reaction of a-AL with 1-BuOH. The conversion of a-AL and selectivity towards *n*-BL depend strongly on the concentration of Brönsted acid sites. Finally the materials prepared by impregnation method shows higher catalytic activity.

Contents

NOMENCLATURE

EISA	:	Evaporation induced self-assembly
ρ_W	:	W surface density [W-atom/nm^2]
LA	:	Levulinic acid
1-BuOH	:	1-butanol
LAE	:	Levulinic acid esters
n-BL	:	normal-butyl levulinate
p-BL	:	pseudo-butyl levulinate
TOF$_{eff}$	:	Effective turn over frequency
WZr	:	WO_x/ZrO_2
SZr	:	SO_4/ZrO_2
WmZrO2	:	$WO_x/mesoporous\text{-}ZrO_2$
WO$_3$-NPs	:	WO_3 nanoparticles
a-AL	:	α-angelica lactone
b-AL	:	β-angelica lactone
g-BL	:	γ-methylene-γ-butyrolactone
g-VL	:	γ-valero lactone
2,4-PDA	:	2,4-pentadionic acid
k	:	Reaction rate constant

Chapter. 1 Introduction

1.1 Acid catalysis

1.1.1 Catalysis (general)

Nowadays, the application of catalysts has been inevitable in our daily life. Close examples are naturally occurring catalysts so called enzymes needed to speed up digestion and metabolism processes in a human body at a relatively low temperature. The enzyme ptyalin is found in human saliva allowing hydrolyzing starch to glucose which can be further absorbed by intestinal walls before being distributed through the blood stream to other parts of the human body. Adenosine tri-phosphate (ATP) known as fuel for the cell metabolism is formed by catalyzing adenosine di-phosphate (ADP) and inorganic phosphate in the presence of ATP-synthase. In the absence of these catalysts, the digestion and metabolism would never happen. Beside facilitating the processes inside the human body, the production of food commodities like wine, cheese, yogurt, soy bean sauce, etc. have long been relying on the principles of catalysis. For instance in the wine processing, glucose extracted from the fruit juice is catalytically transformed by yeasts containing zymase to alcohol and CO_2.

In present time catalysts are involved in the manufacture of ca. 85% of all chemical products from which 90% are catalyzed by heterogeneous catalysts [1]. Heterogeneous catalysts are preferably from the homogeneous ones since they are readily separated from the products mixture by centrifugation and filtration while homogeneous catalysts are harder to recover causing a high cost of separation units and more complex process design. As for heterogeneous catalysis, many processes rely on metal elements to accelerate the reaction rate. For instance NH_3 is synthesized by combining N_2 and H_2 in the presence of promoted iron (Fe) catalysts through the famous Haber-Bosch process [2]. Fe based catalysts are also commercially applied i.e. by SASOL in the high temperature Fischer-Tropsch synthesis (HTFT) to produce liquid alkanes from syngas (CO and H_2) [3,4]. Moreover, noble metals such as Pt have massively been employed in many industrial applications stretching from hydrocarbon processing [5,6], environmental protection [7,8] up to biomass conversion

[9,10]. In addition to metal catalysts, acid catalyzed reactions also play a key role in industrial processes [11,12]. The most popular example relates to fluid catalytic cracking (FCC) units used to immensely manufacture gasoline from long-chain and high boiling point hydrocarbons [13]. The FCC units presently use acidic FAU- or Y-zeolites to boost the gasoline yield. Acidic-zeolite catalysts are also applied to perform hydrocracking, hydration, methanol to gasoline, aromatization, alkane isomerisation, methylamine synthesis etc. [14]. Other types of solid acids such as sulfonated resins, silica-alumina phosphate, niobic acid, SO_4^{2-}/ZrO_2 (SZr) and heteropolyacids have already found their applications in commercial processes [15]. One of the most intriguing catalysts is the highly acidic SZr catalyst which was firstly developed in 1962 [16]. According to Hammet acidity scale it is suggested that its acidity approaches $H_o \leq 14$ which is more acidic than sulfuric acid. Accordingly, this catalyst can be used for alkane isomerisation. Despite its strong acidity, SZr suffers severe deactivation due to the formation of H_2S and SO_x during reaction and regeneration. The deactivation can be considerably overcome by introducing metal elements such as Pt [17,18]. In hydro-isomerisation, Pt not only acts as a stabilizer but also splits H_2 gas to surface atomic H^+ which can enhance the acidity [19]. Other effort have been conducted by many researchers to improve the stability of this catalyst by replacing sulfate active species with more stable elements. In 1987, Hino and Arata discovered WO_x/ZrO_2 (WZr) as a suitable substitution for SZr [20]. In their report, WZr possesses comparable acidity ($H_o \leq 14$) to SZr. Interestingly, WZr is considerably more stable compared to the predecessor, SZr, leading to intense research interest in WZr for acid catalyzed reactions.

1.1.2 ZrO$_2$ based heterogeneous catalysis

Zirconia (ZrO_2) is a polymorphic white crystalline ceramic material possessing a high tensile strength, high hardness, and resistance to corrosion. ZrO_2 consists of three different crystal phases namely monoclinic, tetragonal and cubic. The cubic phase occurs at very high temperatures (>2370 °C). The tetragonal phase exists in the temperature range of 1150 - 2370 °C. Meanwhile, monoclinic ZrO_2 is the most stable crystal phase at low temperatures (<1150 °C). Despite the usually required high temperatures to obtain tetragonal or cubic zirconia, in fact these phases can also coexist with monoclinic zirconia at low temperatures. Many hypotheses have been made concerning this fact. Livage suggested that amorphous

ZrO_2 has a similar local structure to tetragonal crystals causing a partial evolution of the tetragonal phase upon heating of amorphous ZrO_2 [21,22]. Garvie revealed that for a crystal size lower than 30 nm, tetragonal ZrO_2 is favorable because of its lower surface energy [23]. Chuah also confirmed that small ZrO_2 particles prepared via a hydrolysis method at higher temperatures contained mostly the tetragonal phase [24]. Moreover, each crystal phase of ZrO_2 has different volumes potentially leading to crack propagation during phase transformation at high temperatures. Therefore, ZrO_2 is usually stabilized by further elements resulting in a more stable crystal structure. In this case ytrria (YSZ) is normally introduced as a dopant. Because of its exceptional mechanical properties combined with inert characteristics, YSZ can be used for restorative purposes in clinical applications [25,26] and furnace coatings [27]. YSZ can potentially be employed for membrane application due to its resistivity to alkaline environments [28]. The high ionic conductivity of YSZ makes it suitable for solid oxide fuel cells as well as O_2 sensor [29].

In addition to mechanical, thermal and electrical properties of ZrO_2, surface properties of ZrO_2 have also attracted huge attention particularly in the field of catalysis. Bare ZrO_2 is amphoteric possessing Lewis acidity and basicity on the surface. The evolution of those species originates from the appreciable number of unsaturated Zr^{4+} and O^{2-} on the surface, which in turn is dependent on its crystal structures. Pokrovski et al observed that monoclinic ZrO_2 demonstrated a higher CO_2 and CO adsorption capacity than tetragonal ZrO_2 pointing at more Lewis acidity and basicity on monoclinic crystals [30]. A similar finding was obtained by Jung et al revealing that monoclinic ZrO_2 desorbed a higher number of NH_3 molecules per m^2 compared to the tetragonal one [31]. The addition of 5 mol.% Zr^{4+} is also known to considerably enhance the acidity of MCM-41 showing its exceptional activity in isopropanol dehydration and 1-butene isomerization compared to the bare MCM-41 and 5 mol.% Al-MCM-41 [32]. Applying hydrolysis method, Chuah et al successfully synthesized ZrO_2 nanoparticles possessing tetragonal phase with significantly high surface area and acidity [24]. The improvement in surface acidity can be due to the formation of considerably smaller crystallites with more exposed Zr^{4+} on edges and corners leading to the development of stronger Lewis acid centers. The acidic nature of ZrO_2 has been reported being able to initiate isomerization of 1-butene and dehydration of sec-butanol [33]. The formation of 1-butene and ammonia from butanamine was the highest over ZrO_2 compared to La_2O_3, MgO

and ZnO, respectively. Beside its acid-base features, Tanabe pointed out that ZrO_2 has an oxidative ability by generating a radical cation of tryphenyl-amine [34]. ZrO_2 is also active in the formation of nitrobenzene anion radicals demonstrating its reductive ability [35,36].

Altough pure ZrO_2 is active as a catalyst, it has been widely applied as a support for active metals. PdO/ZrO_2 facilitated a very high yield and selectivity towards acetic acid from ethanol oxidation in comparison with PdO/Al_2O_3 [37]. This exceptional activity is caused by the role of ZrO_2 in creating and retaining the spillover of surface oxygenates species preventing them from being completely oxidized. Moreover, ZrO_2 can also interact with the supported metals to alter their catalytic selectivity. Sato et al investigated the catalytic activity of Cu impregnated on different phases of ZrO_2 for ethanol dehydration [38]. Cu/tetragonal ZrO_2 caused the formation of a high fraction of acetaldehyde and methyl-ethyl ketone (MEK) in line with the existence of strong Lewis acid sites and a slight basicity; whereas, the ability of monoclinic ZrO_2 to retain Cu^{2+} resulted in significant formation of ethyl-acetate. The role of ZrO_2 as support is also noted considering the ability of Au/ZrO_2 to selectively catalyze oxidative-esterification of furfural with methanol to methyl-2-furonate at room temperature [39]. ZrO_2 is able to produce well dispersed fine Au nanoparticles which can mutually interact with the methoxy group of methanol by forming a bridge of methoxy species at the perimeter between ZrO_2 support and the Au particle responsible to its superior activity. For Ni/ZrO_2 catalysts, the higher population of oxygen defects over monoclinic ZrO_2 enhanced its activity in hydrodeoxygenation of stearic acid [40].

In addition to active metals, ZrO_2 has vastly been utilized to immobilize SO_4^{2-} anions, which are able to generate exceptionally strong acid sites. A comprehensive review concerning the applications of SO_4/ZrO_2 (SZr) for organic synthesis has been reported by Reddy [41]. Pt promoted SZr catalyst has been employed for C4-C6 paraffin isomerization in an industrial scale by Süd Chemie (now Clariant) [12]. Conventionally, SZr is prepared via sulfatation of amorphous $Zr(OH)_4.xH_2O$ with sulfur compounds such as H_2SO_4, $(NH_4)_2SO_4$, H_2S and SO_2 followed by calcination at certain temperatures. Several investigations showed that SZr calcined at 500 – 600 °C exhibited the optima in acidity and activity [42,43]. A one pot sol-gel route allowed preparing SZr with a homogeneous dispersion of active sites and higher specific surface area, which can hardly be achieved by conventional impregnation [44–46]. The textural properties of SZr can be tailored further by adding organic templates during

synthesis leading to the formation of larger pore opening, which is advantageous for catalysis [47–50]. Furthermore, the resulting ZrO_2 crystal is highly influenced by the existence of SO_4^{2-} ions. The addition of SO_4^{2-} anions can reduce the particle size. Consequently, the unstable tetragonal phase will be predominately present in ZrO_2 even at low temperatures. Indeed, the presence of anions can delay the particle growth during calcination. However, stabilized tetragonal zirconia can be transformed to monoclinic zirconia at a harsh calcination temperature of 800 °C due to sintering and agglomeration [51]. Although tetragonal ZrO_2 is reported to be less acidic compared to monoclinic zirconia, the presence of SO_4^{2-} ions appreciably increases its acidity. Ward et al suggested that a SO_4^{2-} ion attached on a Zr atom can increase the ability of the adjacent Zr atoms to donate the proton [52]. In line, strong Brönsted acidity is generated. In contrast, a less coordinated Zr atom has a tendency to withdraw electrons, which is a characteristic of Lewis acidity as illustrated in Figure 1-1. One of the most crucial problems of using SZr is the instability during reaction and regeneration. During reaction, H_2S is produced by SO_4^{2-} reduction accompanied by coke production due to the formation of aromatics via dehydrogenation [12]. The carbon deposits covering the catalyst have to be removed via combustion with air oxygen accompanied by the conversion of SO_4^{2-} to SO_2. The addition of Pt on SZr (Pt-SZr) catalyst can facilitate H_2 spillover which is able to reduce and remove carbonaceous deposit on the surface leading to higher catalyst stability. Additionally, Ebitani et al proposed that the dissociative H atom on Pt surface could migrate and transfer an electron to the Lewis acid sites (unsaturated Zr^{4+}) to form H^+ responsible to the enhanced Brönsted acidity [53,54]. Despite more stable SZr catalysts can be obtained by Pt doping, suitable alternatives possessing higher stability and facilitated regeneration are desirable.
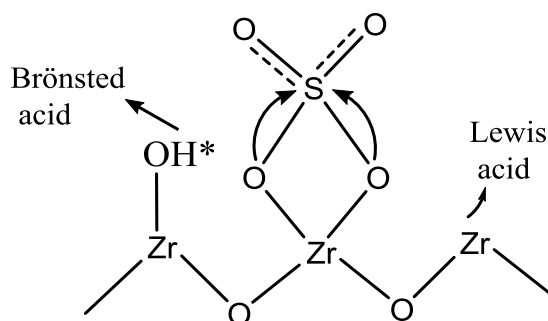
Figure 1-1 Acidity of sulfated zirconia catalysts

WO_x/ZrO_2 (WZr) is among the promising candidates to replace highly acidic SO_4^{2-}/ZrO_2 catalysts. A strongly bond WO_x overlayer on zirconia is expected to prevent the loss of active species during reaction and regeneration. This catalyst has been reported being exceptionally active and stable even under aqueous condition for bromination of phenol [55]. The acidity of WZr was evaluated by Hino and Arata showing that it has a Hammet acidity function (H_0) lower than -14.52 associated to strong acidity [20]. Scheithauer et al further investigated the acidity of 8.6 wt.% WZr by carrying out CO-adsorption [56]. It was found that a shift of the O–H IR stretching band to higher wavelength occurs which was similar to what has been found in SZr catalysts. Surprisingly, compared to H-ZSM5 the band shifts only half as much wavenumbers indicating that WZr possess only moderate acidity [56,57]. Ko et al tested WZr catalysts for n-butane hydroisomerization and observed negligible deactivation after 100 min of time on stream [58]. In contrast, SZr suffered severe deactivation caused by the formation of H_2S under identical reaction conditions [52]. The acidity of WZr can be generated by the formation of poly-WO_x domains covering the ZrO_2 support. A strong correlation between surface acidity and WO_x coverage exists and is expressed in the theoretical surface W density (ρ_W). ρ_W expresses the theoretical number of W atom covering 1 nm^2 catalyst surface assuming homogeneous dispersion. ρ_W can be adjusted by varying WO_3 concentration and calcination temperatures. Using UV-vis absorption spectroscopy, Barton classified three different growth steps of WO_x species on ZrO_2 supports [59]. At low ρ_W, a constant absorption edge energy (AEE) of 4.1 eV was observed associated to isolated monotungstic species. The constant absorption energy also reveals that monotungstates keep existing on the surface although the population of WO_x increases within this low ρ_W region. Raman spectra of low ρ_W show no intensity for the band at 834 cm^{-1} assigned to W–O–W bonds [57,60]. Concerning reducibility, WZr with a low W dopant concentration (2.2 wt.%) exhibits a single broad reduction peak at 927 °C reflecting the reduction of strong W–O–Zr bonds to yield elemental W. Thus the results of Raman spectroscopy and H_2-TPR support the fact that at low W coverage predominately monomeric tungstates are present. Thereafter, as the population of monotungstate grows reaching an intermediate range, a gradual decline of AEE from 4.1 to 3.6 occured implying that electrons delocalize from a W atom to neighboring W atoms providing sites for hosting the protons. This means that the W–O–W network expands as a consequence of monotungstate

polymerization. According to the Hückel calculation, a decrease of AEE can be a hint for an expanding interconnected network of metal oxides [61]. In the intermediate loading, Raman spectra show a band at 834 cm^{-1} (W–O–W stretching mode) evolving together with a band at around 890 cm^{-1} designated to W = O bonds in hydrated poly-WO$_x$ species. The band at 890 cm^{-1} shifts progressively to higher frequencies together with an increased intensity of the band at 834 cm^{-1} as a consequence of increased ρ_W [56]. The development of extended W–O–W networks enhances the reducibility via the formation of an additional broad peak between 520 and 920 °C assigned to the stepwise reduction of poly-WO$_x$ species [62]. The expansion of over layer species eventually achieves saturation when the ZrO$_2$ surface is completely coated with WO$_x$, which is defined as theoretical monolayer coverage. Any WO$_3$ loadings beyond monolayer coverage will give rise to crystallite monoclinic WO$_3$ particles. The formation of WO$_3$ particles results in low AEE, which is usually located lower than 3.6 eV. Interestingly, this value remains constant at any WO$_3$ concentration. Constant AEE (around 4 eV) at ρ_W higher than complete coverage were also observed by Wachs' and co-workers [60]. The appearance of WO$_3$ nanoparticles can be recognized by the presence of distinct Raman bands at 800 cm^{-1} and 715 cm^{-1}. Those bands grow in intensity with WO$_3$ concentrations indicating the intensification of WO$_3$-NPs formation [56,57,60].

WZr is assumed to exhibit the highest acidity when the ZrO$_2$ surface is completely hidden because the saturation capacity of the 2D over layer poly-WO$_x$ species is attained. It should be noted that above complete monolayer coating, the extensive formation of WO$_3$-NPs negatively affects on acidity and activity since the formation of larger particles buries accessible active WO$_x$ species. Investigating CO adsorption over WZr in FTIR, Scheithauer et al were able to identify the occurrence of Brönsted and Lewis acid sites on WZr catalysts [57]. At low ρ_W, Lewis acidity predominates the surface due to a high number of exposed unsaturated Zr^{4+} atoms. Moreover, the electron withdrawing effect by adjacent WO$_x$ units strengthens the Lewis acid sites [56]. Upon increased ρ_W, the number of exposed Zr^{4+} shrinks and the sites are covered by the expansion of over layer WO$_x$ leading to the development of Brönsted acid sites. The rise of Brönsted acid centers continues until the entire surface of ZrO$_2$ is shielded by a monolayer of poly-WO$_x$ species. According to Raman spectroscopy, increased ρ_W results in a Raman shift from 980 to 1001 cm^{-1} accompanied by an increasing intensity associated to the spread of terminal W=O bonds. Therefore, a higher Raman shift

of the W=O band can indicate as well increased Brönsted acidity. From the structural perspective, it is proposed that the over-layer structure involves W^{6+} coordinated to 6 oxygen atoms building an octahedral symmetry with some incorporation of Zr^{4+} ions, which are speculated to be surface pseudo-heteropolyacids [56]. Applying X-ray absorption spectroscopy, a local structure of WO_x could be confirmed being a distorted octahedral symmetry, which underwent no significant change with increasing ρ_W [62]. The reduction behavior of WO_x species was also reported to influence the activity and acidity of the catalysts [62,63]. It is proposed that once poly-WO_x clusters are formed, they are able to delocalize negative charge, which can be later balanced by protons to generate strong acidity. Such a proton attachment and electron transfer over extended interconnected W–O–W systems are similar to the electronic structure of heteropolyacids as proposed by van Bekkum et al [64]. The addition of elements that can provide protons from H_2 splitting such as Pt has a huge impact for enhanced surface acidity of WZr catalysts as illustrated in Figure 1-2[62]. Such an approach has been intensively exploited particularly for hydro-isomerisation reaction resulting in a highly active and stable WZr catalyst. [59,62,65–70].
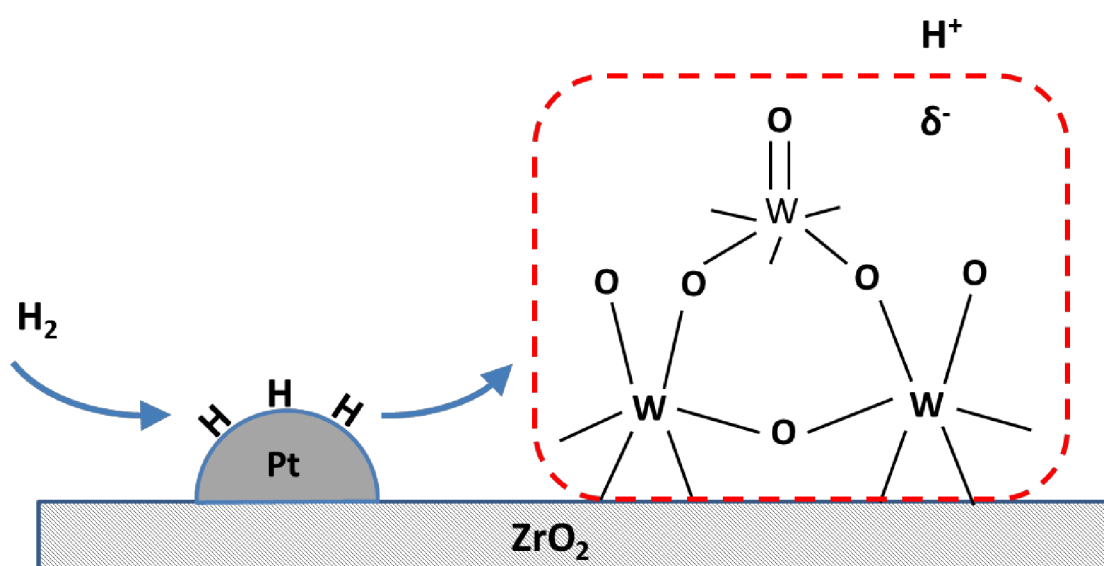
Figure 1-2 Acidity and hydrogen spill over mechanism on Pt-WOx/ZrO2 adapted from Barton et al [62]

Preparation conditions have been optimized to search for ρ_W at which monolayer poly-WO_x coatings occur. Hino and Arata as early as 1988 firstly optimized the preparation condition for WZr. They suggested that 13 wt.% WZr catalysts calcined at 800 – 850 °C were the most active for n- to iso-pentane isomerization [20]. While Scheithauer et al in 1998

reported that 19 wt.% WZr calcined at 650 °C demonstrated the highest conversion rate of n-pentane [57]. It was later on realized that the population of W atoms occupying 1 nm^2 of catalyst surface leading to a well-known dependency between ρ_W and catalytic activity. Baertsch et al reported that the optimum ρ_W for dehydration of 2-butanol was 9.6 W/nm^2. At this ρ_W, the ZrO$_2$ support was fully saturated by an amorphous poly-WO$_x$ layer [71]. Isomerization of n-hexane attained an optimal conversion rate as the monolayer shield of poly-WO$_x$ at a ρ_W of 6 W/nm^2 developed [72]. Boyse et al reported that ρ_W as high as 6 W/nm^2 was required to have a complete over-layer coverage responsible to the maximum activity of the n-butane isomerizetion. [58]. Applying one pot hydrothermal synthesis, a WZr catalyst with 6.2 W/nm^2 associated to the threshold of complete poly-WO$_x$ over layer coverage was able to optimally isomerize n-pentane [73]. Martinez et al showed that 6.8 and 5.2 W/nm^2 are required to reach the maximal hydro-isomerization of n-hexadecane for WZr catalysts prepared by co-precipitation and impregnation, respectively [63]. Shiju et al observed that a monolayer capacity of 7.3 W/nm^2 was responsible for the efficient production of ε-caprolactam from cyclohexane oxime [74]. Zhu et al also proposed that saturation of the WO$_x$ over-layer at 15 wt.% caused a superior rate in hydrogenolysis of glycerol to 1,3-propanediol over Pt-WO$_x$/SiO$_2$-ZrO$_2$ [75]. Interestingly, several investigations emphasized an optimum activity in the presence of WO$_3$-NPs, which is slightly beyond monolayer coverage. Barton et al noted that ρ_W as high as 10 W/nm^2, which was just above saturation coverage, was necessitated to reach the maximal TOF for ortho-xylene isomerization [62]. The incipient formation of crystalline WO$_3$ at ρW of 6.6 W/nm^2 apparently led to the highest rate of acetic acid esterification [76]. The highest initial rate of palmitic acid esterification was identified at 8.9 W/nm^2 at which crystalline WO$_3$-NPs were already present [77]. Moreover, WO$_3$-NPs in Pt-WZr were indispensable for high activity in the isomerization of n-pentane and n-heptane [65]. Furthermore, the group of Wachs succeeded to visualize the active W species on zirconia applying high resolution microscopy with high angle annular dark field imaging (HAADF) [78]. It was discovered that the most active WZr catalysts consisted of sub-nanometer Zr-WO$_x$ clusters composed by 8 – 15 W atoms (Figure 1-3). From the micrograph, bright features caused by sub-nanometer WO$_x$ clusters (white circles) can be identified for the most active catalyst with a W population of 6.2 W/nm^2. Therefore, it can be deduced that the appearance of W clusters emerging at

higher WO_3 loadings is responsible for high catalytic activity in methanol dehydration. In addition to acid catalyzed reactions, WZr has also been used for a number of reaction requiring bifunctional catalysts. The ability of WZr to provide Brönsted acidity has attracted lots of attention for selective hydrogenolysis reactions Ethylene glycol can be dehydrated to facilitate highly selective C-O cleavage followed by the hydrogenation of ethanol intermediate to ethane in an aqueous phase over Pd-WZr catalyst [79]. Selective production of 1,3-propanediol from glycerol was successfully performed employing Pt-WZr [80–83]. A bifunctional metal-acid Ir-WO_x/SiO_2-ZrO_2 catalyst was successfully applied for ring opening of methylcyclohexane, a model compound of naphtha [84]. For NO_x reduction under an O_2 excess, Pt-WZr enabled high activity at a low temperature [85].
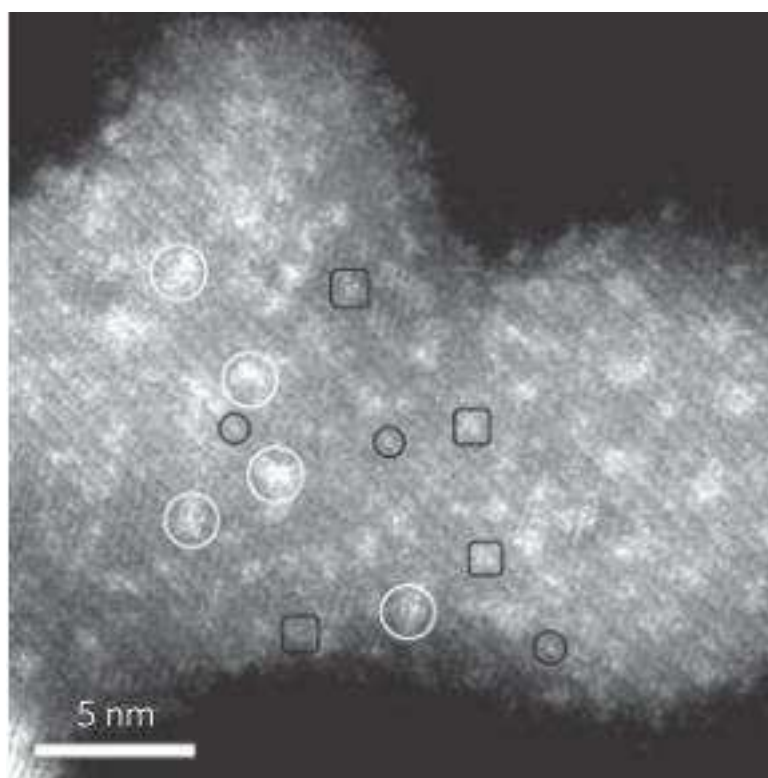
Figure 1-3 High annular dark field imaging for the most active WO_x/ZrO_2 (ρ_W = 6.2 W/nm^2) in methanol dehydration. Spots assigned with dark circle and squares represent mono- and poly-tungstic species while white circles are designated to sub-nanometer WO_x clusters [60]

1.2 Levulinic acid as a sustainable chemical derived from lignocellulose

The depletion of non-renewable resources such as petroleum has caused increasing attention concerning the utilization of sustainable feedstocks to produce chemicals and fuels. Biobased sources like fats, vegetable oils and sugars have been massively investigated

in the last two decades as they are potentially renewable, sustainable and environmentally benign. However, the exploitation of these sustainable resources to substitute petroleum seems to face a serious problem in the future due to a competition with food supply. This has shifted the sustainability orientation from edible to inedible renewable sources such as lignocellulose. Lignocellulose can be harvested from agricultural and municipal waste providing a low cost feedstock for further processing. Lignocellulose is chemically composed of cellulose, hemicellulose and lignin which are considerably inert. Crystalline cellulose and amorphous hemicellulose constitute approximately 60 – 90 wt.%, while 15 wt.% of biomass are lignin [86]. Cellulose is a polysaccharide, which can be partially hydrolyzed to cellooligomers or completely hydrolyzed to generate glucose. Whilst cellulose is only built of glucose, different sugar monomers with 5 (xylose and arabinose) and 6 carbon atoms (glucose, galactose and mannose) are the building blocks of hemicellulose. Moreover, lignin is a highly branched aromatic polymer consisting of coniferyl, sinapyl and coumaryl alcohol.

Several methods have been investigated to convert biomass to platform chemicals as starting point for further upgrading. A thermal treatment can facilitate the destruction of unreactive biomass constituents to simpler molecules possessing higher reactivity. Biomass can thermally be decomposed by gasification in gases such as H_2, CO, CO_2, CH_4 and N_2 under assistance of either steam or air. Subsequently, the product composition can be adjusted to be rich in H_2 by means of water gas-shift reaction. The outlet of the gasifier can be further tailored to produce liquid fuels via Fischer-Tropsch synthesis. Beside gaseous products, gasification also generates tar, which possesses condensed high molecular weight hydrocarbons formed in the downstream of the gasifier. Tar deposits will cause clogging in the pipes, which has to be removed to allow continuous operation. Tar removal is so far the most challenging issue faced by gasification technology since the removal is expensive [86]. A thermal treatment of biomass can also lead to the production of bio-oil through pyrolysis. In pyrolysis, the solid structure of biomass is decomposed by heat in inert atmosphere to yield bio-oil. The residence time of pyrolysis plays an important role to control the outcoming product. Slow pyrolysis generates a large amount of coke, while fast pyrolysis enables bio-oil yields up to 80 wt.% dry basis. Pyrolysis is advantageous because a large fraction of biomass can be converted to bio-oil in a single reactor. Nevertheless, the resulting bio-oils have very high acidity, poor cold flow properties and low stability so that they need

to be further upgraded to meet the desired specifications. Huber et al highlighted several possibilities to upgrade bio-oil constituents for instance by hydrodeoxygenation and steam reforming [86,87]

The previous discussion has briefly elaborated some potential processes to transform biomass to value added products using high temperature approaches. Gasification requires operation temperatures stretching from 500 – 1000 °C, while fast pyrolysis is conducted at 375 – 525 °C. Another approach to decompose the polymeric structures of biomass relates to low temperature hydrolysis. In hydrolysis, biomass is brought into contact with water with or without additional chemicals and mild heating is applied in the temperature range of 25 – 200 °C [88,89]. For the case of corn stover hydrolysis, the introduction of diluted acid facilitated a very high sugar yield of 92.5 %. Cellulose depolymerization can also be done by suitable enzymes as catalysts, which can boost the yield up to 100 %. Nevertheless the enzymes are costly and space-time yields are low limiting their utilization for a large scale operation. The resulting glucose molecules are the mother of the biorefinery because their derivatives are highly promising platform chemicals [87].

Levulinic acid has been listed as one of the most potential sugar derivatives because it has a high functionality for further transformation. Levulinic acid is a biogenic acid containing 5 carbons and is functionalized by one ketone and one carboxylic acid group. It appears to be a viscous liquid at room temperature and boils at 245 °C. This biogenic acid is a product of deep hydrolysis and dehydration of glucose or fructose in which 5-hydroxymethyl furfural (5-HMF) occurs as an intermediate. The technology for levulinic acid production has been highlighted by Rackemann and Doherty [90]. Recalling that biomass is abundant and not expensive, the production of levulinic acid from biomass feedstock will be increasingly considered. The Biofine process offers an efficient manufacture of levulinic acid by using two consecutive hydrolysis (R1) and dehydration reactors (R2) [91]. For R1, hydrolysis is performed at 220 °C at 25 bar pressure and short reaction time (12 s) to depolymerize the biomass feed into soluble products namely mono- and disaccharides as well as 5-HMF. Subsequently, the outlet from R1 is further processed in R2 where the production of LA takes place. R2 is operated at milder conditions (190 °C and 14 bar) and exhibits a larger dimension than R1 since its longer residence time of up to 12 min is needed for the formation of levulinic acid. Biofine has claimed to be able to reach a very high LA yield of 75

% from hexoses. Levulinic acid has been produced in a commercial scale by GF Biochemical company announcing a production capacity 2000 ton/year [92,93]. It presents a suitable platform chemical for further conversion to e.g. fuels, plasticizers, chemical intermediates, herbicides, foods, resins and flavoring agents.

Levulinic acid esters (LAE) or alkyl-levulinates, synthesized via esterification of levulinic acid, are highly prospective owing to their broad applications [94]. Because of their lower vapor pressures, LAE can be used to replace harmful trichloroethylene as degreasing agent in metal industries as reported by Ferrer et al [95]. The authors also revealed that low cytotoxicity, mutagenicity of butyl and pentyl-levulinate enable these esters to be deployed as green solvents. Introducing LAE into a fuel mixture will lead to cleaner combustion emitting lower levels of NO_x and soot, respectively [96]. LAE show potential as substitutes for conventional fuel additives such as methyl tert-butyl ether and ethanol [97]. The miscibility of different LAE has been studied to comprehend their behavior in a mixture of diesel fuel [98]. Ethyl levulinate (EL) underwent phase separation from a diesel blend at 10 °C whereas butyl levulinate (BL) remained completely miscible up to -10 °C. Based on those results, BL is more appropriate for addition in diesel fuels. Furthermore, levulinic acid ester ketals (LAEK) with a molecular weight above 300 possess high stability to be applied in plasticizers [99]. LAEK have also been identified to be very promising in perfume formulation and personal care manufacture [100,101]

Because of their importance and broad applications, the production of LAE has found considerable attention. A comprehensive review regarding the production methods of LAE has been reported by Demolis et al [94]. Fernandes et al compared different types of zeolites and sulfated metal oxides for the synthesis of EL [102]. USY zeolite possessing one third lower of acid sites number than H-ZSM 5 unexpectedly performed the best among other zeolites. In this case 2.5 wt.% USY could convert nearly 8% of LA, whereas H-ZSM 5 was only able to achieve 4% conversion after 4 h. The higher catalytic activity of USY zeolite was suggested to be caused by its larger pore openings allowing the substrate to readily reach the active sites. The three dimensional pore channels of USY zeolites can also give a positive impact on the molecular traffic permitting the products to readily diffuse out of the catalyst. Concerning supported sulfate species, TiO_2 and SnO_2 supports were able to reach the highest EL yields. The activity can ascribe to the ability of TiO_2 and SnO_2 to retain more SO_4^{2-} anions

after impregnation. Comparing those two types of catalysts, SO_4^{2-}/metal oxides particularly SnO_2 and TiO_2 were superior being able to achieve 36 – 38% of LA conversion after 4 h compared to 8% for USY. An enrichment of the SO_4^{2-} population on SnO_2 was attempted by multiple impregnations. The method enabled a linear increase of the SO_4^{2-} density as well as the number of acid sites. Nevertheless, after the 4th impregnation, a decline in BL yield was observed implying that the activity did not thoroughly relate to the concentration of acid sites. The concentration of strong acid sites was suggested to play a vital role in this reaction. The production of EL over SO_4^{2-}/ZrO_2 can be significantly increased by incorporating Si during the support preparation [103]. The presence of SiO_2 substantially increases the specific surface area, which in turn can be used to anchor SO_4^{2-} ions. In addition, incorporated Si could generate a mesoporous structure, which was beneficial to prevent diffusional barriers. 7.5 – 10 mole.% Si were observed to give the highest LA conversion of up to 39%. Despite their superior activity, it is important to note that sulfated metal oxides suffer substantial deactivation due to SO_4^{2-} ion detachment. The synthesis of BL over different types of zeolites was reported by Maheria et al [104]. Despite a higher NH_3-uptake of HZSM-5, the yield of BL was very poor. Interestingly, the conversion of BL reached 32% for USY zeolite (10 wt.% respective to LA) with a relatively low acid site density. In another effort to utilize the highly acidic HZSM-5, soaking the microstructured HZM-5 catalyst in NaOH solution was reported. Partially leached SiO_2 could enlarge the pore width leading to mesostructured HZSM-5 (meso HZSM-5). Meso HZSM-5 apparently demonstrated considerable activity in the synthesis of bulkier octyl levulinate, which is prospective as biolubricant [105]. Supported heteropoly acids (HPA) have also been tested for LA esterification facilitating superior catalytic activity. Mesoporous silicas, treated clays and desilicated zeolites were chosen to host HPA since the high specific surface area and bigger pore size of these supports are suitable to immobilize bulky HPA [106–109]. Leaching of HPA can still be noticed after several runs resulting in moderate deactivation. A new catalyst type for such transformations are metal organic frameworks (MOF). They were recently reported to be catalyzing LA esterification with butanol [110]. In this case, MOFs based on Zr-modified terephthalate ligands were able to achieve 99 % *n*-BL yield after 4 – 5 h reaction time. To conclude, it is evident that the textural properties are highly significant to promote LA esterification. In addition, the concentration

of active sites does not always influence activity. Strong acid sites have been suggested to be the determining factor for the reaction.

This page is intensionally left blank

Chapter. 2 One Pot synthesis of WO$_x$/ZrO$_2$ catalysts for the production of levulinic acid esters

2.1 State of the art

As a versatile compound, levulinic acid can be transformed to numerous high added value products. Rackemann and Doherty [90] together with Pileidis and Titrici [111] have summarized the potential chemicals derived from biogenic levulinic acid as illustrated Figure 2-1. Levulinic acid esters (LAEs) become one of the most promising compounds because of their vast applications stretching from fragrances, bio-lubricants, fuel additives, and green solvents. A review concerning their applications and synthetic routes has been reported by Demolis et al [94]. LAEs have been prepared over many different types of solid acids. Zeolites with mesoporous structure can substantially alleviate internal mass transport inside pores [102,104,105,112]. Sulfonated mesoporous SiO$_2$ [113], mesoporous ZrO$_2$ [103] and nanotubes [114] have shown their high activity in the production of esters of LA. Superior activity is encountered for supported heteropoly acids in LA esterification [106,115,116]. LAEs have also been produced over Zr-MOF prepared from terephthalate ligands [110]. Recently, a continuous LA esterification in vapor phase has been carried out on ZrO$_2$/SBA-15 as a catalyst [117]. Over different types of solid acids, potentially stable WO$_x$/ZrO$_2$ (WZr) has not been studied yet for levulinic acid ester synthesis. In fact, number esterification reactions can successfully be catalyzed by WZr. WZr successfully enabled the esterification of acetic acid in liquid and vapor phase [76,118,119]. WZr demonstrated high activity in the synthesis of long chained fatty acid esters [77,120,121]. WZr was also reported to be active in the synthesis of aspirin (acetyl-salicylic acid) [122]. Due to its limited specific surface area, WO$_x$/ZrO$_2$ can be dispersed over a large specific surface area MCM-41 support, which facilitates the esterification of oleic acid with methanol [123]. Based on these reports, a systematic study on the preparation of mesoporous WO$_x$/ZrO$_2$ (WmZr) as catalyst for LA esterification has been carried out. The mesoporous feature of catalyst is expected to

alleviate the diffusion of substrates and products inside catalyst pores. A facile one-pot evaporation induced self-assembly will be employed to direct the formation of meso-structure. This route has been successfully applied in the preparation of mesoporous metal oxides such as Al_2O_3 [124], Nb_2O_5 [125], TiO_2 [126], Zr-phosphate [127], Y-ZrO_2[128] and NiO-MgO-Al_2O_3 [129].
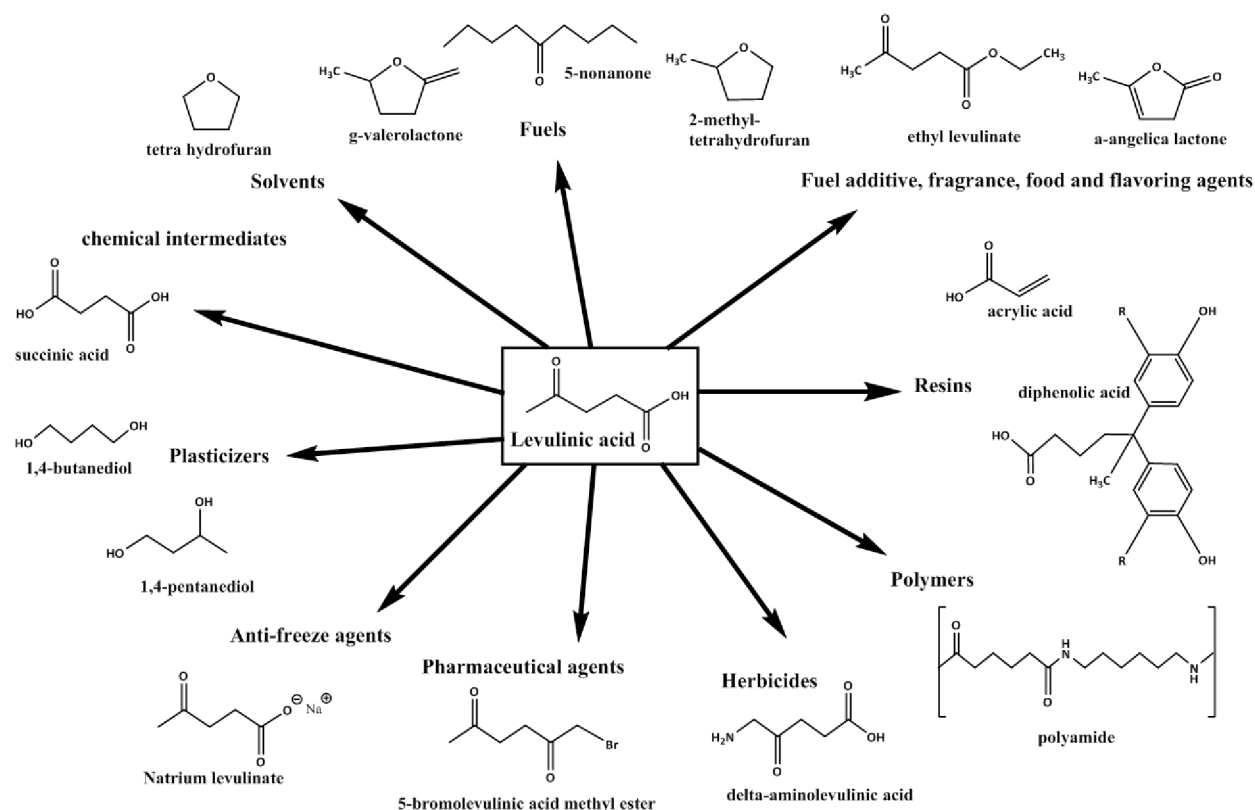
Figure 2-1. Various chemicals derived from levulinic acid, adapted from Rackemann et al [90]

2.2 Result and discussion

2.2.1 Catalyst selection

Before a comprehensive material characterization, a selection of promising WmZr catalysts appears necessary. The selection is based on their activity in catalyzing LA esterification as demonstrated in Figure 2-2. Esterification of LA and 1-butanol (1-BuOH) was carried out for 2 h at 120 °C with 1-BuOH/LA ratio of 2. Two isomers of butyl levulinate were detected namely pseudo (*p*-) and normal butyl levulinate (*n*-BL). The entire catalyst series display a similar trend. Regardless of calcination temperature, a higher WO_3 content leads to higher formation of ester products. In general, catalysts calcined at 800 °C exhibit higher

activities and present a maximum of *n*-BL yield at 20 wt.% WO_3 concentration. Based on this result, the influence of WO_3 loadings on the catalyst properties will be evaluated at 800 °C. Meanwhile, the effect of calcination treatment will be assessed at a fixed WO_3 loading of 20 wt.%.
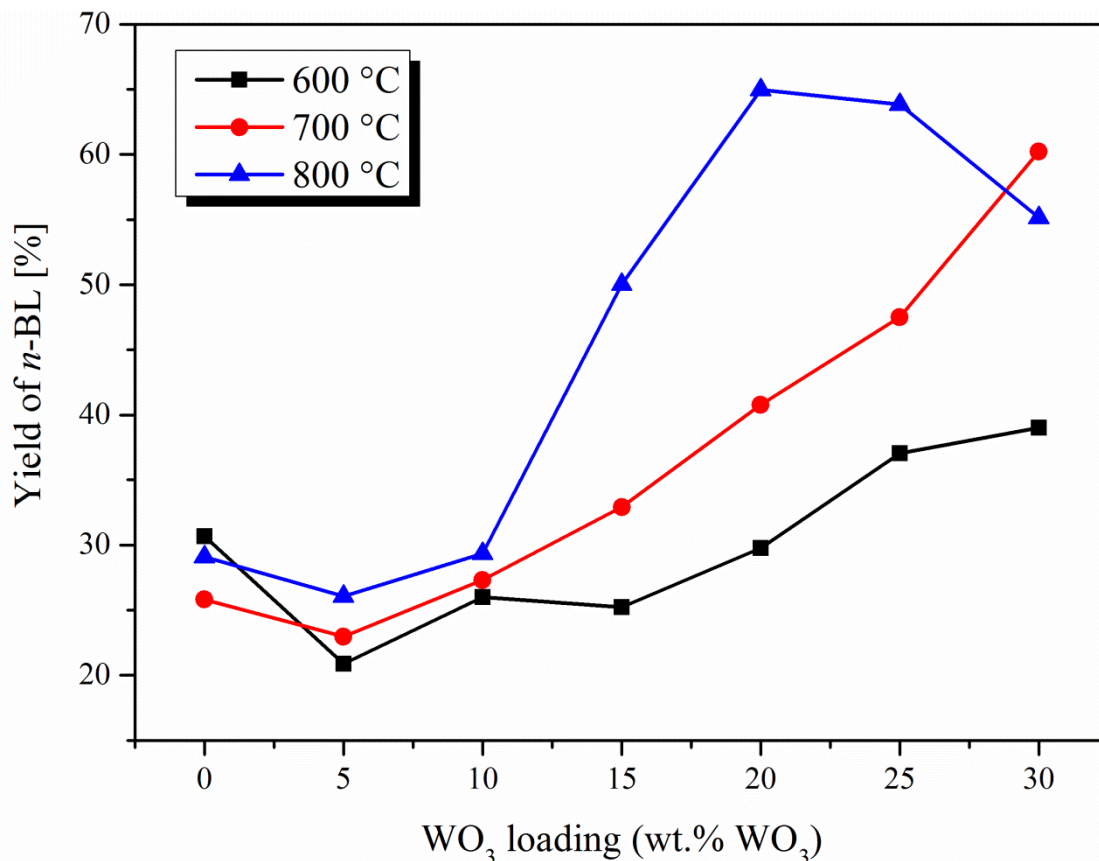
Figure 2-2. Catalytic activity of WmZr catalysts with different WO_3 content and calcination temperatures. Reaction was performed after dosing the mixture of LA and butanol (1-BuOH/LA = 2) with 10 wt.% catalyst (according to the mass of LA) for 2 h at 120 °C.

2.2.2 Isothermal N_2-physisorption for catalyst characterization

Isothermal N_2 physisorption was employed to characterize the physicochemical properties of the prepared catalysts calcined at 800 °C with variation of WO_3 concentrations as summarized in Table 2-1 and Figure 2-3a and b. All catalysts demonstrate a hysteresis at relative pressure above 0.4 indicating the presence of mesopores. Catalysts with 0 – 15 wt.% WO_3 demonstrate appreciable improvement of the initial N_2 uptake and possess shifts of the hystereses to lower partial pressures. This finding implies that at this loading range, the addition of WO_3 leads to higher specific surface areas accompanied by smaller pore sizes. For catalysts loaded with 20 – 30 wt.%, the change in the initial N_2 uptake and the shift of hystereses are not so discernable implying insignificant difference in obtained pore size and

specific surface area. Furthermore, evaluating the pore size distribution (PSD) of pure ZrO_2 (0 wt.% WO_3) emphasizes a broad distribution ranging from 6.5 to 16 nm and a very low overall pore volume of 0.05 cm^3/g as presented in Table 2-1 and Figure 2-4a, respectively. Introducing WO_3 loading of 5 to 15 wt.% causes a considerably narrower PSD together with a smaller pore size. For even higher WO_3 loadings of 20 to 30 wt.%, PSD broadens again. Moreover, the resulting specific surface areas (Table 2-1) increase from 15 to 54 m^2/g for 0 – 15 wt.% WO_3 incorporated during synthesis. Further WO_3 enrichment from 20 to 30 wt.% results in specific surface areas around 54 to 58 m^2/g. The enhanced specific surface areas and more uniform pore size distributions can be attributed to the formation of rather stable W-O-Zr bonds on the surface. The creation of those bonds is able to reduce the mobility of Zr atoms on the surface minimizing sintering [62].

Moreover, the dependency of N_2 isotherms on calcination temperatures is shown in Table 2-1 and Figure 2-3c. WmZr calcined at 600 and 700 °C reflect comparable initial N_2 uptakes as well as the formation of a hysteresis. After calcination at 800 and 900 °C, N_2 uptakes drastically drop followed by a shift of the hysteresis to higher partial pressures. It reflects that the specific surface areas shrink and pore size enlarges after calcination at elevated temperature. Furthermore, the influence of calcination temperatures on PSD is presented in Figure 2-4b. A narrow pore size distribution located at 4.6 nm can be obtained by calcining the catalysts at both 600 and 700 °C. The PSD is further stretched with a maximum at 6 nm after subjecting the material to 800 °C before it substantially broadens as a result of exposure to 900 °C. The consequence of varying calcination temperatures on the resulting specific surface areas is summarized in Table 2-1. Rising calcination temperatures from 600 to 700 °C insignificantly affect the obtained specific surface areas yielding only a slight decline from 111 to 90 m^2/g. Applying higher calcination temperatures of 800 and 900 °C leads to a substantial decrease in specific surface are of 54 and 25 m^2/g, respectively. These results emphasize that high calcination temperature can trigger pore collapse since higher energy is available to mobilize surface Zr atoms facilitating sintering. The increasing pore size due to higher calcination temperatures were also observed in other reports [58,130]. It has been proposed that the harsh calcination temperatures particularly for transition metal oxide are able to damage mesostructure by forming bigger particles leading to the bigger pore width.

The calculated theoretical W surface density (ρ_W) expressing the number of W atom per nm^2 is summarized in Table 2-1. For materials with different W loadings, ρ_W gradually increases from 3.2 (5 wt.% WO_3) to 11.7 W/nm^2 (30 wt.% WO_3). While for the samples calcined at different temperatures, ρ_W increases gradually from 3.7 to 4.6 W/nm^2 after being exposed to 600 and 700 °C, respectively. Subseqeuntly, an sudden increase of ρ_W occurs for samples calcined at 800 (11.7 W/nm^2) as well as 900 °C (16.4 W/nm^2). Such a dramatic increase can be caused by a significant decline in the resulting specific surface area after the samples were treated at 800 and 900 °C. In comparison to literatures, EISA provides a superior W dispersion compared to materials prepared via impregnation. 15 wt.% WZr calcined at 800 °C via incipient wetness impregnation reached ρ_W of 8 W/nm^2 [77]. A similar finding was also obtained for WZr (15 wt.% calcined at 800 °C) prepared by wet impregnation possessing 8.4 W/nm^2 [60]. A slightly higher ρ_W of 10.5 W/nm^2 was obtained for 15 wt.% WZr after being calcined at 800 °C [71]. Shiju et al reported that ρ_W as high as 7.6 W/nm^2 resulted for 10 wt.% WZr (calcination at 800 °C) synthesized by wet impregnation [74]. In the present study, 15 wt.% WmZr thermally treated at 800 °C possesses a ρ_W of 6.2 W/nm^2 implying better W dispersion. The one pot synthesis of WZr e.g. via co-precipitation and sol-gel tends to produce low ρ_W. One-step synthesis via co-precipitation to prepare 15 wt.% WZr (calcined at 800 °C) was applied by Martinez giving ρ_W of 5.5 W/nm^2 [63].

Table 2-1. Physicochemical properties of WmZr catalysts

WO$_3$ Loading [%]	Calcination temperature [^{o}C]	S$_{BET}$ [m^2/g]	D$_{pore}$ [nm]	V$_{pore}$ [cm^3/g]	ρ_W [W/nm^2]
0	800	15	13.0	0.05	0.0
5	800	33	8.1	0.06	3.2
10	800	48	6.5	0.08	5.6
15	800	54	5.5	0.08	6.2
20	800	58	6.0	0.09	7.7
25	800	54	6.0	0.07	9.5
30	800	54	7.1	0.09	11.7
20	600	111	4.6	0.09	3.7
20	700	90	4.6	0.09	4.6
20	900	25	6.7	0.05	16.4
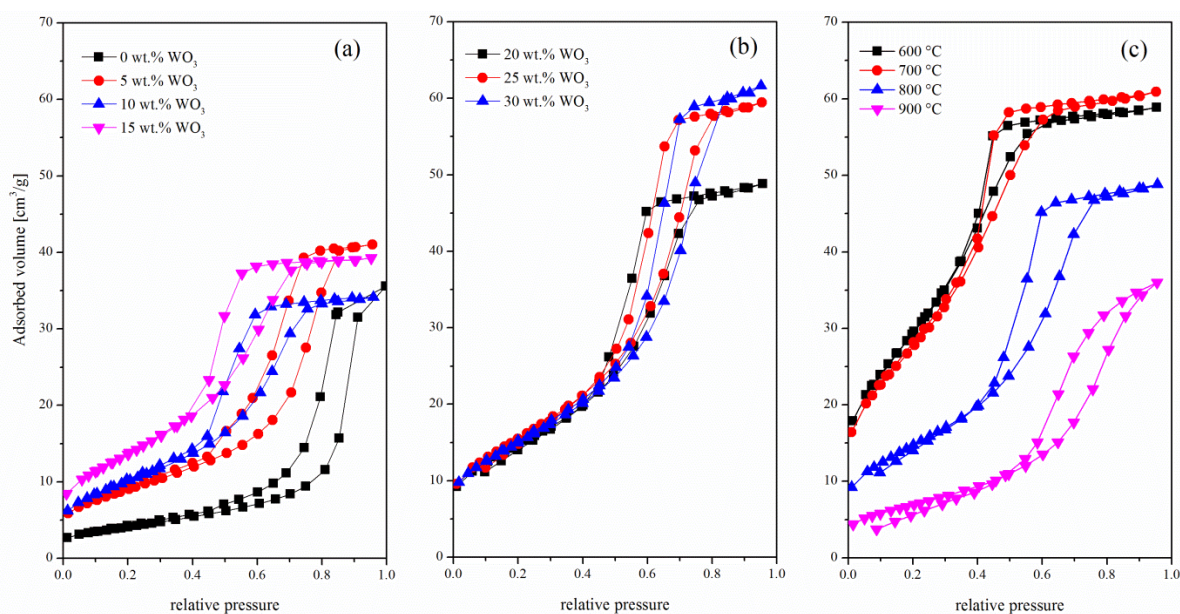
Figure 2-3. Isothermal N$_2$ physisorption of WmZr catalysts loaded with 0 – 15 wt.% WO$_3$ (a), 20 – 30 wt.% WO$_3$ and 20 wt.% WO$_3$ loading calcined at various temperatures (c).
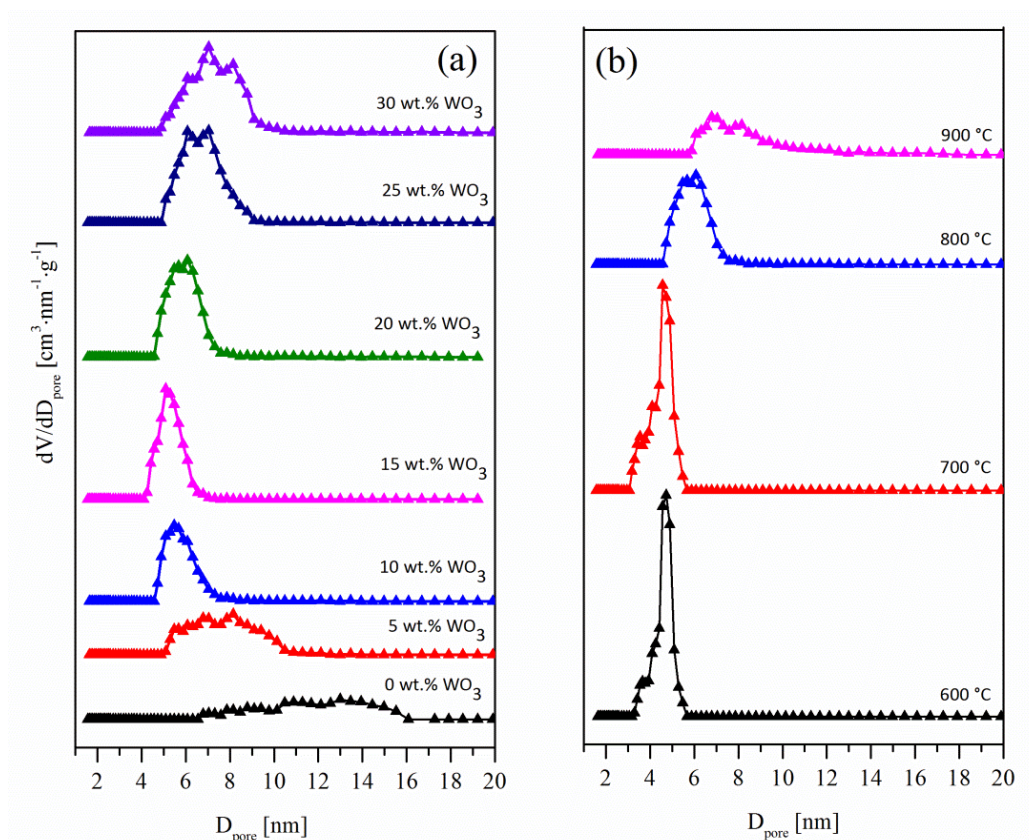
Figure 2-4. Pore size distribution of the catalysts with different WO₃ loadings (a) and 20 wt.% WO₃ loading calcined at different temperatures (b)

2.2.3 Catalyst characterization by X-ray diffraction

XRD was employed to investigate the resulting bulk structure of the catalysts. Figure 2-5a demonstrates the reflection pattern of catalysts containing different WO_3 amounts. The reflections at 28.2, 31.5 and 34.5° can be assigned to monoclinic ZrO_2, whereas the presence of tetragonal ZrO_2 can be recognized by the incidence of reflections located at 29.0, 35.3, 50.1, 60.2, and 62.9°. The coexistence of the tetragonal and monoclinic phase of ZrO_2 can be observed as WO_3 is absence (0 wt.% WO_3). Upon addition of small amounts of WO_3 (5 wt.%), monoclinic ZrO_2 vanishes leaving only the tetragonal phase. The addition of higher WO_3 concentrations leads to no significant difference in terms of ZrO_2 diffraction patterns. In addition, no reflection coming from WO_3 can be detected for 5 to 20 wt.% WO_3. Small reflections around 23 – 24° can be spotted for the catalyst possessing 25 wt.% WO_3 suggesting the emergence of WO_3-NPs. The reflex intensity rises for 30 wt.% WO_3 incorporated during synthesis. The presence of WO_3-NPs is also corroborated by visual inspection of the materials showing a yellowish color for samples with a WO_3 content higher

than 20 wt.%. The influence of W addition on the crystallinity of ZrO_2 has been studied by Barton et al [59]. They observe that after introducing 4 wt.% WO_3, the crystal size of ZrO_2 decreased from 35 to 18 nm. The reduction of crystal size was apparently accompanied by disappearance of monoclinic ZrO_2. Strong interactions between W and Zr facilitate surface passivation through the immobilization of surface Zr atoms potentially suppressing sintering during thermal treatment at high temperatures.

The structural characteristics of WmZr catalysts can also be affected by the calcination temperatures. To study this effect, catalysts with a fixed W loading of 20 wt.% are selected and exposed to different calcination temperatures (Figure 2-5b). Varying calcination temperatures from 600 to 700 °C does not cause significant difference in the XRD profiles of the materials. Within this range, all arising reflections correspond to the formation of tetragonal ZrO_2. Noteworthy, monoclinic ZrO_2 can actually be detected as pure mesoporous ZrO_2 was calcined at 600 °C. This finding reveals that the presence of WO_3 is vital to preserve unstable tetragonal ZrO_2 at high calcination temperatures. Nonetheless, monoclinic ZrO_2 evolves together with the growth of WO_3-NPs as the catalyst is calcined as high as 900 °C. Apparently, the transformation of the tetragonal to the monoclinic phase was promoted at 900 °C. Calcination temperatures as high as 900 °C are considered to provide adequate energy to mobilize surface Zr atoms resulting in massive sintering and collapse of mesostructures. Visual inspection also emphasizes the presence of WO_3-NPs causing a yellowish color of the catalyst thermally treated at 900 °C. Thus based on the results, it can be suggested that 900 °C is the threshold for the transformation from tetragonal to monoclinic ZrO_2 as well as the evolution of WO_3-NPs.
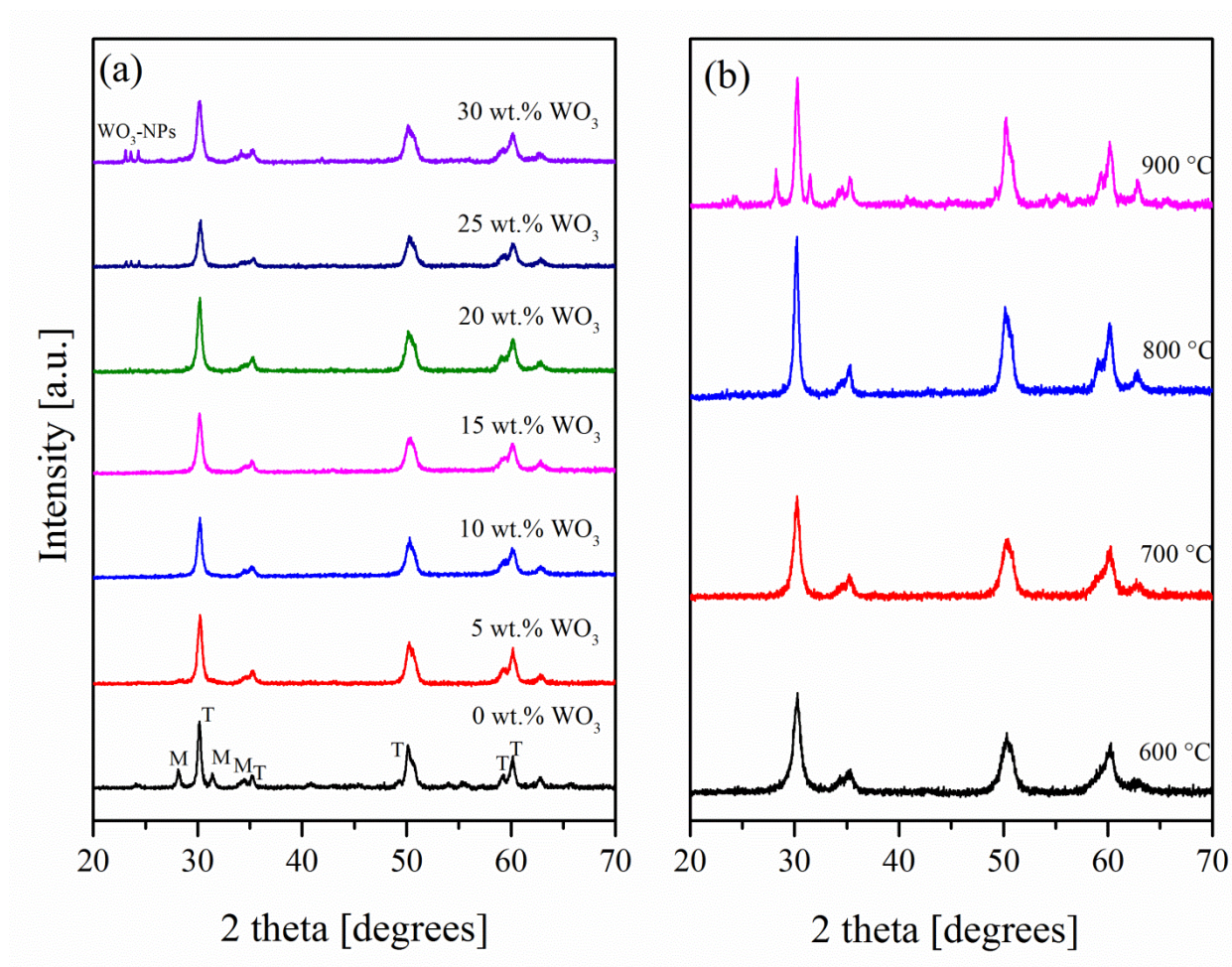
Figure 2-5. (a) X-ray reflection of catalysts with different WO$_3$ loadings (calcined at 800 °C) and (b) 20 wt.% WO$_3$ loading treated at different calcination temperatures (20 wt.% WO$_3$)

2.2.4 Catalyst characterization by Laser FT Raman spectroscopy

Surface features of the prepared catalysts are studied using Raman spectroscopy. Figure 2-6a illustrates Raman spectra of catalysts synthesized with different WO$_3$ loadings. Raman shifts lower than 700 cm^{-1} can be used to interpret surface states of ZrO$_2$ species, while the spectra evolving at higher than 700 cm^{-1} are the footprint of WO$_x$ species. Raman bands at 220, 278, 333, 345, 380, 477, 502, 538, 559, and 617 cm^{-1} can be assigned at monoclinic ZrO$_2$, while tetragonal ZrO$_2$ can be identified through emerging bands at 266, 315, 461 and 648 cm^{-1}, respectively. For unloaded mesoporous ZrO$_2$, the tetragonal and monoclinic ZrO$_2$ phase coexist. Furthermore, only the tetragonal phase is detected after introducing 5 wt.% WO$_3$ implying that the monoclinic phase is considerably suppressed upon WO$_3$ addition. The Raman features for ZrO$_2$ do not alter significantly with increased amount of WO$_3$. Concerning WO$_x$ surface species, the incorporation of 5 wt.% WO$_3$ results in the evolution of two broad

bands located at 826 and 974 cm^{-1}. The first corresponds to the W–O and W–O–W stretching mode whereas the latter is responsible to the stretching terminal of W=O oxo-bonds [56,57,73]. The band at 826 cm^{-1} becomes more pronounced followed by a shift of the band at 924 cm^{-1} to higher frequencies at 986 and 997 cm^{-1} as a result of increasing WO$_3$ loadings to 10 and 15 wt.%. An increased intensity of the band at 826 cm^{-1} is also associated by an increasing number and crystallization degree of sub-nanometer Zr-WO$_x$ species [60,78,131]. Additionally, a Raman shift to higher frequency in the region of 970 – 1020 cm^{-1} implies the extension of polymeric WO$_x$ domains [56,73]. Furthering WO$_3$ addition to 20 wt.% results in the emergence of distinct bands at 714 as well as 808 cm^{-1} designated to the occurrence of crystallite WO$_3$-NPs. It is important to note that WO$_3$ concentrations higher than 15 wt.% causes no further difference on the band located at 997 cm^{-1} affirming that similar polytungstic species exist for catalysts with 15 – 30 wt.% WO$_3$ loadings. Therefore, 20 wt.% WO$_3$ loading corresponding to 7.7 W/nm^2 can be suggested as the threshold concentration for the formation of WO$_3$-NPs. On the other hand, using the monolayer concept, 15 wt.% WO$_3$ (associated to 6.2 W/nm^2) can be considered as the saturation point of poly-tungstic coverage. This result is in a good agreement with previously reported WmZr prepared via EISA demonstrating that WO$_3$-NPs developed firstly at 7.8 W/nm^2 [131]. Shiju et al described that WO$_3$-NPs developed at a ρ_W of 7.3 W/nm^2.[74]. Applying a one-pot synthesis via a hydrothermal route, Song et al observed WO$_3$-NPs formation at 6.6 W/nm^2 [73].

Raman spectra of catalysts calcined at different temperatures at a constant WO$_3$ loading of 20 wt.% are presented in Figure 2-6b. The catalysts calcined at 600 and 700 °C display broad spectra from 200 – 700 cm^{-1} pointing to amorphous characteristics of the ZrO$_2$ surface. These results are in contrast to what has been shown by XRD suggesting the complete formation of crystallite ZrO$_2$. Here, the conservation of amorphous ZrO$_2$ on the surface can be associated to the presence of WO$_x$, which appears to be able to delay surface crystallization of ZrO$_2$. Livage et al proposed that amorphous surface layers of ZrO$_2$ possess a preferential local structure resembling the tetragonal phase [21,22]. Therefore, the formation of bands at 278, 315, 461 and 648 cm^{-1} can be considered as the seed for the development of tetragonal ZrO$_2$. Increasing the calcination temperature to 800 °C triggers surface crystallization and the spectra corresponding to tetragonal phase become more

distinct. Subsequently, bands associated to monoclinic ZrO_2 are recognizable for the catalyst calcined at 900 °C. Regarding the surface states of WO_x, broad bands at 849 (lower) and 974 cm^{-1} (higher) can be assigned to W–O–W and W=O stretching bonds, respectively. The lower band progressively moves to 826 cm^{-1} implying increasing crystallization of Zr-WO_x clusters, whereas the higher band shifts to 983 cm^{-1} suggest expansion of poly-WO_x domains. For the catalysts calcined at 800 and 900 °C, the band located at 826 cm^{-1} is obscured by a sharp and intense band at 804 cm^{-1} associated to the formation of crystallite WO_3-NPs. Meanwhile, increasing the calcination temperature from 800 to 900 °C does not significantly alter the position of the higher band (at 997 cm^{-1}).
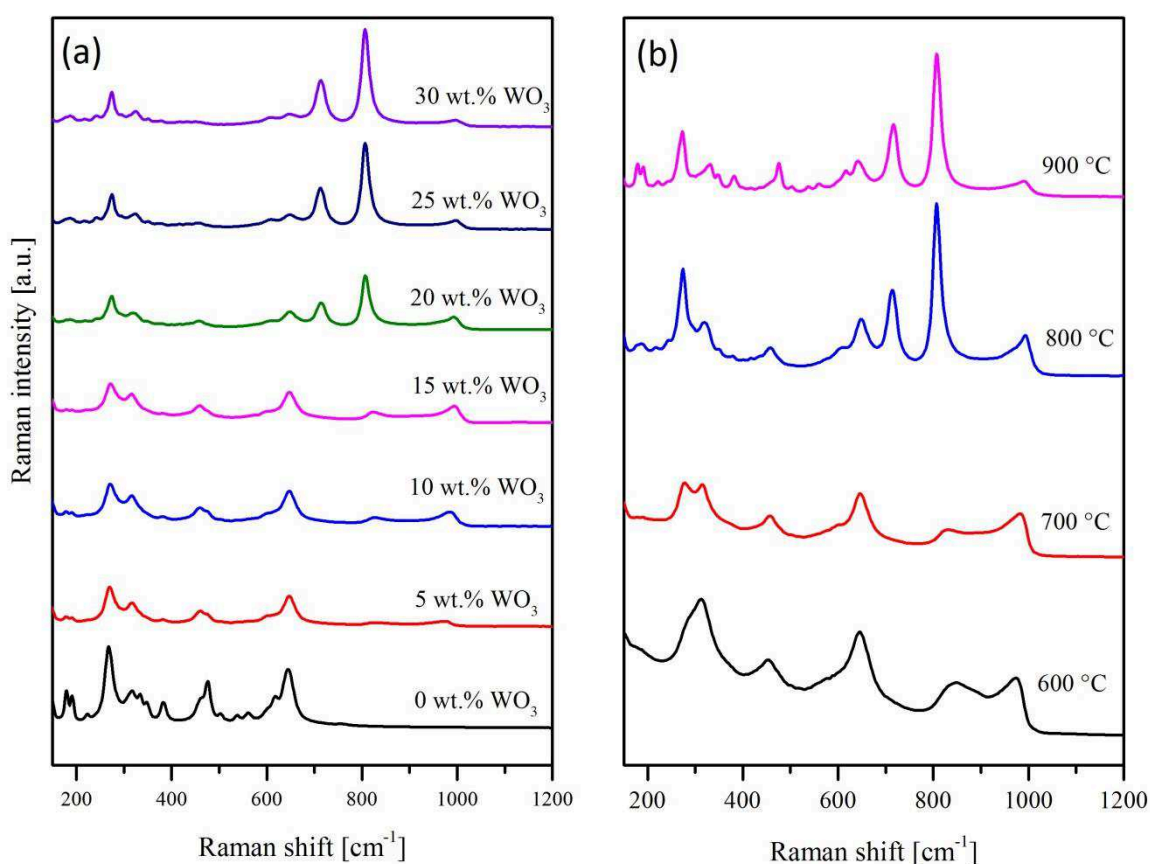
Figure 2-6. FT Raman spectra of catalysts loaded with various WO₃ loadings (a) and 20 wt.% WO₃ loading calcined at different temperatures

2.2.5   Characterization of acidity by NH₃-temperature programmed desorption (TPD)

The surface acidity of the prepared catalysts is studied via NH$_3$-TPD. Figure 2-7a illustrates the surface acidity of catalysts consisting of various WO_3 concentrations. NH$_3$ is generally desorbed at a broad range of temperatures indicating that different strengths of acid centers are present on the surface. Weak acid sites are designated for NH$_3$ desorption at

lower than 350 °C whereas the acid centers releasing NH_3 at higher than 350 °C are categorized as strong acid sites. Such an assignment has also been used by other researchers. Triantafillidis et al classified acid centers desorbing NH_3 at temperatures higher than 350 °C as strong acid sites [132]. Michalow-Mauke assigned four regions of desorption temperatures to distinguish the acid strength namely: physisorbed NH_3 (50 – 125 °C), weak acid sites (125 – 200 °C), intermediate strength (200 – 350 °C) and strong acid sites (higher than 350 °C) [133]. For catalysts with various WO_3 contents, low WO_3 loadings (0 – 10 wt.%) exhibit only low intensity of desorbed NH_3. The intensity is somewhat improved following an increase of WO_3 concentration to 15 wt.%. Furthermore, a notable enhancement of NH_3 uptakes is observed after enriching the WO_3 loading from 20 to 30 wt.%.

Moreover, a quantification of acid site density based on NH_3 desorption is provided in Figure 2-8a. In general, the liberated NH_3 gradually increases from 0.014 to 0.038 mmol/g together with the increase of WO_3 content from 0 to 15 wt.%. Afterwards, following the enrichment of WO_3 loading to 20 and 25 wt.%, a distinct improvements of the amount of released ammonia up to 0.104 and 0.107 mmol/g occurs, respectively. The number of liberated NH_3 is slightly reduced to 0.097 mmol/g as a consequence of 30 wt.% WO_3 loading. Thus, it can be concluded that at the lower loading range (0 – 15 wt.%), the acid sites increase progressively associated with the gradual polymerization of mononuclear tungstic species. The substantial enhancement of acid sites at loadings higher than 20 wt.% facilitates the development of sub-nanometer Zr-WO_x clusters, which has been confirmed to exhibit strong acidity and exceptional catalytic activity [60,78,131].

The effect of calcination temperatures on NH_3 desorption profiles is demonstrated in Figure 2-8b. NH_3 is also desorbed within a broad desorption temperature range implying the existence of acid centers with different strength. The catalyst thermally treated at 600 °C contains 0.176 mmol/g acid sites. The number of acid sites is progressively reduced to 0.143 and 0.104 mmol/g along with increasing calcination temperatures to 700 and 800 °C, respectively. A higher calcination temperature of 900 °C results in a substantial depletion of acid sites to 0.003 mmol/g. The decline of acid sites with increasing calcination temperatures can be associated to the shrinkage of the specific surface area and the collapse of the pore structures.

Figure 2-7. NH$_3$ desorption profiles for the catalysts with different WO$_3$ contents (a) and 20 wt.% WO$_3$ loading treated at different calcination temperatures (b)
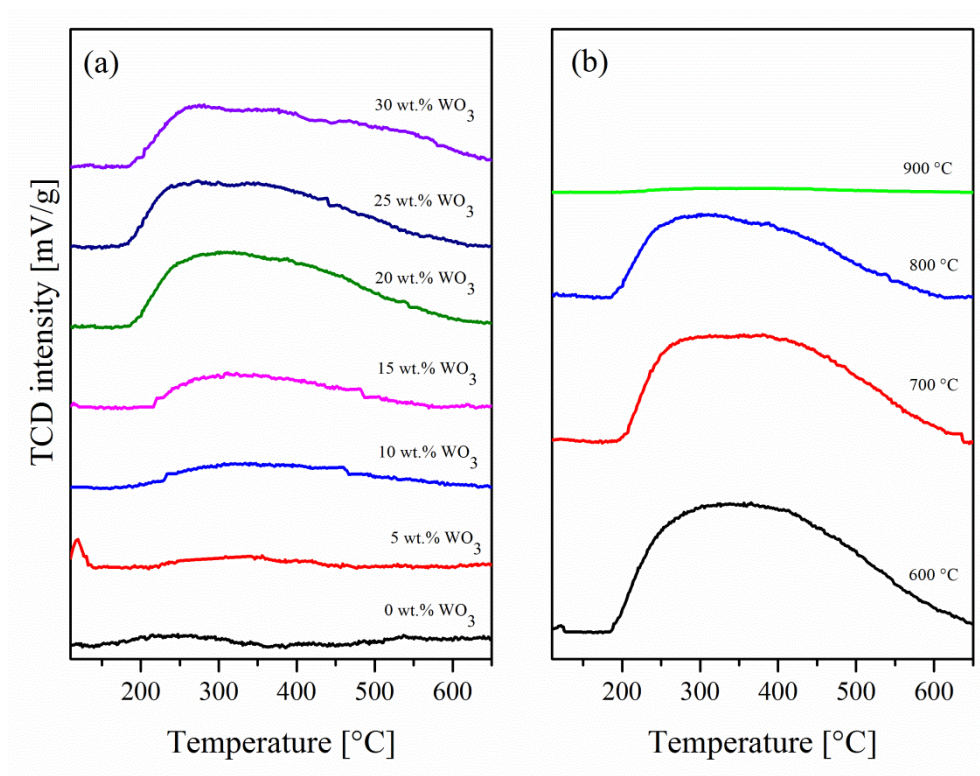

Figure 2-8. Acid sites quantification for the catalysts with various WO$_3$ loadings (a) and 20 wt.% WO$_3$ loading treated at different calcination temperatures (b)

2.2.6 DRIFT with pyridine adsorption

The discrimination of acid species was carried out by DRIFT spectroscopy with pyridine adsorption. A perturbation generated by the interaction between basic pyridine molecules and unsaturated Zr^{4+} on the surface results in the arise of a band at 1440 cm^{-1} which is associated to Lewis acid sites. Pyridine molecules are also able to bind to the protons of surface OH$^-$ functional group causing the development of a signal at 1540 cm^{-1}. This signal is characteristic of Brönsted acidity on the solid surface. Meanwhile, an emerging band at 1490 can be attributed to both Brönsted and Lewis acidity. The DRIFT spectra of adsorbed pyridine for catalysts decorated with different WO_3 loadings are presented in Figure 2-9a. Bare ZrO_2 usually possesses Lewis acidity and an appreciably lower extent of Brönsted acidity [30,56]. No significant difference in the pyridine spectra for ZrO_2 loaded with WO_3 contents between 0 and 10 wt.% (5.6 W/nm^2) occured. Those spectra exhibit only the development of Lewis acid sites at 1440 cm^{-1} suggesting isolated monotungstates mainly present on the surface leaving many uncovered unsaturated Zr^{4+} sites. Introducing 15 wt.% WO_3 (6.2 W/nm^2), a band at 1540 cm^{-1} appears associated to increasing Brönsted acidity. The formation of this band is most probably related to the condensation of monotungstic to polytungstic species. A W atom in an extended poly-WOx over-layer is able to delocalize electrons to its neighbours creating W atoms with imbalanced charge. These W atoms can finally be the hosts for protons, which are responsible for Brönsted acidity. The intensity of Brönsted acidity is considerably intensified for catalysts loaded with 20 (7.7 W/nm^2) to 30 wt.% (11.7 W/nm^2) of WO_3, which can be linked to the massive formation of Zr-WOx sub-nanometer clusters.

Furthermore, the ratio of Brönsted and Lewis acid sites (A_B/A_L) is also quantified as shown in Figure 2-10b. A_B/A_L is relatively constant at around 0 with the addition of WO_3 from 0 to 10 wt.% (5.6 W/nm^2). An appreciable increase of Brönsted acid sites takes place upon the incorporation of WO_3 to 15 wt.% (A_B/A_L = 1.2). A_B/A_L is dramatically increased up to 3.5 and 3.8 as WO_3 loading increases to 20 (7.7 W/nm^2) and 25 wt.% (9.5 W/nm^2), respectively; before it slightly declines to around 3.5 after adding 30 wt.% WO_3. It should be noted that despite the development of Brönsted acid sites, the band at 1440 cm^{-1} for Lewis acidity is still present for the entire range of WO_3 loadings. The detection of Lewis acidity even for catalysts containing the highest amount of Brönsted acidity emphasizes that not the whole

ZrO_2 surface is covered by a WO_x layer. The increase of Brönsted acidity within the loading range of 15 – 25 wt.% is in line with the propagation of polytungstic species and the development of $Zr-WO_x$ clusters, which contribute to the strong acid centers. Referring to the Raman spectra (Figure 2-6a), the development of Brönsted acidity (15 – 30 wt.% WO_3) corresponds to the formation of a W=O stretching band at 997 cm^{-1}. This band is located at lower frequencies for catalysts exhibiting a lower WO_3 loading. It is suggested that the swing of the band in the higher frequency region of 960 to 996 cm^{-1} can be used to indicate the development of Brönsted acidity [57,63]. It is also important to note that the significance enhancement of Brönsted acid sites is also confirmed by the rise of a sharp Raman band at 804 cm^{-1} associated to WO_3-NPs.

Moreover, 20 wt.% WO_3 is chosen to study the influence of calcination temperatures as shown in Figure 2-9b. For calcination at 600 °C, the presence of a single band at 1440 cm^{-1} reveals that exclusively Lewis acidity exists on the catalyst. The band remains comparable after calcination at 700 °C coexisting with a weak band at 1540 cm^{-1} linked to Brönsted acidity. Later on, this band significantly grows as the catalyst is calcined at 800 °C followed by a noticeably decay after thermal exposure to 900 °C. Furthermore, the quantification of surface acid species is summarized in Figure 2-10b. The concentration of Brönsted acid sites gradually increases along with the calcination temperatures from 600 to 700 °C. An abrupt improvement of Brönsted acid sites takes place at 800 °C followed by a significant decline for a calcination at 900 °C. Low calcination temperatures lead to higher specific surface area with lower ρ_W. The catalyst calcined at 600 °C exhibits a specific surface area of 111 m^2/g, which corresponds to 3.6 W/m^2. Therefore, more uncovered ZrO_2 domains with a higher number of unsaturated Zr^{4+} can be encountered. Together with an increasing calcination temperatures, the uncovered domains of ZrO_2 decline leading to the rise of Brönsted acidity. The concentration of Brönsted acid sites finally reaches a maximum at 800 °C with a WO_x dispersion as high as 7.7 W/nm^2. However, a harsher thermal treatment at 900 °C (16.4 W/nm^2) causes a considerable decrease of Brönsted acidity due to massive formation of WO_3-NPs.
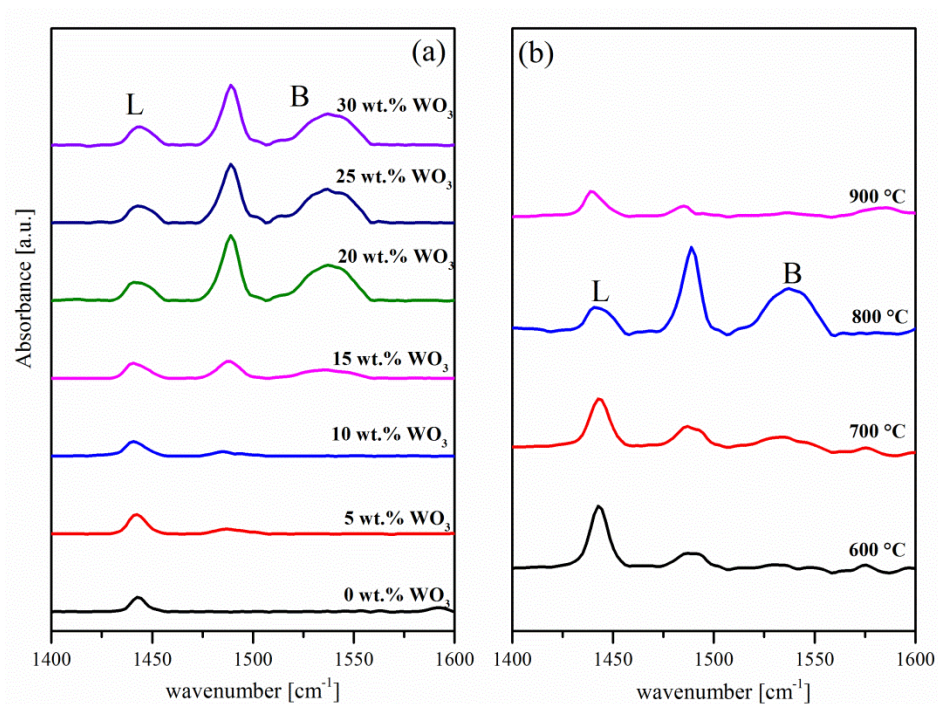
Figure 2-9. DRIFT-pyridine spectra for catalysts with different WO₃ loadings (a) and 20 wt.% WO₃ loading treated at different calcination temperatures (b)

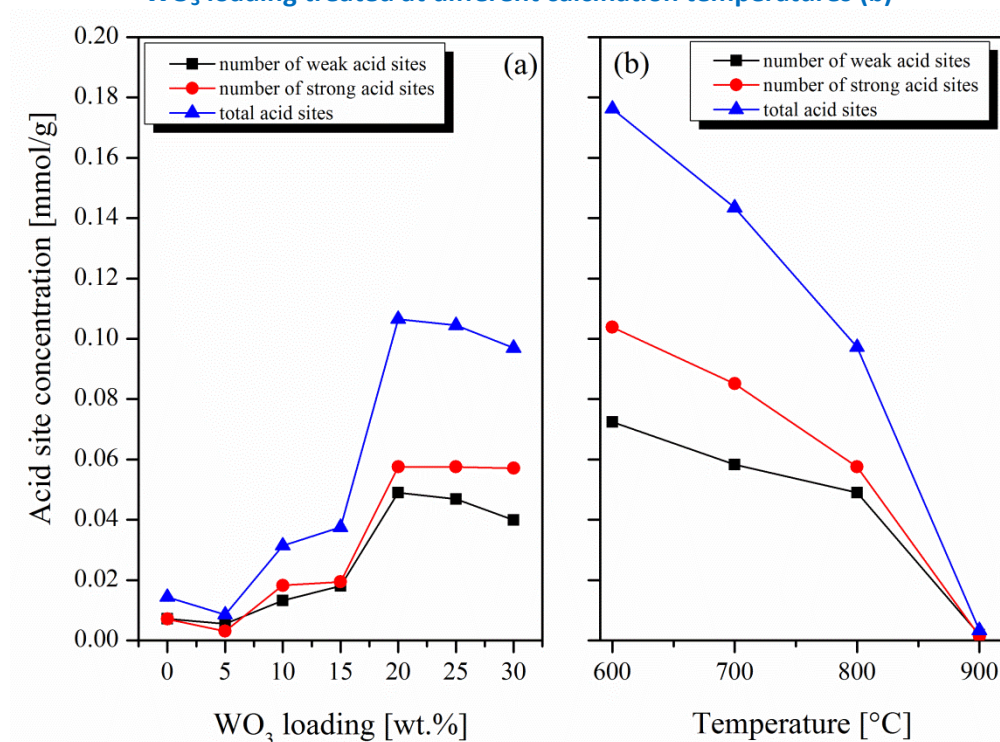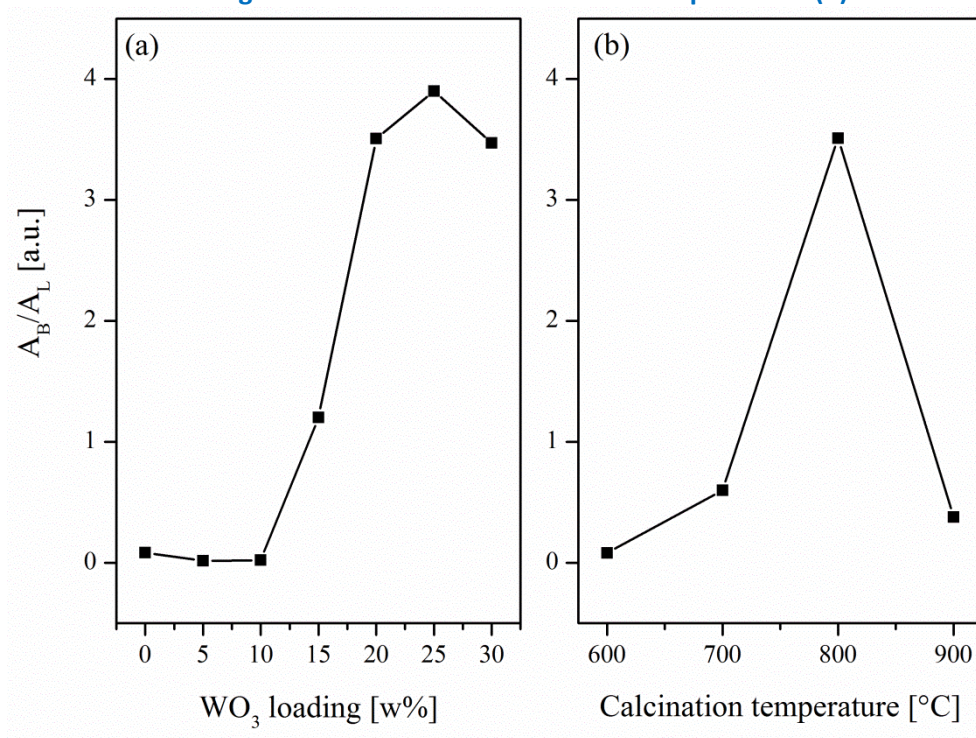**Figure 2-10. B/L ratio for the catalysts with various WO₃ loadings (a) and 20 wt.% WO₃ loading treated at different calcination temperatures (b)**

2.2.7 Catalytic activity

2.2.7.1 Pretest
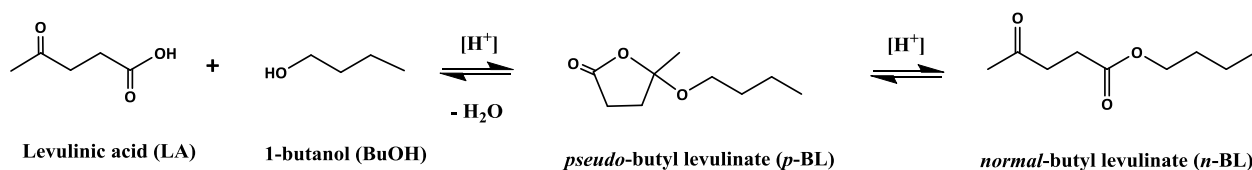
Scheme 2-1 Esterification of levulinic acid with 1-butanol

Butyl-levulinates are a derivative of levulinic acid (LA) which can be produced from renewable biomass. In this study, butyl levulinates are synthesized from LA and 1-butanol (1-BuOH) over WmZr catalysts as depicted in Scheme 2-1. Before going further to investigate the catalytic activity, a number of blank test was firstly performed recalling that LA is a weak acid with a pKa of 4.59. These blank tests indicate that LA can also catalyze the reaction contributing to a distinct blank activity in LA esterification as presented in Figure 2-11. For all reactions, only two products are formed namely *pseudo*- (*p*-BL) and *normal*-butyl levulinate (*n*-BL). However, esterification proceeds slow in the absence of catalyst. 8 % total yield of butyl levulinates with 37% *n*-BL selectivity is attained as the reaction for a catalyst-free reaction at 80 °C. Increasing reaction temperatures to 100 and 120 °C obviously produces more ester products with 14 and 31 % yield, repsectively. Not only the total yield, but also *n*-BL selectivity improves at higher temperatures. *n*-BL is generated consecutively from *p*-BL, which has been reported previously by Al-Shaal et al [134]. It has been proposed that a higher activation energy is required to produce *n*-BL resulting in low selectivity at low reaction temperatures. Furthermore, the mechanism of LA transformation to *n*-BL will be discussed later in the next chapter of this report. The reaction can be enhanced by adding a suitable catalyst. In the presence of a catalyst, the total ester yield can be improved to 11 %. Applying higher reaction temperatures of 100 or 120 °C, ester yield of 26 and 65 % can be achieved, respectively. Furthermore, in order to clearly distinguish between blank activity and contribution of the catalyst, the so-called catalytic contribution is introduced. Table 2-2 displays the catalytic contribution which is defined as the difference of yield and selectivity as a consequence of catalyst addition.

Table 2-2 Catalytic contribution of LA esterification with 1-BuOH/LA = 2 for 2 h at different temperatures.

T [°C]	Y_{blank} [%]	Y_{cat} [%]	Cat. contribution ΔY, [%]	S_{blank} [%]	S_{cat} [%]	Cat. contribution ΔS_{n-BL}, [%]
80	8	11	4	37	64	27
100	14	26	12	75	93	18
120	31	64	33	83	98	10
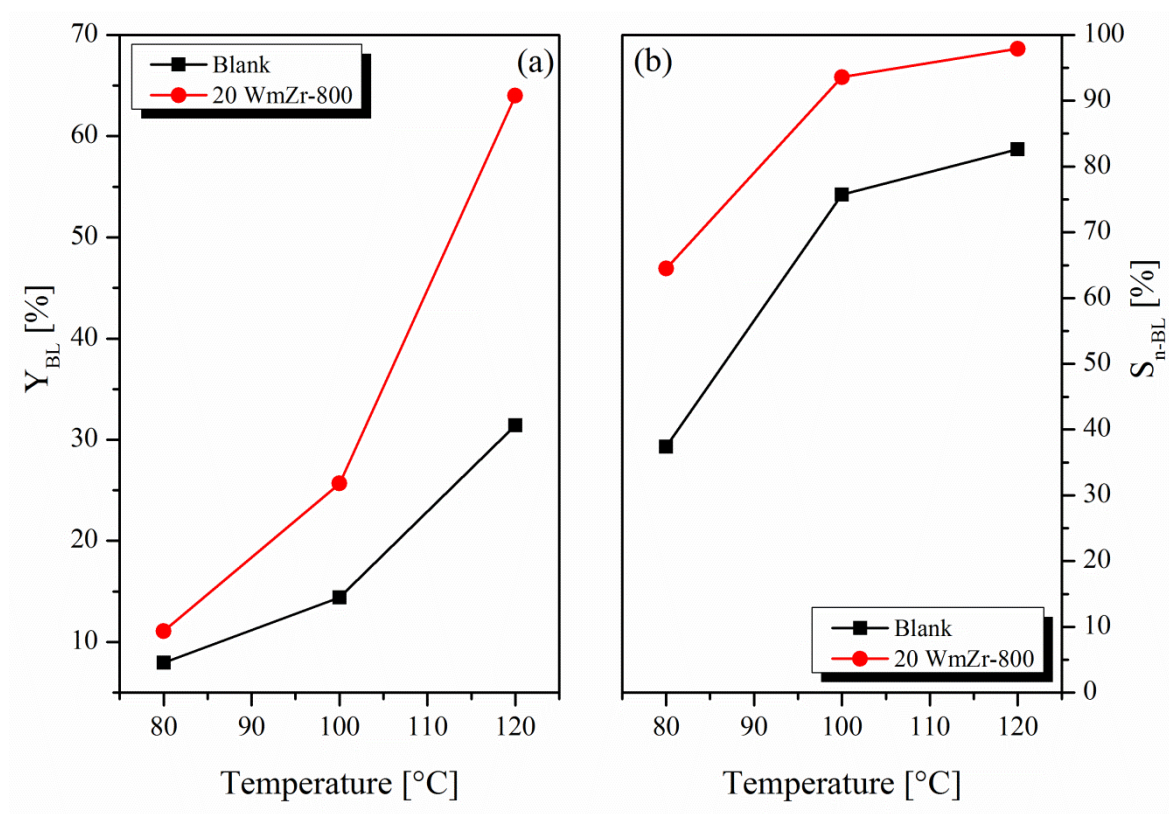
Figure 2-11. Total yield of butyl levulinates (a) and selectivity towards *normal*-butyl levulinate (b). Reaction conditions: $R_{1-BuOH/LA}$ = 2, T = 120 °C, t = 2 h , stirring rate = 750 rpm

2.2.7.2 Catalytic activity: Influence of WO₃ loadings and calcination temperatures

The activity of catalysts calcined at 800 °C with different WO_3 loadings is displayed in Figure 2-12a. The catalysts with low WO_3 loadings (0 – 10 wt.%) are only able to generate 27 – 30% total esters yield with 80 – 86% *n*-BL selectivity. In comparison to the blank test,

despite somewhat higher *n*-BL selectivity, no significant improvement of the ester yield is reached. Thus, it can be concluded that low WO_3 loadings do not provide sufficient acidity for high catalytic activity. In the presence of 15 wt.% WO_3, the total yield can be enhanced to 50 % with a higher *n*-BL selectivity of 96%. The yield further rises to 64 and 68% following an increased WO_3 loading of 20 and 25 wt.%, respectively. However, a higher WO_3 content (30 wt.%) lowers the total yield again only facilitating 58%. Concerning *n*-BL selectivity, applying catalysts containing 15 – 30 wt.% WO_3 leads to insignificant changes of selectivity, which remains constant around 96 – 98%. In principle, a direct correlation of catalytic activity to the catalytically active sites is desirable. Therefore, an effective turn over frequency (TOF_{eff}) can be introduced to clarify the independency of activity on the number of active sites. Herein, TOF_{eff} is determined by normalizing the reaction rate to the number of W atom on the catalyst. Consequently, further catalytic properties such as specific surface area, number of acid sites and ratio of Brönsted/Lewis acidity are correlated to TOF_{eff} to identify major factors controlling catalytic activity. Figure 2-13 illustrates that the catalytic activity is independent of catalysts' specific surface area. A correlation of the catalytic activity with the number of acid sites is presented in Figure 2-14. The number of acid sites moderately increases with WO_3 loading from 5 to 10 wt.% whereas the catalyst is relatively inactive at these loadings. A slight increase of acid sites at 15 wt.% WO_3 apparently triggers a substantial rise of TOF_{eff} followed by a maximum at 20 wt.%, which is in line with the improved amount of acid sites. After passing the maximum, both number of active sites and TOF_{eff} progressively decline with further increasing the WO_3 content to 25 and 30 wt.%, respectively. According to these results, it can be inferred that the activity is influenced by the number of acid sites. Interestingly, such a correlation is not valid for catalysts possessing 20 wt.% WO_3 loading and treated at different calcination temperatures (Figure 2-14b). Indeed, increased calcination temperatures result in a distinct drop of the number of acid sites while the catalytic activity rises reaching a maximum at 800 °C. This result is not in agreement with the prior hypothesis of a correlation between catalytic activity and total acid site concentration. To address this issue, the role of the nature of the acid sites has been taken into consideration. Figure 2-15a relates the influence of WO_3 loading to TOF_{eff} and A_B/A_L. At low WO_3 concentrations (5 and 10 wt.%), both A_B/A_L and TOF are very low. A marked increase of A_B/A_L at 15 wt.% is followed by a substantial rise of TOF. For loadings

between 15 and 30 wt.%, both A_B/A_L and TOF grow developing an individual maximum at 20 and 25 wt.% before they further decline at 30 wt.% WO_3 loading. However, if total yield (Figure 2-12a) is related to A_B/A_L over various WO_3 contents, an identical curve possessing a maximum at 25 wt.% will be obtained. The early formation of maximum for the TOF can be ascribed from the fact that the TOF calculation involves the normalization of the activity to the number of W atom on the catalyst leading to the lower WO_3 loading to reach the highest activity. In case of 25 wt.% WO_3, larger WO_3-NPs evolve leading to a reduced tungsten dispersion. The influence of calcination temperatures on A_B/A_L as well as TOF_{eff} is illustrated in Figure 2-15b. Within a temperature range of 600 to 900 °C, both TOF_{eff} and A_B/A_L develop maxima located at around 800 °C. This result affirms that the activity of LA esterification is highly affected by the Brönsted acid concentration. Related to the Raman spectra, the most active catalyst (20WmZr-800 with 7.1 W/nm^2) is characterized by a strong band at 714 and 804 cm^{-1} associated with the formation of sub-nanometer Zr-WO_x clusters. Moreover, the dependence of ρ_W on TOF_{eff} is depicted in Figure 2-16. After combining WO_3 loadings and calcination temperatures, a correlation between TOF_{eff} and ρ_W can be observed. The activity of the catalysts appears to be merely determined by ρ_W, which can be regulated by altering WO_3 loading and calcination temperature. The optimal ρ_W in this work (7.7 W/nm^2) is somewhat lower compared to the value reported for esterification of palmitic acid, which lays at 8.9 W/nm^2. While Lopez et al obtained a W population as low as 6.6 W/nm^2 for esterification of acetic acid with methanol [76]. Kourieh et al reported the highest conversion of fructose in the dehydration to 5-HMF for 4.3 W/nm^2.[135].
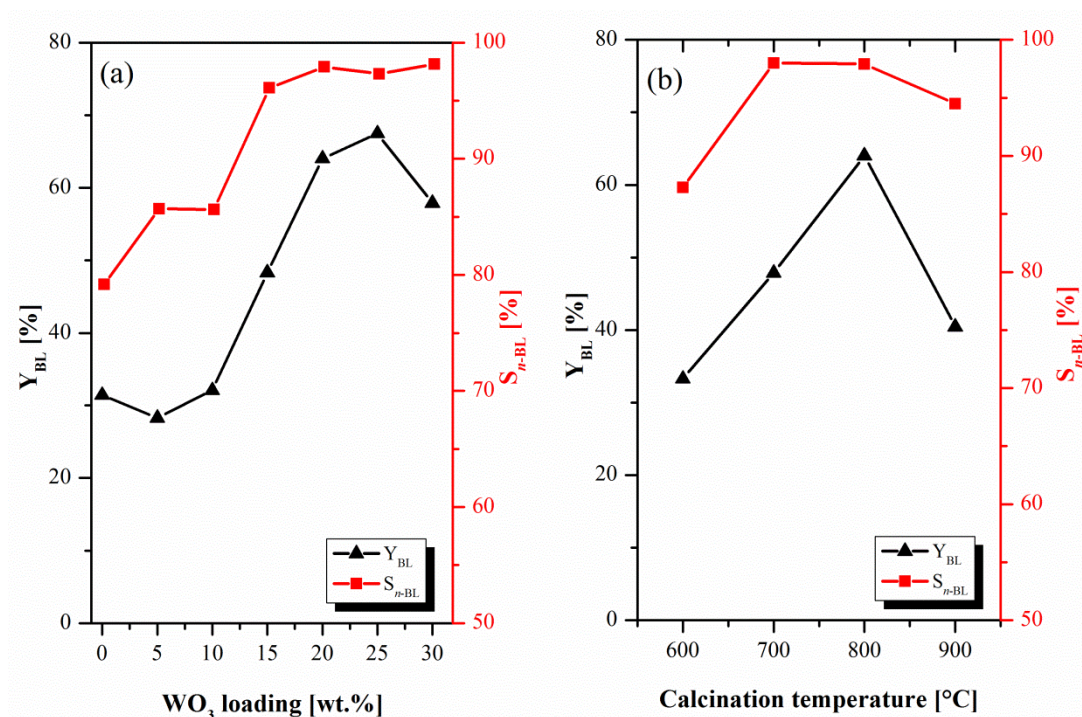
Figure 2-12. Total ester yield and *n*-BL selectivity as a function of WO₃ loading and calcination temperatures for 20 wt.% WO₃ loading. Reaction conditions: $R_{1-BuOH/LA}$ =2, 10 wt.% catalyst respective to LA, T = 120 °C, stirring rate = 750 rpm
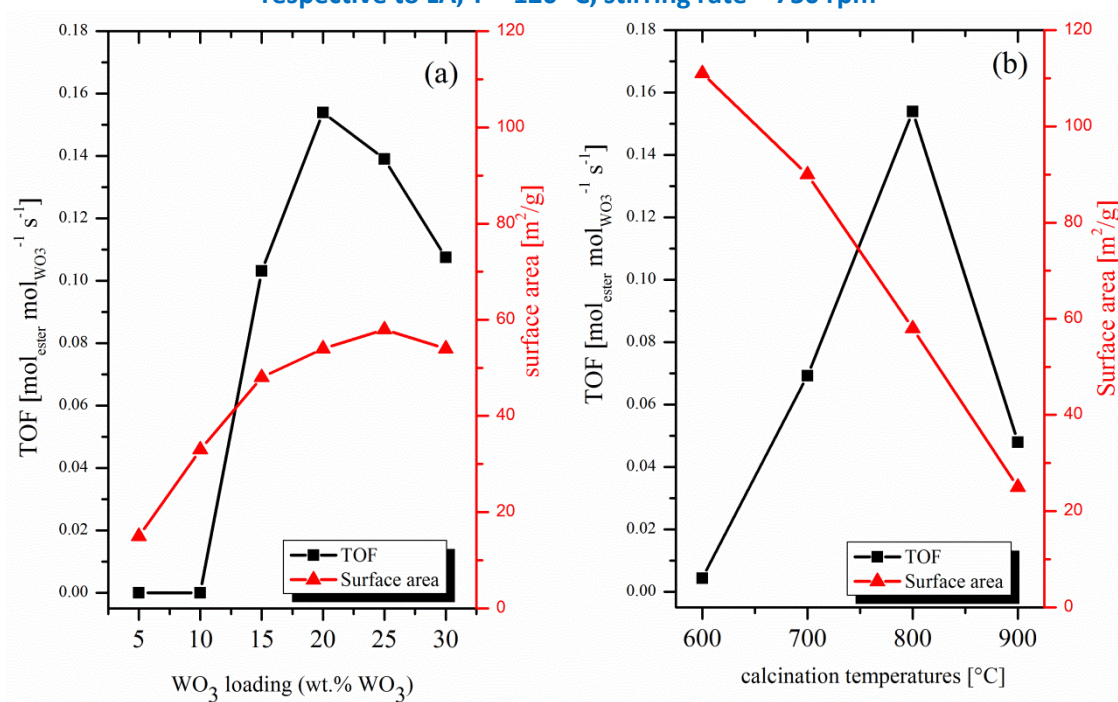
Figure 2-13. TOF$_{eff}$ and specific surface areas dependence on WO₃ loading (a) and calcination temperatures for 20 wt.% WO₃ loading (b). Reaction condtions: $R_{1-BuOH/LA}$ =2, 10 wt.% catalyst respective to LA , T = 120 °C, stirring rate = 750 rpm
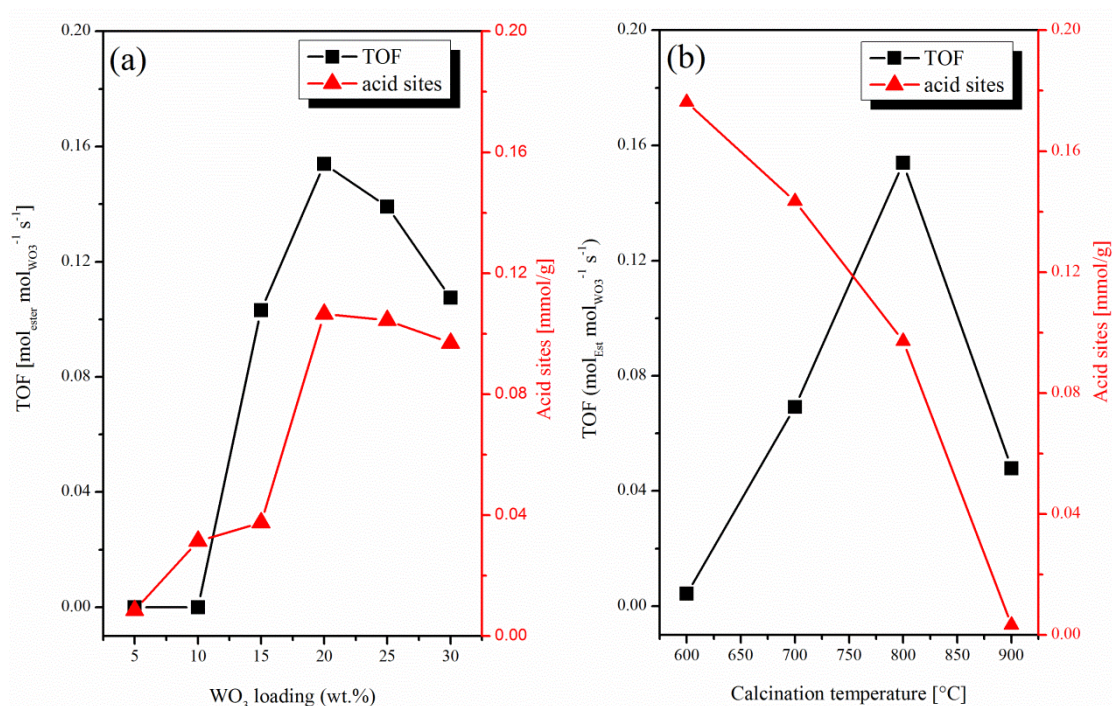
Figure 2-14. TOF$_{eff}$ and acid sites dependence on WO$_3$ loadings (a) and calcination temperatures for 20 wt.% WO$_3$ loading (b); Reaction conditions: R$_{1\text{-BuOH/LA}}$ =2, 10 wt.% catalyst respective to LA , T = 120 °C, t = 2 h, stirring rate = 750 rpm
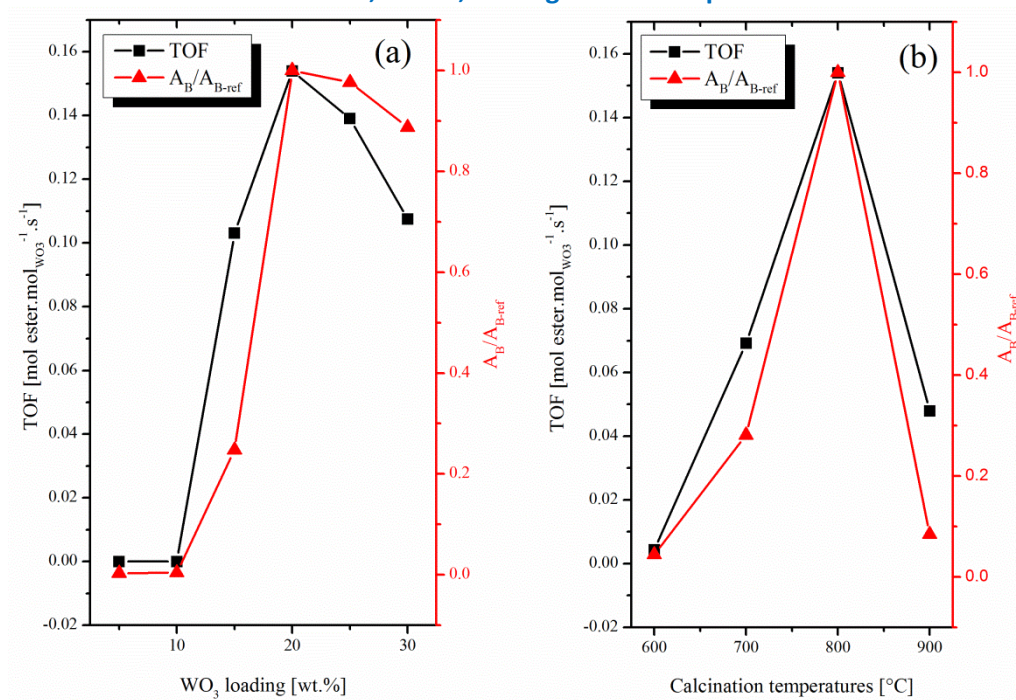
Figure 2-15. TOF$_{eff}$ and A$_B$/A$_L$ dependence on WO$_3$ loadings (a) and calcination temperatures for 20 wt.% WO$_3$ loading (b); Reaction conditions: R$_{1\text{-BuOH/LA}}$ =2, 10 wt.% catalyst respective to LA , T = 120 °C, t = 2h, stirring rate = 750 rpm
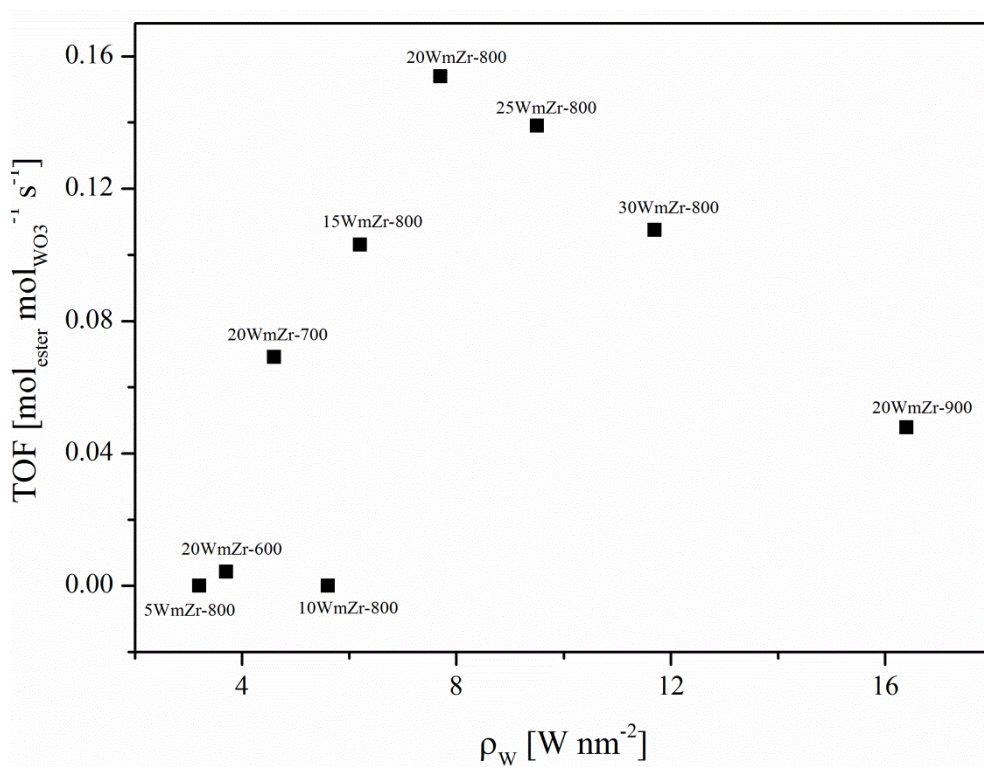
Figure 2-16. Dependence of TOF$_{eff}$ on ρ_W. Reaction conditions: R1-BuOH/LA =2, 10 wt.% catalyst respective to LA , T = 120 °C, stirring rate = 750 rpm

2.2.8   High resolution transmission electron microscopy (HRTEM)

In order to visualize the surface species, the least (5WmZr-800) and most active catalyst (20WmZr-800) are examined by STEM facilitating to acquire information from materials with better contrast. An image obtained via a secondary emission technique for the least active catalyst is shown in Figure 2-17a. W atoms with heavier atom weight are recognized by brighter speckles while fainter lattice fringes characterize the ZrO_2 surface. The image of the least active catalyst is not easy to interpret as it is difficult to discriminate the WO_x species over the support. In contrast, clearer and brighter white spots are dispersed well over ZrO_2 indicating the presence of either 2D poly-WO_x or 3D sub-nanometer WO_x clusters for the most active catalyst (Figure 2-18a). Applying the Z-contrast technique for the least active catalyst, sparsely white spots are detectable, which can be due to the formation of mono- and 2D-poly-WO_x species (Figure 2-17b). Interestingly, aggregates of brighter speckles with denser population can be seen for the most active catalyst, which might be ascribed to the formation of 3D-subnanometer WO_x clusters (Figure 2-18b). The presence of those dense bright speckles on 20WmZr-800 is suggested to cause the significantly higher activity of this catalyst compared to 5WmZr-800.
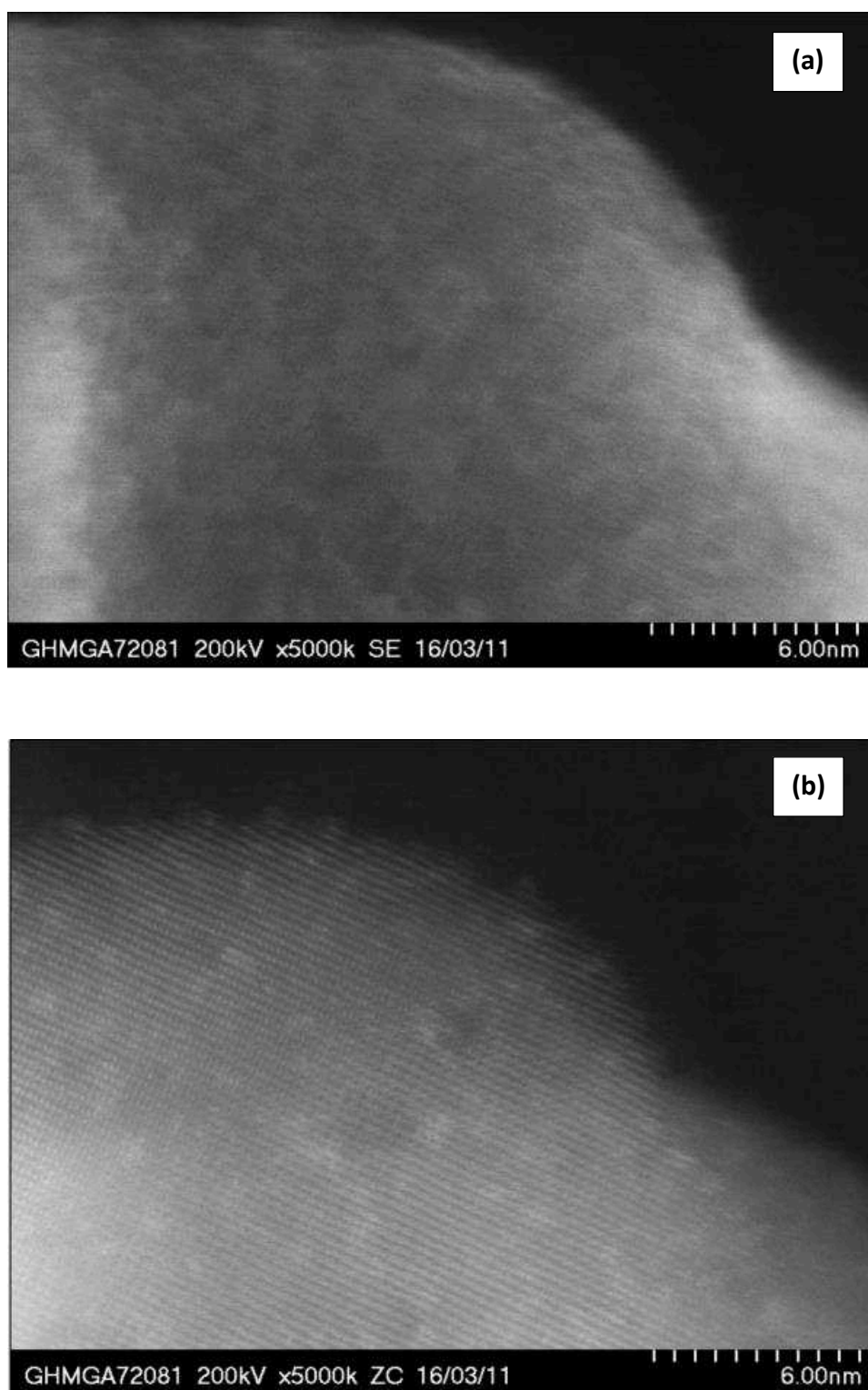
Figure 2-17. Secondary emission (a) and Z-contrast (b) of HR-TEM images of a WmZr catalyst loaded with 5 wt.% WO$_3$
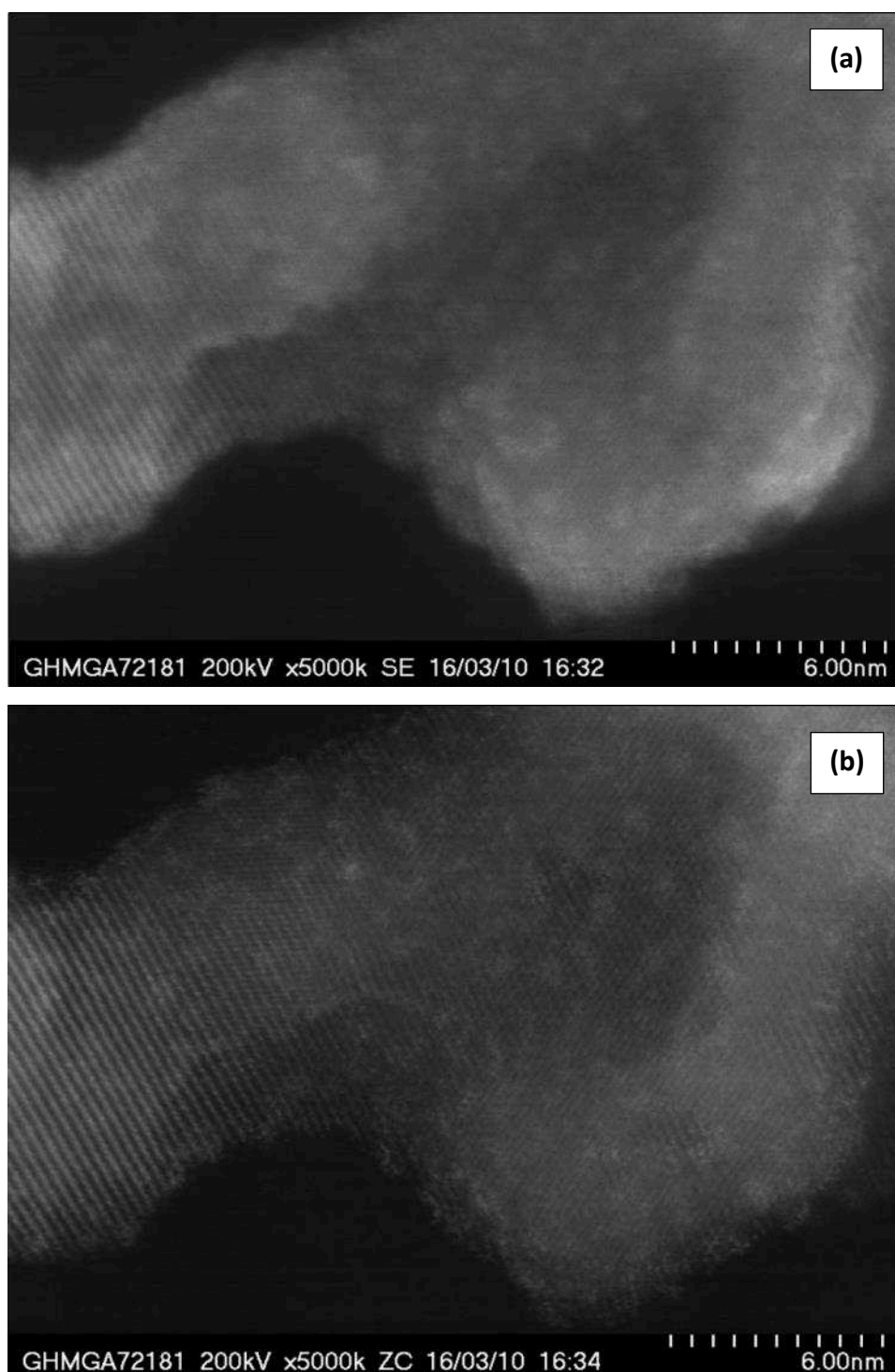
Figure 2-18. Secondary emission (a) and Z-contrast (b) of HR-TEM images of a WmZr catalyst loaded with 20 wt.% WO₃

2.2.9 Comparison with other solid acid catalysts

In order to examine the activity of the prepared catalyst in comparison to other solid acids under identical reaction conditions, the most active catalyst (20WmZr-800) and other

commercially available catalysts are tested (Figure 2-19). It is noticeable that even in the absence of catalyst, 31% total ester yield can still be achieved. Pure metal oxides such as γ-Al_2O_3 and monoclinic ZrO_2 facilitate only 29 and 31% total ester yield reflecting that these catalysts are inactive. Furthermore, pentasil zeolites with different Si/Al ratios are represented by HMFI-25 (Si/Al = 25) and -400 (Si/Al = 400) leading to 27 and 43% total yield, respectively. The difference between those two zeolites can be caused by the fact that more isolated AlO_4 tetrahedra are present on HMFI-400 and are responsible for strong Brönsted acid sites [136]. Beta zeolite (BEA) was also employed to catalyze esterification providing in general a similar total yield of LAE of 60 (HBEA-25) and 64% (HBEA-150). The higher catalytic activity of HBEA zeolites could be caused by their larger pore openings allowing the substrates and products to diffuse in and out of the catalyst. A similar result has been noted by Fernandes et al suggesting - despite the very acidic nature of HZSM zeolite - the pore structure of HBEA zeolite is decisive to enable the formation of LAE [102]. Subsequently, it can be concluded that 20WmZrO2-800 shows a similar activity to HBEA zeolites, which were reported to be the most active zeolite catalysts for LA esterification [102].
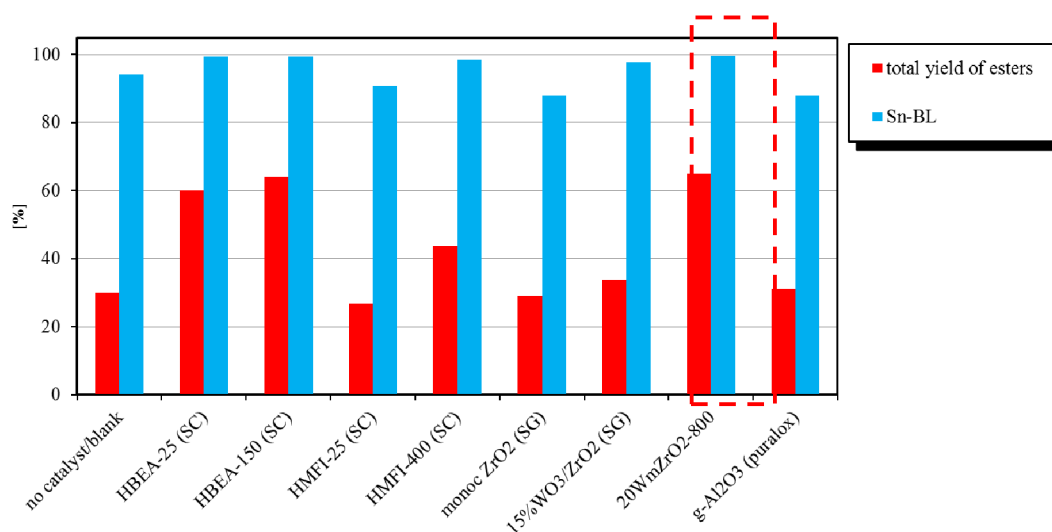
Figure 2-19. Esterification of levulinic acid over different types of catalyst. The reaction was performed for 2 h with 10 wt.% catalyst (respective to LA), $R_{1\text{-BuOH/LA}}$ = 2, 750 rpm, at 120 °C.

2.3 Summary

WmZr catalysts have successfully been synthesized by evaporation induced self-assembly. Bulk and surface structures were measured via XRD and Raman spectroscopy. The strength and number of acid sites are determined using NH_3-TPD, while DRIFT pyridine adsorption is used to investigate acid species on active centers. The catalysts are tested for LA esterification with butanol. Catalysts loaded with low WO_3 contents (0 – 10 wt.%) possess an increasing specific surface areas rising from 15 to 48 m^2/g. Those catalysts have only few acid centers, which are dominated by Lewis acidity. ZrO_2 loaded with low WO_3 contents exhibit no activity in LA esterification. Furthermore, higher loadings (15 – 30 wt%) are characterized by a relatively constant specific surface area of around 54 to 58 m^2/g. In the higher loading range, the number of acid sites and Brönsted acid centers develop a maximum at 20 wt.% (7.7 W/nm^2), which is most probably responsible for the highest activity in LA esterification. Indeed, Brönsted acid site concentration proceeds in well agreement to the activity in LA esterification reaching the highest TOF at 20 wt.% WO_3 loading. Calcination temperature also plays a significant role for catalytic activity. Increasing the calcination temperatures from 600 to 900 °C causes a significant drop of specific surface area and the number of acid centers whereas the number of Brönsted acid sites and TOF rises up to 800 °C before it considerably declines for a calcination at 900 °C. Thus, according to the results, it can be affirmed that the catalytic activity of WmZr in LA esterification is highly determined by the population of Brönsted acid sites.

Chapter. 3 Production of levulinic acid esters from α-angelica lactone over different solid acid catalysts

3.1 State of the art

Levulinic acid esters (LAEs) have been so far synthesized via esterification of levulinic acid (LA) with alcohols (R-OH). A typical LA esterification can be expressed in Equation 3-1 as well as 3-2. Esterification itself is well known to be an equilibrium reaction and consequently thermodynamically limited. Therefore, an excessive amount of substrate has to be introduced to drive the reaction towards full product formation. Another technique to run the esterification being far away from the equilibrium is by harvesting the just formed products via either continuous extraction or distillation.

$$LA + R-OH \overset{k_1,k_2}{\Longleftrightarrow} LAE + H_2O \qquad \textbf{(Equation 3-1)}$$

$$K_{eq} = \frac{[LAE]\,[H_2O]}{[LA][R-OH]} \qquad \textbf{(Equation 3-2)}$$

α-Angelica lactone (a-AL) is the dehydration product of levulinic acid, which can be considered as a new biogenic platform chemical. Recently, Al-Shaal et al found that applying a-AL as substrate, 97% γ-valerolactone (g-VL) selectivity with full conversion of a-AL can be attained at an appreciably mild reaction temperature (50 °C) [137]. Cao et al also observed that g-VL can be produced at even room temperature from a-AL over Pd/C with the assistance of ionic liquids [138]. Thus, it can be hypothesized that the compound derived from LA might be more efficiently prepared employing a-AL as the substrate. From the perspective of process feasibility, the prospective platform chemical, a-AL, can be produced continuously over a Ru/C catalyst under inert atmosphere at a temperature as low as 50 °C [139]. As catalyst, montmorillonite, was applied to dehydrate LA under vacuum condition at 165 °C resulting a mixture of α- and β-angelica lactones with 100 % total yield [140]. 97% total yield with 64% α- and 33% β-angelica lactone selectivity can be harvested from LA over a H-ZSM5/SiO₂ catalyst under reduced pressure (0.01 MPa) at 130 °C. Although more studies

are required to optimize a-AL production, efficient conversion accompanied by simple synthesis of a-AL promises novel transformations within a potential bio-refinery. Those advantageous features have motivated us to investigate another derivatization of a-AL to high added value compounds such as LAEs. Recalling the equilibrium issue for LAEs production, the use of a-AL becomes prospective. Manzer patented the production protocol of LAEs from a-AL with various alcohols over different solid acids [97]. While much earlier, Langlois et al reported that pseudo-LAE can be derived during the addition of a-AL with different alcohols [141]. Nonetheless, the influences of alcohols, acid catalysts and reaction mechanisms hitherto have not been comprehensively investigated yet.

3.2 Result and discussion

3.2.1 Temperature effect on LAE formation

The addition of a-AL and 1-BuOH was carried out at different temperatures. The effect of temperature on the a-AL conversion and product distribution are summarized in Table 3-1. Full conversion can be reached in less than 30 min as a low temperature (50 °C) was applied. Higher temperatures (75 and 100 °C) considerably enhance a-AL conversion with full conversion in about 10 min. Increased temperatures substantially alter the product distribution. Two isomers of butyl levulinate, pseudo- (*p*-BL) and normal-butyl levulinate (*n*-BL), are observed. For a reaction at 50 °C up to 120 min, a significant formation of *p*-BL can be noticed. Thereafter, this compound progressively disappears along with time leading to the enrichment in *n*-BL. In addition, trace formation of β-angelica lactone (b-AL), γ-methylene-γ-butyrolactone (g-BL), and 2,4-pentadienoic acid occur in the reaction mixtures. Similar results are also observed for higher reaction temperatures. However, it is important to note that the disappearance of *p*-BL is faster at higher temperatures. For instance, only 10 and 0.1% *p*-BL yield can be detected after 60 min at 75 and 100 °C, respectively; whereas at 50 °C, the *p*-BL yield reaches up to 27.8% after 120 min. From the facts above, it can be concluded that *p*-BL undergoes a consecutive transformation to n-BL and the transformation is enhanced at higher temperatures. Moreover, levulinic acid is also developed during the reaction. The formation of this compound might be caused by the existence of small amounts of water on the catalyst leading to the hydration of a-AL. Noteworthy, the

formation of LA is lowered at higher temperatures, which may be due to the enhanced esterification of LA to *p*- and *n*-BL.

Table 3-1. The addition of a-AL with 1-BuOH over A-36 at different temperatures and reaction times, reaction conditions: $R_{1\text{-BuOH}/a\text{-AL}}$ = 1, T = 75 °C, stirring rate = 350 rpm

T	t	$X_{a\text{-AL}}$	Yields [%]		
[°C]	[min]	[%]	*n*-BL	*p*-BL	LA
	30	99.4	18.1	67.2	4.8
50	120	100	62.0	27.8	10.5
	330	100	89.3	1.8	9.5
	10	99.7	42.1	50.1	6.9
75	60	100	79.8	10.0	9.3
	240	100	94.0	1.0	5.2
	10	99.7	68.5	30.4	2.2
100	30	100	91.4	5.3	2.8
	60	100	98.4	0.1	2.1

3.2.2 Influence of different alcohols on the LAEs formation

The effect of alkyl chain length can be studied by comparing different alcohol substrates, in this case ethanol, 1-butanol and 1-octanol (shown in Table 3-1 and

Table 3-2). As for ethanol and 1-butanol, full conversion of a-AL was possible after 10 min reaction. In case of n-octanol the time until full conversion prolonged to 60 min. Furthermore, two LAE isomers can be noticed for three of the alcohols. After 10 min reaction, 45 and 50% yield of pseudo-ethyl (*p*-EL) and *p*-BL are observed. However, 52.9 % pseudo-ester of octyl levulinate still exists even after 60 min emphasizing that for linear alcohols the longer alkyl chain the more difficult is the formation of the normal-ester. Additionally, to gain insight into the difference in activity between linear and branched alcohols, 1-BuOH and *iso*-propanol (*i*-PrOH) were investigated. Applying the linear alcohol, full conversion of a-AL can be attained within only 10 min whereas with the branched alcohol 120 min was demanded to completely consume a-AL. The production of normal-ester is also influenced by the linearity of alcohols. For instance, 42.1% yield of normal-butyl levulinate can be obtained after 10 min while 40.5% yield of normal-iso-propyl levulinate is

achieved within 40 min. Those facts finally lead to the conclusion that the reactivity of branched alcohol is lower than that of the linear one. This is because the branched alcohol gives more stearic hindrance making the functional groups less reactive.

Table 3-2. Influence of alcohols on a-AL addition over A-36 at 75 °C. Reaction conditions: $R_{1\text{-BuOH/a-AL}}$ = 1, T = 75 °C, stirring rate = 350 rpm

Alcohol/R-OH	t	$X_{a\text{-AL}}$	Yields [%]		
	[min]	[%]	Normal-ester	Pseudo-ester	LA
Ethanol	10	99.1	43.0	45.0	11.1
	180	99.2	91.3	0.1	7.8
n-octanol	60	99.8	33.1	52.9	13.9
	300	100	93.8	0.5	5.0
Iso-propanol	40	98.9	40.5	40.5	11.6
	120	99.3	75.8	3.4	19.7

3.2.3   Influence of substrates

Considering the potential application of a-AL to replace LA, these two substrates then will be compared under identical reaction conditions. For this purpose, LA and a-AL were reacted with ethanol as illustrated in Figure 3-1. 72.8% LA substrate is converted progressively after extending the reaction to 240 min. Noteworthy, only trances of *p*-EL are formed in the course of the reaction indicating a very high selectivity towards normal-ethyl levulinate. Starting the reaction with a-AL as substrate, full conversion is attained immediately. A prolonged reaction time of 240 min leads to full conversion of a-AL together with 92.2% n-EL yield and trace amounts of p-EL. It is notable that LA exists during the reaction in a relatively constant level, which could indicate that water might be present in the system allowing hydration of a-AL.
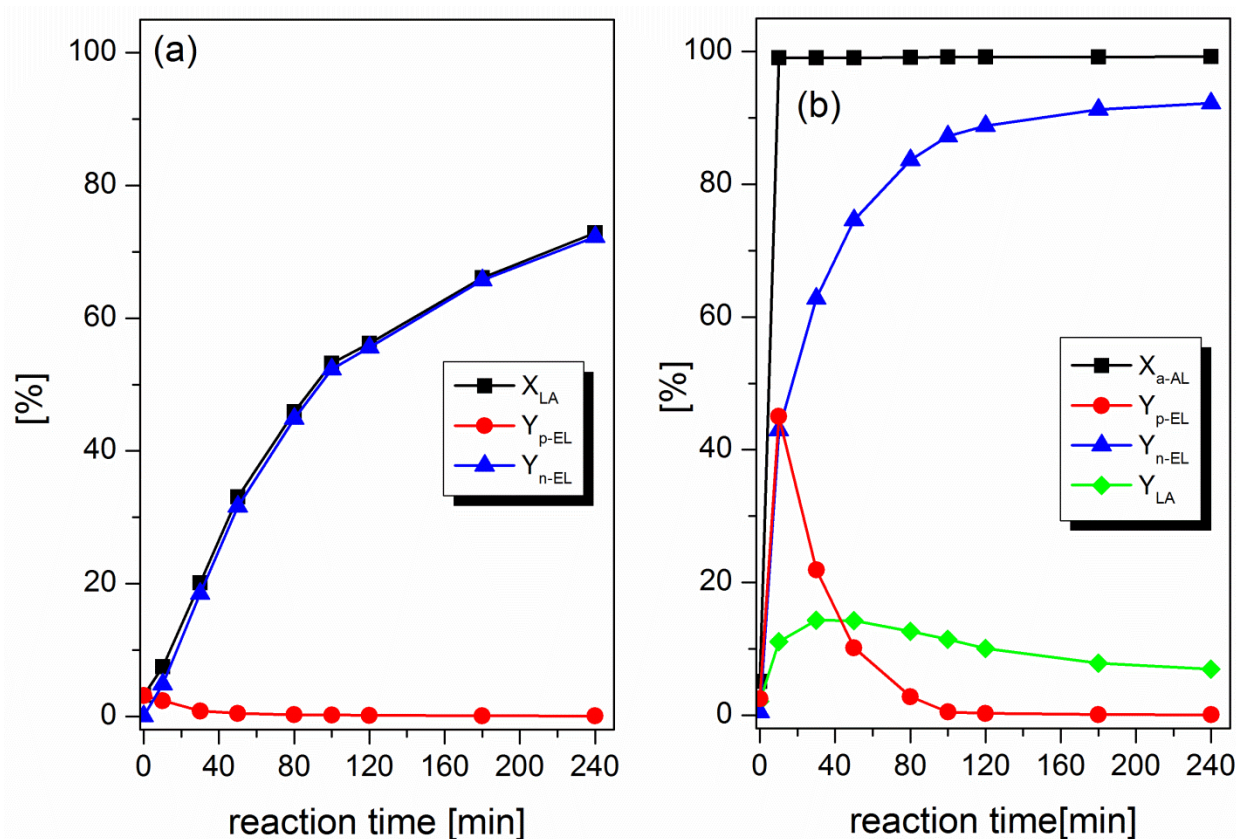
Figure 3-1. Time resolved formation of ethyl levulinate from levulinic acid (a) and α-angelica lactone (b) with stoichiometric amounts of EtOH (1 to 1) at 75 °C over A-36 as catalyst applying 350 rpm agitation rate.

Furthermore, the esterification of LA with different alcohols was also performed as given in Table 3-3. The same trend also applies in this case. Again longer times are necessary to transform LA with longer alkyl chain alcohols. The reaction of LA and a-AL with ethanol is illustrated in Figure 3-1. As a-AL was used as the substrate, 90% yield of n-EL could be rapidly formed in 120 min whereas with LA the yield of n-EL is only as high as 60%. Additionally, 100% conversion of a-AL is attained in a considerably short time. Beside the esters, LA is also generated as a by-product during the addition of a-AL. LA is an undesired product developed during the addition of a-AL most probably as a consequence of a-AL hydration. To address this observation, experiments were carried out aiming for an understanding of the influence of water addition on LA formation. Therefore, kinetic studies of a-AL addition with 1-BuOH were carried out without (Figure 3-2) and deliberately with initial H_2O addition (Figure 3-3). Generally, for both systems a-AL is easily converted reaching full conversion just after 10 min.

Table 3-3. Esterification of LA with different linear alcohols (LA/alcohol mole ratio of 1) at 75 °C over A-36 as catalyst under 350 rpm agitation rate.

Alcohol	t	X_{LA}	Yield [%]	
	[min]	[%]	Normal-ester	Pseudo-ester
EtOH	180	66.1	65.8	0.1
1-BuOH	240	56.3	56.1	0.2
1-OctOH	300	42.1	41.3	0.7

However, the impact of H_2O addition on the product distribution is remarkable as 5 and 10 mol.% H_2O (respective to a-AL) were introduced. In the presence and absence of H_2O the system can quickly develop 44 – 53% *p*-BL yield within 10 min. For the H_2O free system, the yield of *p*-BL depletes substantially to 10 % in 60 min whereas for the same reaction time, the yield is still 28 % as a result of H_2O loading. The delayed conversion of *p*-BL consequently results in lower *n*-BL formation over time. Meanwhile, different H_2O loadings do not significantly alter the final yield of *p*- and *n*-BL. Concerning LA development, the system with no water addition develops only about 7.4 % LA yield during reaction. Even a small addition of H_2O is able to considerably rise the average LA yields to 28.3 and 33.5 following the addition of 5 and 10 mol.% H_2O, respectively. Interestingly, for all cases, LA yield is relatively constant throughout the course of the reaction. A potential explanation could be that a large amount of LAE has simultaneously been produced preventing the further conversion of LA to its corresponding esters. Overall, the presence of water substantially influences the reaction. H_2O has particularly a negative effect on esters formation due to LA release, which causes again an equilibrium situation in ester formation.
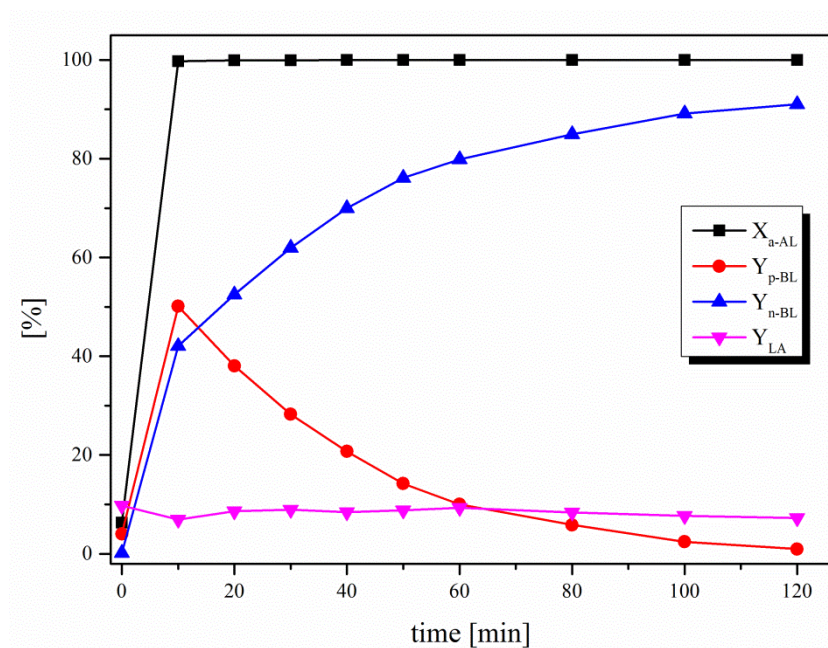
Figure 3-2. addition of a-AL with 1-BuOH ($R_{a\text{-}AL/1\text{-}BuOH}$ = 1) over A-36 at 75 °C applying stirring at 350 rpm
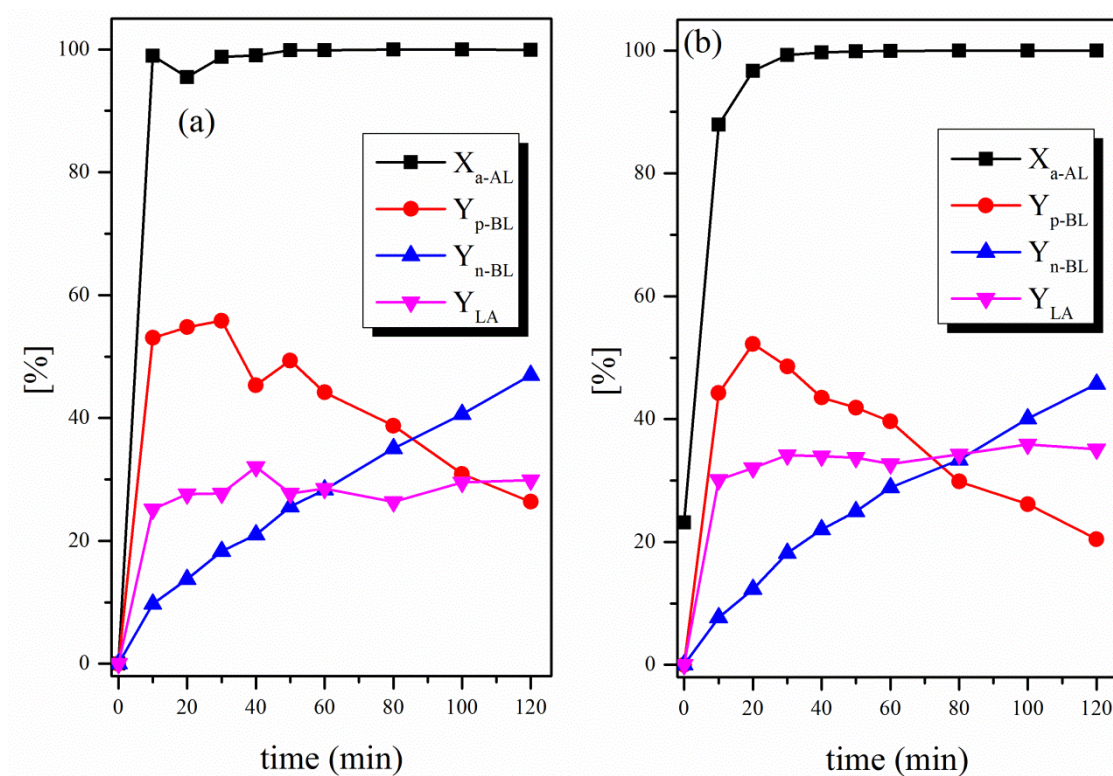

Figure 3-3. Effect of an addition of 5 (a) and 10 mole.% H_2O (b) on the formation of LA. Reaction conditions: $R_{1\text{-}BuOH/a\text{-}AL=1}$, at 75 °C, stirring rate of 350 rpm.

3.2.4 a-AL addition over different solid acid catalysts

Up to this point, an extensive study related to the reaction conditions has been conducted to conclude on the mechanism of LAE production via a-AL. However, it is also interesting to investigate the influence of different types of catalysts on the addition of a-AL. To realize this investigation, three different classes of catalysts namely sulfonated polymers, zeolites and modified ZrO_2 will be used to initiate the reactions. The activity of different solid acid catalysts is summarized in Figure 3-4. Two sulfonated polystyrenes so called Amberlysts-15 (A-15) and -16 (A-36) demonstrate similar kinetic profiles. Complete consumption of a-AL is attained within only 10 min reaction followed by a high yield of *n*-BL (95%) after 120 min reaction. It is important to note that the composition of products does not change with extended reaction times longer than 120 min. In addition, a relatively constant yield of LA of around 10% can be observed. Furthermore, two commercial ZrO_2 catalysts, SO_4^{2-}/ZrO_2 (SZr) and 15 wt.% WO_x/ZrO_2 (WZr) are appreciably less active than Amberlysts. Performing the reaction for 360 min, 90% a-AL conversion together with the 88% yield of *p*-BL could be achieved confirming a high selectivity towards *p*-BL over WZr. Interestingly, a very different kinetic profile is obtained for SZr. SZr facilitates a rapid consumption of a-AL within 30 min for full conversion. *P*-BL yield also quickly reaches the maximum of 82% before it gradually declines accompanied by the formation of *n*-BL. Noteworthy, unlike SZr, only a small amount of *n*-BL is generated over WZr. H-BEA zeolites with a Si/Al ratios of 150 (HBEA-150) and 25 (HBEA-25) are also studied concerning their activity in the a-AL addition. Both zeolites demonstrate comparable conversion of a-AL in which 90 min reaction is required to completely consume a-AL. These two catalysts also achieve the highest yield of *p*-BL of 80 % after 70 min reaction time. Nevertheless, HBEA-150 exhibits a faster decline of *p*-BL compared to HBEA-25. An extended reaction time to 360 min results in only trace amounts of *p*-BL for HBEA-150, while the *p*-BL yield is still as high as 25 % for HBEA-25. Regarding LA formation, despite lower activity both the investigated zeolites and the ZrO_2 based catalysts only produced traces of LA. In contrast, the use of A-36 as the catalyst leads to the appreciable formation of water which can be due to the high moisture content of A-36. The used A-36 in this work contains approximately 55 wt% H_2O. Despite evacuation under vacuum at 60 °C overnight was applied to evacuate the water, such a treatment seems not to be able to completely remove water from A-36. Eventually, the bound water contributes

in the hydration of a-AL to LA. In addition, pure metal oxides, monoclinic ZrO_2 (mZr) as well as γ-Al_2O_3, were also tested exhibiting no activity in the addition reaction of a-AL.

To correlate catalytic behavior with material properties, the acidity and specific surface areas of catalysts are measured for different types of catalysts as presented and summarized in Figure 3-5 and Table 3-4. The acidity of the catalyst is determined by NH_3-TPD. Because of limited thermal stability, no NH_3-TPD measurement was carried out for A-36. The concentration of acid sites was provided by the supplier showing noticeably higher acid density on this catalyst compared to other types of catalyst responsible for its superior catalytic performance. For both zeolite based catalysts, NH_3 molecules are released over a wide desorption temperatures covering a range between 150 and 600 °C. Such a broad feature indicates that acid sites of different acid strengths are present. Nevertheless, these two zeolites demonstrate different desorption profiles. HBEA-25 demonstrates very intensive NH_3 desorption creating a distinct peak and a broad shoulder. Applying a deconvolution technique, two overlapping peaks were identified possessing maxima at 250 and 400 °C, which are assigned to weak and strong acid centers, respectively. In contrast to HBEA-25, HBEA-150 desorbs a lower amount of NH_3 molecules and two distinct peaks with maxima at 210 and 450 °C can be differentiated. Quantification of desorbed NH_3 molecules suggests that HBEA-25 possesses a significantly higher acid concentration than HBEA-150. This could be due to the higher Al^{3+} content in HBEA-25. Evaluating acid strength, it becomes evident that HBEA-25 exhibits a substantially higher fraction of strong acid sites compared to HBEA-150. Despite these stronger acid sites, HBEA-25 is less active than HBEA-150 in the addition reaction. Next, various types of ZrO_2 catalysts will be discussed. Generally ZrO_2 based catalysts hold a very broad desorption profile. Unlike zeolites with distinct acid centers, ZrO_2 catalysts often result in multiple overlapping peaks. In order to discriminate the acid strength, peaks located below 350 °C are assigned to weak acid sites, while those at higher than 350 °C are assigned as strong acid cites. TPD spectra and acid sites quantification suggests that SZr contains a higher amount of acid centers than mZr and WZr. This finally leads to significantly higher activity of SZr in a-AL addition. Interestingly, despite the greater acid number than HBEA-150, the activity of SZr is inferior to HBEA-150. From above discussion, it can be deduced that the activity of a-AL is less dependent on the number of acid sites. Nevertheless, applying strong acids such as Amberlysts, HBEA zeolites and SZr

alleviate the development of *n*-BL. Furthermore, the influence of specific surface area will be related as well. In spite of comparable specific surface area of HBEA-25 and -150, more *n*-BL is produced over HBEA-150 after 360 h. The same case applies as well for ZrO_2 catalysts. Although the three ZrO_2 catalysts possess similar specific surface areas of $100 - 121 \text{ m}^2/\text{g}$, they have very different catalytic activity. These results indicate that the catalytic activity is independent to the catalyst surface area . Therefore, further investigations related to other factors influencing activity such as the nature of surface acid species will be considered and studied elsewhere.
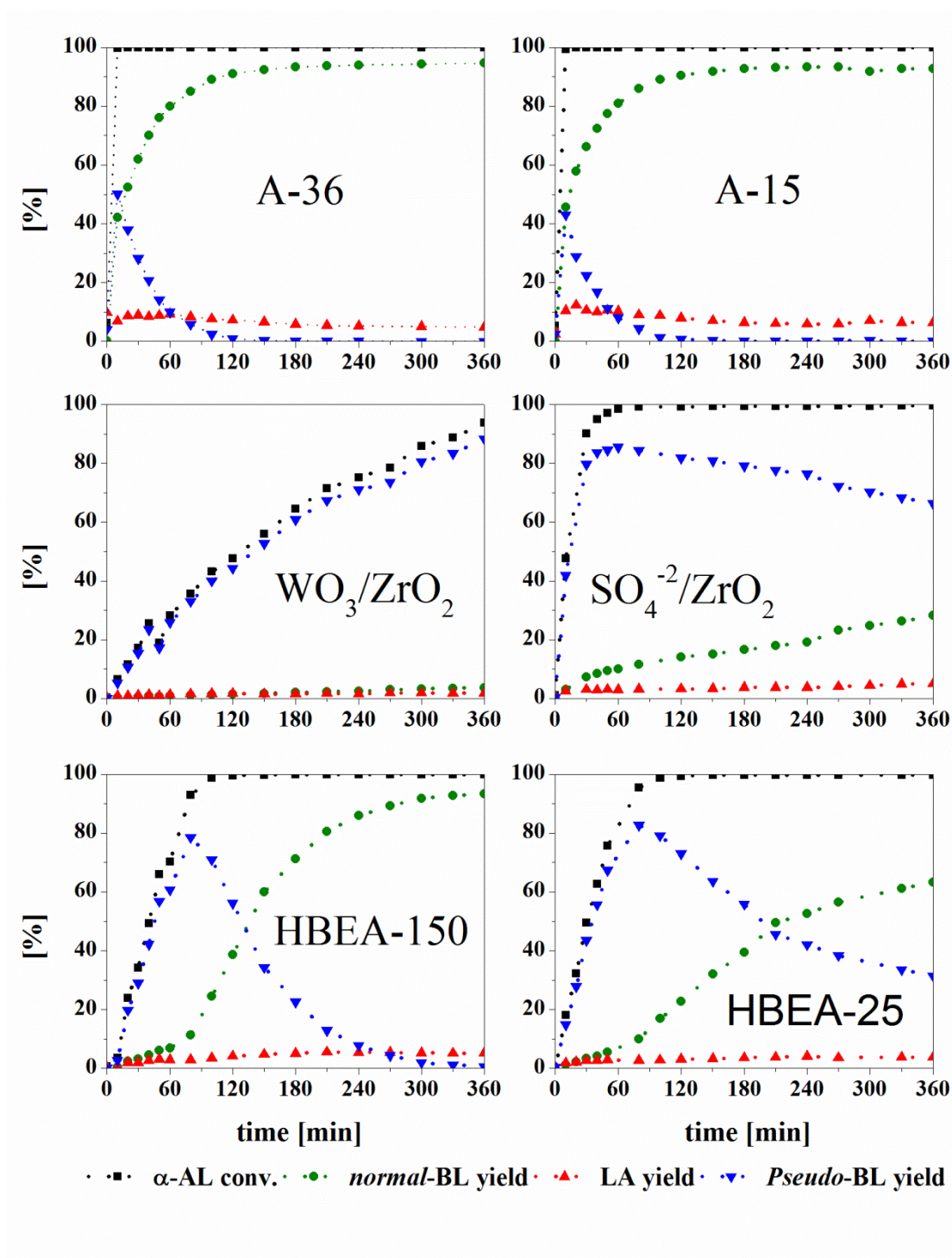
Figure 3-4. Addition of a-AL to 1-BuOH over different catalysts. Reaction conditions: $R_{1\text{-BuOH/a-Al}} = 1$, $T = 75$ °C, stirring rate = 350 rpm
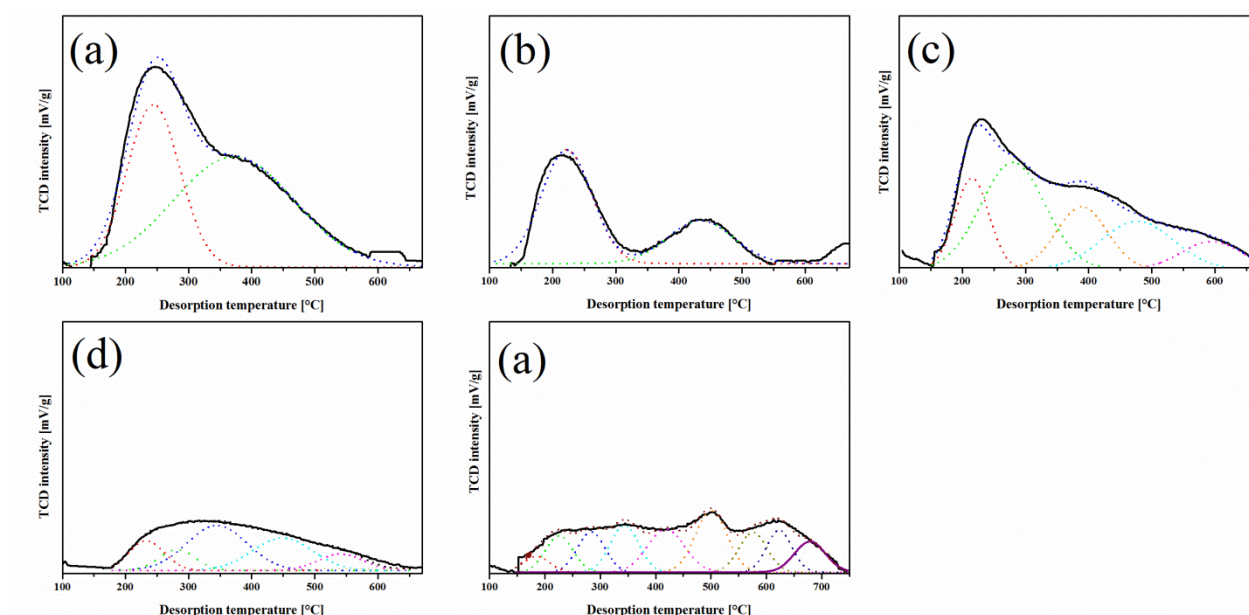
Figure 3-5. NH$_3$-TPD of commercial (a) HBEA-25, (b) HBEA-150, (c) SO$_4^{2-}$/ZrO$_2$, (d) 15 wt.% WO$_x$/ZrO$_2$ and (e) monoclinic ZrO$_2$

Table 3-4. Textural properties and surface acidity of different solid acid catalysts

Catalysts	surface area [m^2/g]	weak acid [mmol/g]	strong acid [mmol/g]	total acidity [mmol/g]	strong acid density x 10^{-3} [mmol/m^2]	weak acid density x 10^{-3} [mmol/m^2]	total acid density x 10^{-3} [mmol/m^2]
HBEA-25	502	0.52	0.08	0.60	1.03	0.17	1.20
HBEA-150	577	0.15	0.07	0.22	0.26	0.12	0.37
WO$_x$/ZrO$_2$ (WZr)	103	0.16	0.04	0.20	1.59	0.39	1.99
SO$_4^{2-}$/ZrO$_2$ (SZr)	121	0.17	0.12	0.29	1.38	0.99	2.38
monoclinic ZrO$_2$ (mZr)	102	0.11	0.00	0.11	1.30	0.00	1.30
Amberlyst-36	104	NA	NA	5.4	NA	NA	51.98

3.2.5 Proposed reaction mechanism and activation energy

Based on the previously discussed results, it is clear that *p*-BL is an intermediate product subsequently further transformed into *n*-BL. Moreover, carrying out the addition reaction at higher temperatures, the decline of *p*-BL becomes more rapid implying that *n*-BL formation requires high activation energy. In order to gain a clearer insight, a rigorous kinetic study is required at various temperatures over A-36 catalyst for 360 min as depicted in Figure A2-2 to Figure A2-4. For the reaction performed at 50 and 75 °C, the conversion of a-AL is accompanied by the development of high amount of *p*-BL particularly for the first 50 min. Over time, the amount of *p*-BL declines with the increase of *n*-BL yield implying a consecutive transformation from *p*- to *n*-BL takes place. Elevating the reaction temperatures also affects the maximum yield of *p*-BL. An increase of temperature from 50 to 75 °C decreases the maximum yield of *p*-BL from 88 to 66%, respectively. Furthermore, as the reaction was conducted at 100 °C, only 32% maximum yield of *p*-BL can be reached. This investigation also enables us to determine the activation energy for each transformation steps. The Arrhenius' plots are then presented in Figure 3-6 leading to the values of 3 and 50 kJ/mol for the activation energy of *p*- and *n*-BL formation, respectively. It suggests that the subsequent transformation from *p*- to *n*-BL requires considerably higher energy than that from a-AL to *p*-BL. Thus, it leads to a solid conclusion that stepwise transformation from a-AL to *n*-BL is accompanied by the production of *p*-BL intermediate. The transformation of *p*- to *n*-BL exhibits higher activation energy and can be facilitated by rising the reaction temperatures or applying another catalyst. As we mentioned in Sub-Chapter 3.2.1, the addition reaction of a-AL generates trace amounts of β-angelica lactone (b-AL), γ-methylene-γ-butyrolactone (g-BL), and 2,4-pentadienoic acid (2,4-PDA) in the final product mixtures. To study a complete mechanism, pure a-AL was heated at 75 °C in the presence of A-36 as illustrated in Figure 3-7. A kinetic plot of a-AL conversion confirms that b-AL and g-BL exist at constant yields throughout the reaction course implying that a-AL undergoes isomerization. Nevertheless, it has to be noted that the final product solution exhibits a brownish color and some precipitates settle down on the bottom of the flask. This can be an indication that high molecular weight products form as a result of polymerization. These results finally lead to the reaction network for the transformation of a-AL over acid catalysts illustrated in Scheme 3-1. In the presence of alcohol and water, a-AL is transformed to LAE and LA, respectively. In

the absence of alcohols, a-AL undergoes isomerization resulting in the formation of b-AL and g-BL. Particularly, for b-AL, the presence of protons enables ring opening leading to the development of 2,4-PDA and further polymerization of b-AL to high-molecular weight products. Additionally, if an alcohol exists in the reaction, esterification of 2.4-PDA may lead to the generation of 2,4-pentadienoic acid ester (2,4-PDAE). A double bond present at the end of the alkyl chain of 2,4-PDA and -PDAE facilitates self-condensation of the compounds to produce polymers most probably responsible for the brownish color and precipitates in the solution.
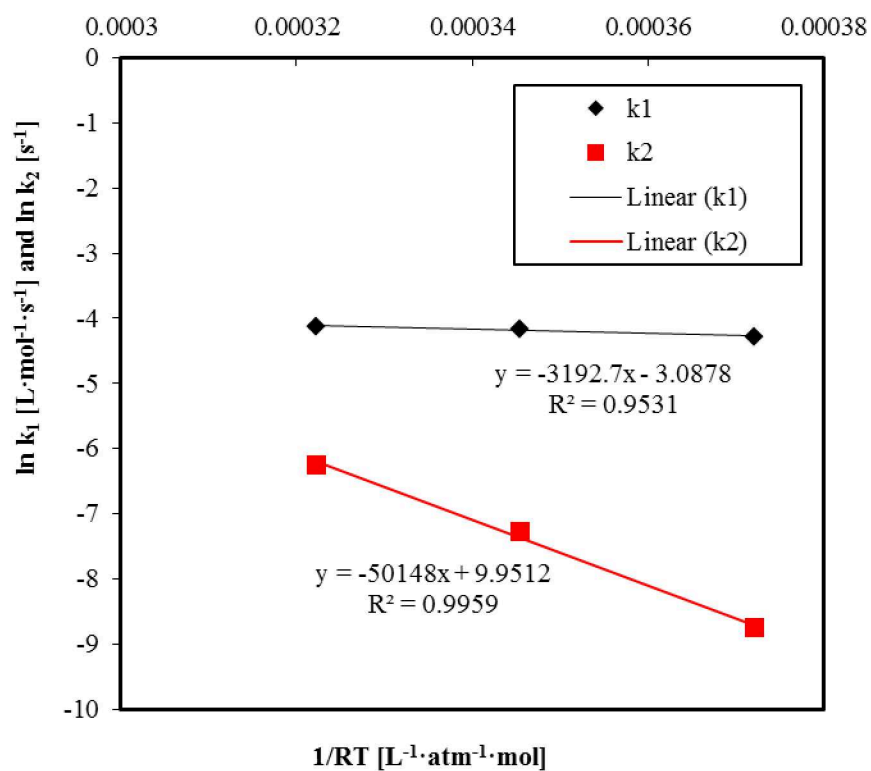
Figure 3-6. Activation energy for the formation of *p*-BL and *n*-BL. A low slope of k_1 indicates that the transformation of a-AL to *p*-BL takes place without energy barrier over A-36
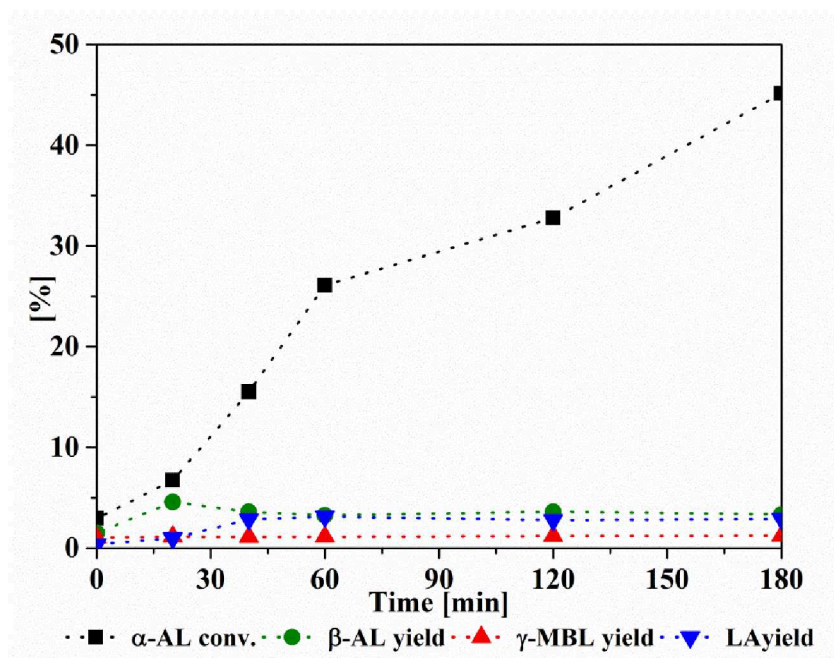
Figure 3-7. Isomerization of a-AL over 5 wt.% A-36 at 75 °C
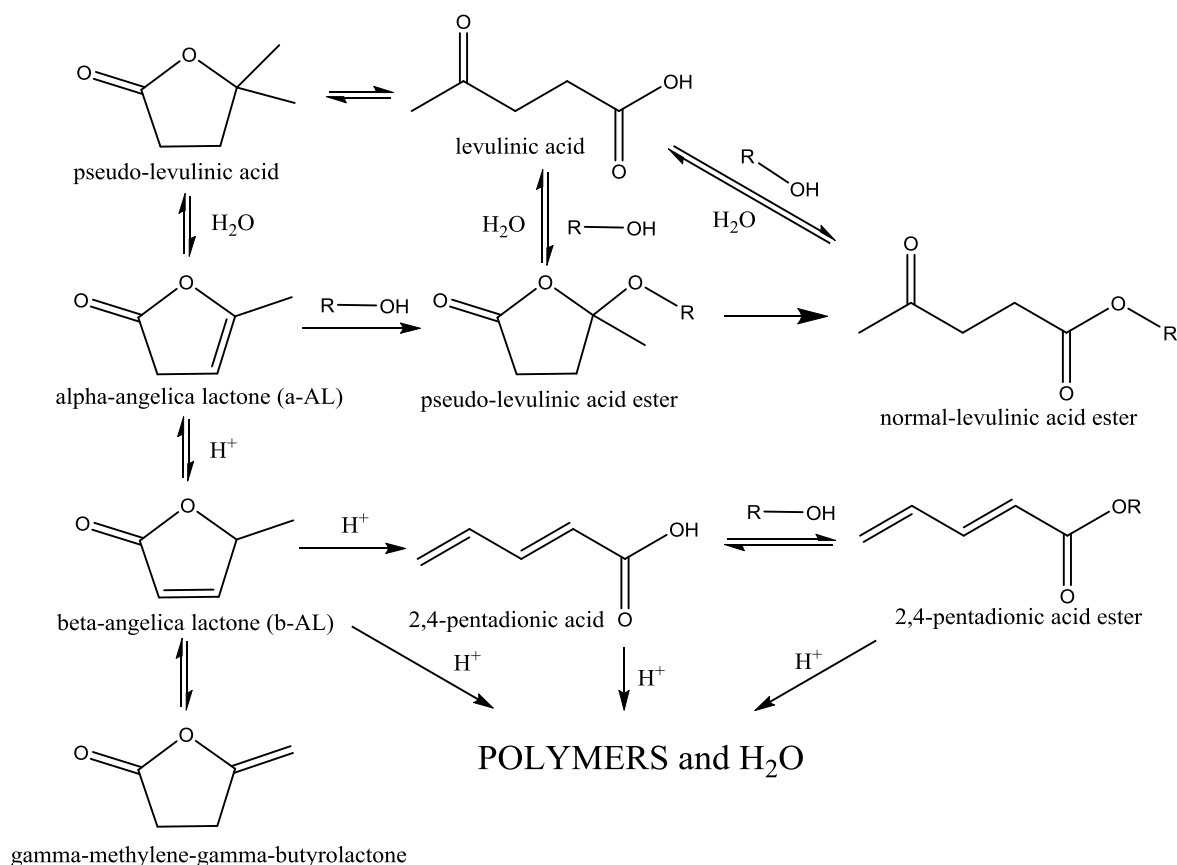
Scheme 3-1 Proposed reaction mechanism of a-AL transformation in the presence of acid catalysts.

3.2.6   Summary

The addition of alcohols to a-AL has been carried out over different solid acids resulting in the development of two ester products namely p- and n-LAEs, respectively. Experiments with temperature variations confirm that the transformation of a-AL to n-BL takes place via the formation of p-BL. The conversion of p- to n-BL is enhanced with increased temperatures. Furthermore the transformation of a-AL is influenced by the type of alcohols. Longer chain and more branched alcohols tend to delay the reaction due to the steric hindrance issue. LA behaves differently than LA in the synthesis of LAE. Full conversion at much shorter reaction time and higher n-BL yield can be achieved employing a-AL while the existing equilibrium characteristic of LA esterification causes sluggish conversion and considerably lower yield of n-BL. The presence of H_2O gives a negative impact on the yield production because of the development of undesired LA during the reaction. Different activity and product distribution are resulted as a consequence of using different solid acid

catalysts. Catalysts with stronger acidity like Amberlysts, zeolites and sulfated zirconia tend to generate a higher n-BL yield whereas WO_x/ZrO_2 catalyst with moderate acidity prefers producing p-BL with high selectivity. Nonetheless, weak correlation of activity with the number acid sites and acid strength for strong acid catalyst is obtained directing to a further investigation on the role of acid species in the next study. Furthermore calculated activation energy reveals that the formation of n-BL is the most energy demanding. According to the proposed reaction mechanism, over solid acid catalyst and in the absence of alcohol, a-AL can undergo isomerization to b-AL and g-BL. The former is potentially converted to 2,4-PDA and further suffers polymerization responsible to the brownish final product mixture and the observed precipitation.

This page is intentionally left blank

Chapter. 4 WO$_x$/ZrO$_2$ in the production of levulinic acid ester from α-angelica lactone - a potential bio-based platform chemical

4.1 State of the art

In chapter 2, the esterification of levulinic acid (LA) to levulinic acid ester (LAE) has been studied affirming a high dependency of catalytic activity on Brönsted acid concentration. These Brönsted acid sites can apparently be controlled by altering synthesis parameters such as WO$_3$ loadings and calcination temperatures. In Chapter 3, the potential of different commercial solid acids in the formation of LAEs via addition of alcohols to a-AL has been in the focus providing the potency of a-AL as a new biogenic platform chemical. Interestingly, employing a-AL, milder reaction conditions are required emphasizing that it can efficiently act as the substrate for LAEs production. Strong acid catalysts such as Amberlysts, H-BEA zeolites and SO$_4$/ZrO$_2$ were able to generate *n*-BL, whereas weak-moderate acidic WO$_x$/ZrO$_2$ (WZr) catalysts facilitate *p*-BL formation with considerable selectivity. Nonetheless, for strong acid catalysts, the number of acid sites as well as acid strength do not agree well with the resulting activity. Another catalyst property namely the nature of acid sites so far has not been been discussed in the addition of a-AL. In Chapter 2 we have successfully prepared WZr catalysts with controllable Brönsted to Lewis acid ratio by adjusting the synthesis parameters. It finally motivates us to utilize WZr catalysts to investigate the influence of the acid nature on the addition of a-AL. In order to realize the investigation, WZr with various W loading calcined at 800 °C will be applied as the catalysts. Additionally, the influence of synthesis method will be also studied by comparing the catalytic activity of WZr prepared by EISA and wet impregnation route.

4.2 Result and discussion

4.2.1 Isothermal N$_2$-physisorption

N$_2$ physisorption measurement was used to study the textural properties of the prepared catalysts which are recapitulated in Table 4-1. Catalysts prepared by EISA and impregnation generally exhibit a similar trend of the specific surface area. The catalysts with no WO$_3$ loading only reach specific surface areas of 14.7 and 18.4 m^2/g for impregnation and EISA, respectively. Employing EISA, the resulting specific surface areas gradually increase from 32.5 to 54.4 m^2/g upon enhancing the WO$_3$ loading from 5 to 15 wt.%. As the WO$_3$ concentration rises from 20 to 30 wt.%, the specific surface areas remained constant in the range of 54 to 58 m^2/g. The same applies for impregnation the specific surface area increases from 41.9 to 54.5 m^2/g for WO$_3$ contents of 5 to 10 wt.%, respectively. The addition of WO$_3$ from 10 to 20 wt.% results in a relatively constant specific surface area of 51 to 55 m^2/g before it declines to 37.7 m^2/g as a consequence of 30 wt.% WO$_3$ loading. The conservation of the specific surface area along with WO$_3$ addition is caused by the reduced mobility of surface Zr atoms due to stable W-O-Zr bonds [58]. In addition, catalysts prepared via both EISA and precipitation possess pore diameters of 4.9 to 13 nm corresponding to mesoporosity. Owing to the crucial role in catalysis, the theoretical surface density (ρ_W) is also determined. ρ_W for catalysts synthesized by EISA increases from 0 (0 wt.% WO$_3$) to 11.7 W/nm^2 (30 wt.% WO$_3$). Applying impregnation, increasing WO$_3$ concentrations from 0 to 20 wt.% lead to a progressive increase of ρ_W from 0 to 9.7 m^2/g. However, a significant increase in ρ_W to 20.7 W/m^2 occurs as 30 wt.% WO$_3$ is incorporated followed by a considerable decline of the specific surface area.

Table 4-1. Textural properties of WZr catalysts with different WO$_s$ contents

Entry	Method	WO$_3$ loading [wt.%]	S$_{BET}$ [m^2/g]	D$_{pore}$ [nm]	V$_{pore}$ [cm^3/g]	ρ_W [W$_{atoms}$/nm^2]
1	EISA	0	14.7	13.0	0.05	0.0
2	EISA	5	32.5	8.1	0.06	3.2
3	EISA	10	47.7	6.5	0.08	5.6
4	EISA	15	54.4	5.5	0.08	6.2
5	EISA	20	57.7	6.0	0.09	7.7
6	EISA	30	54.4	7.1	0.09	11.7
7	Impregnation	0	18.4	6.3	0.02	0.0
8	Impregnation	5	41.9	4.9	0.05	3.1
9	Impregnation	10	54.5	7.0	0.08	4.8
10	Impregnation	15	51.7	5.3	0.07	7.5
11	Impregnation	20	53.6	5.1	0.07	9.7
12	Impregnation	30	37.7	7.0	0.06	20.7

4.2.2 X-ray diffraction for catalyst characterization

Bulk properties of the resulting catalysts are examined by XRD as presented in Figure 4-1. Polymorphic zirconia is represented by reflections at 2 θ of 29.0, 35.3, 50.1, 60.2, and 62.9 for tetragonal as well as 28.2, 31.5, and 34.5° for the monoclinic crystal phase. The coexistence of monoclinic and tetragonal phase occurs for unloaded ZrO$_2$ prepared by both methods. It is notable that the catalyst prepared via EISA consists mainly of the tetragonal phase while the monoclinic phase dominates for impregnation. Employing EISA, already 5 wt.% WO$_3$ addition leads to disappearance of monoclinic reflections. Furthermore, the diffraction patterns of ZrO$_2$ do not substantially alter with WO$_3$ contents. For impregnation, reflexes associated to monoclinic ZrO$_2$ can still be detected up to 10 wt.% WO$_3$. The reflections corresponding to monoclinic ZrO$_2$ vanishes for 15 – 30 wt.% WO$_3$ loadings. These results suggest that EISA hinders the transformation from tetragonal to monoclinic ZrO$_2$. A higher stability of the tetragonal ZrO$_2$ phase in EISA is caused by the fact that W atoms are well tethered in the ZrO$_2$ lattice as a result of the one pot preparation route. Consequently, more energy is required to repel them out to the support surface causing a delayed

formation of monoclinic ZrO_2. Moreover, the development of crystalline WO_3 can also be monitored via XRD by the emergence of diffraction peaks between 23 – 25°. No WO_3 crystal phase can be detected for any of the methods introducing 0 – 10 wt.% WO_3 during the synthesis. WO_3 nanoparticles (WO_3-NPs) emerge at 15 wt.% WO_3 for impregnation, whereas the onset of WO_3-NPs occurs at 30 wt.% for EISA. The difference of WO_3 loading at which WO_3-NPs are formed could be related to different ρ_W at comparable WO_3 content. For instance for 15 wt.% WO_3, the population of W atoms is as high as 7.5 W/nm^2 for impregnation but only 6.2 W/nm^2 for EISA. The late development of WO_3-NPs has also been observed by other researchers for one-pot co-precipitation [58].

Figure 4-1. X-ray powder diffraction patterns of catalysts prepared via EISA (a) and impregnation (b)

4.2.3   Laser FT Raman spectroscopy for analysis of surface sites

Raman spectroscopy is employed to investigate molecular surface structures of the catalysts. Tetragonal ZrO_2 can be recognized by the development of bands at 266, 315, 461 and 648 cm^{-1} while bands evolve at 220, 278, 333, 345, 380, 477, 502, 538, 559, and 617 cm^{-1} are designated to monoclinic ZrO_2. The Raman spectra for the catalysts prepared via EISA

and impregnation are illustrated in Figure 4-2. As has been previously pointed out for XRD, irrespective of the preparation methods, monoclinic and tetragonal ZrO_2 are present on catalysts containing no WO_3. It also becomes evident that bands associated to monoclinic ZrO_2 are more pronounced for impregnation, whereas EISA leads to the domination of tetragonal ZrO_2. Once WO_3 is incorporated via EISA, bands associated to monoclinic ZrO_2 are not any longer observable leaving only tetragonal ZrO_2. The feature of the Raman spectra for ZrO_2 remains almost unaltered throughout different WO_3 loadings. In contrast, monoclinic ZrO_2 still exists up to 15 wt.% WO_3 for materials prepared by impregnation, before the contribution of monoclinic ZrO_2 clearly declines for loadings higher than 15 wt.%. These facts emphasize the ability of EISA to conserve tetragonal ZrO_2, an effect potentially linked to the stronger interaction between Zr and W atoms located inside the ZrO_2 lattice. Additionally, the presence of WO_x species can be recognized by rising bands at 826 and 926 – 989 cm^{-1}. For the material produced by EISA, introducing 5 – 15 wt.% WO_3 leads to a more intense band at 826 cm^{-1} and the shift of a band at 962 to 989 cm^{-1}. The former is related to the increasing number of sub nanometer Zr-WO_x clusters [60,78] while the later corresponds to the propagation of an amorphous poly-WO_x overlayer [56,60,142]. Further WO_3 enrichment from 20 to 30 wt.% results in emerging distinct bands at 808 and 714 cm^{-1} indicating the formation of highly crystalline WO_3-NPs. The sharp band at 808 finally hides the weaker band at 824 cm^{-1}. For the Raman features of the samples prepared via impregnation, sharp and pronounced bands at 824 and 989 cm^{-1} can be obviously recognized after 5 wt.% WO_3 addition. It is important to note that no further shift is observed for the band at 989 cm^{-1}. In addition, the bands exhibit higher intensity than the ones for EISA. Along with further increasing WO_3 addition to 10 wt.%, the onset formation of WO_3-NPs is observable by the development of a weak band at 808 cm^{-1}, which superimposes the band at 824 cm^{-1}. The evolution of WO_3-NPs becomes more obvious following the introduction of 15 – 30 wt.% WO_3, which is also emphasized by the appearance of sharp bands at 714 cm^{-1}. These findings confirm that in addition to delayed formation of monoclinic ZrO_2, EISA has an ability to impede the development of WO_3-NPs.
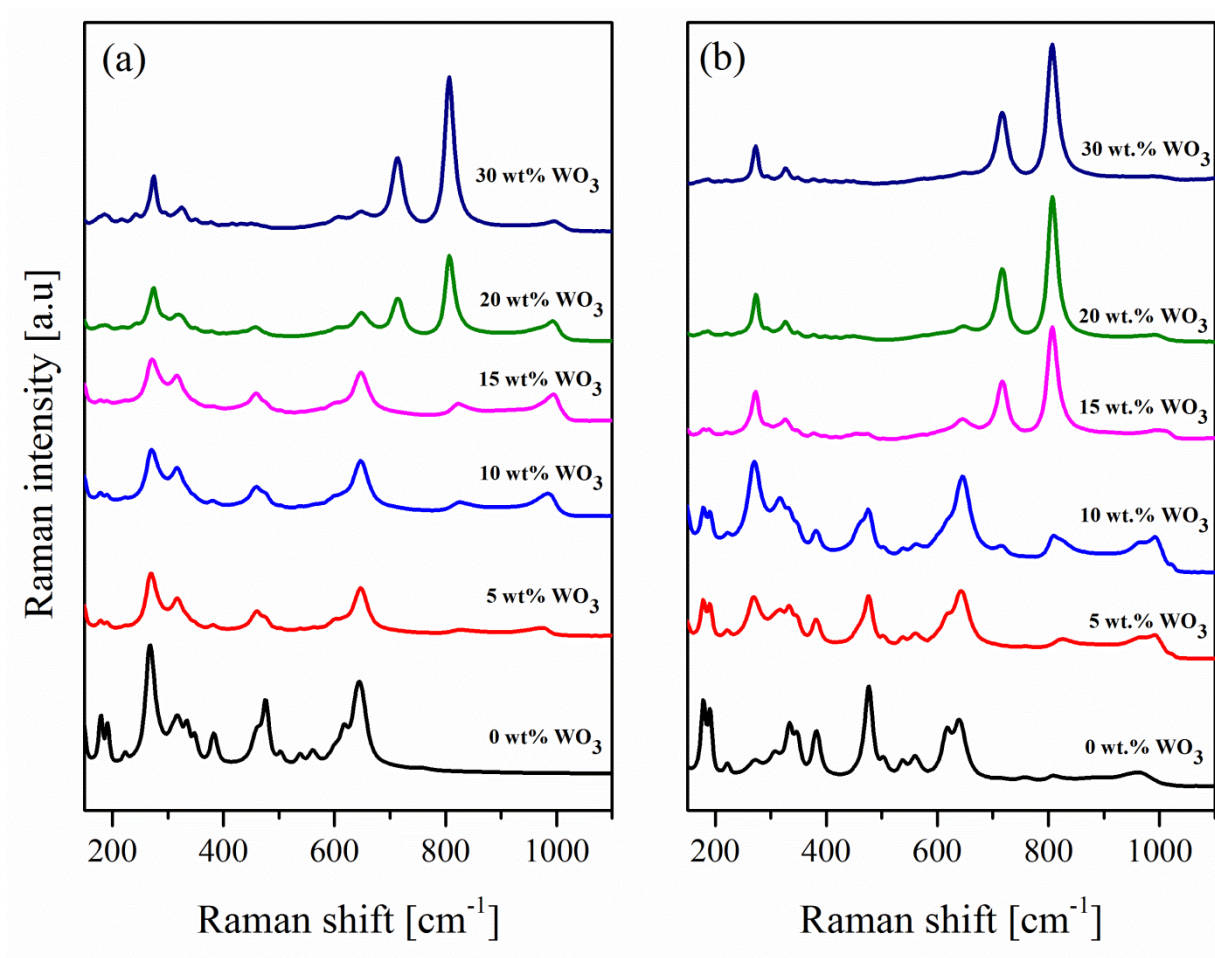
Figure 4-2. Laser FT Raman spectra for catalysts prepared via EISA (a) and impregnation (b)

4.2.4 NH$_3$-TPD for determination of surface acid sites

NH$_3$-TPD is applied to investigate the surface acidity of the catalysts as illustrated in Figure 4-3. Regardless of the preparation method, NH$_3$ is desorbed over a broad range of temperatures implying a broad acid strength present on the catalysts. For EISA, an increase of WO$_3$ loading from 0 to 20 wt.% results in an increased intensity of released NH$_3$. However, a higher WO$_3$ concentration of 30 wt.% reduces the intensity of desorbed NH$_3$. Noteworthy, the catalysts decorated with 15 − 30 wt.% WO$_3$ demonstrate an additional NH$_3$ desorption at higher temperatures (> 577 °C). A similar tendency can also be obtained for catalysts prepared via impregnation. In this case, ZrO$_2$ loaded with 0 − 15 wt.% WO$_3$ exhibits a progressive improvement of desorbed NH$_3$. The addition of 20 wt.% WO$_3$ only slightly enhances the intensity of desorbed NH$_3$ before it is appreciably reduced for 30 wt.% WO$_3$ addition. Furthermore, the difference in surface acidity from those two different routes will be evaluated. In the loading range of 0 − 10 wt.%, catalysts prepared by EISA possess a

narrower range of desorption temperatures and a weaker intensity of the ammonia desorption signal compared to the impregnation. As the WO_3 content rises to 15 wt.%, comparable desorption features appear. For both methods, 20 wt.% WO_3 loading lead to the highest amount of desorbed NH_3 followed by further depletion as the loading increases to 30 wt.%. It is notable that at 20 and 30 wt.% WO_3, EISA causes a higher intensity of the signal of desorbed NH_3 accompanied by the release of NH_3 at temperatures higher than 577 °C. In addition, no NH_3 is desorbed at temperature higher than 577 °C for impregnation.
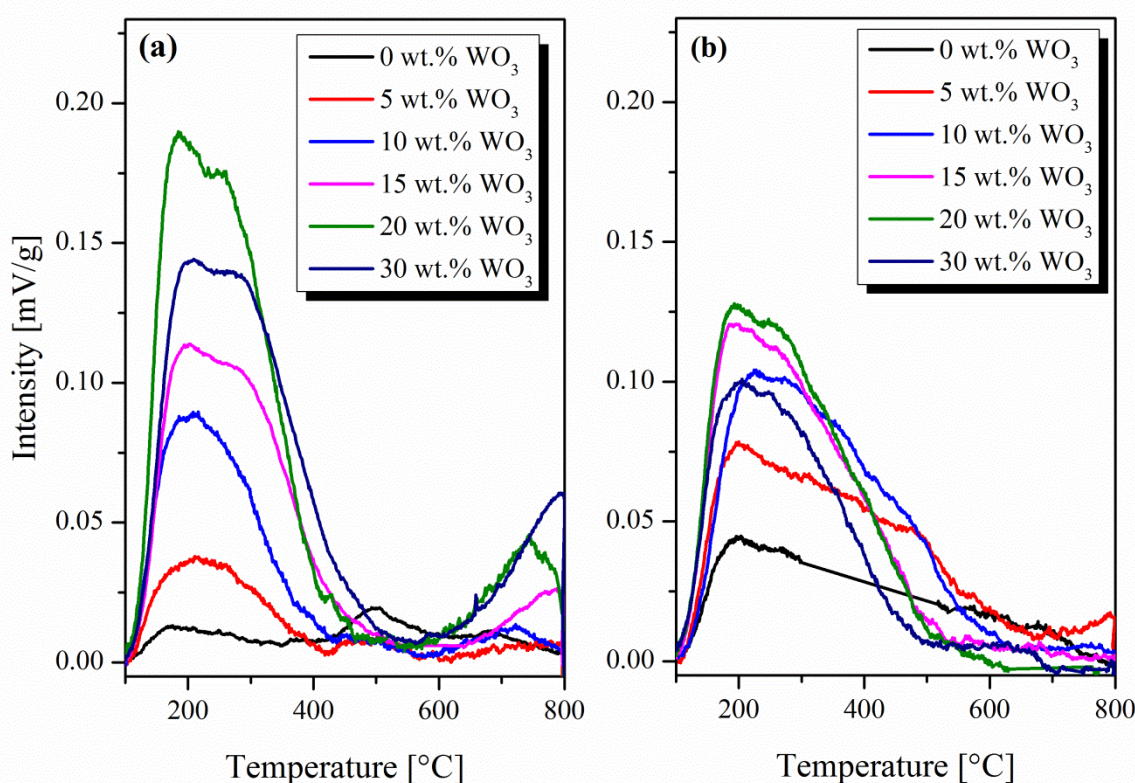
Figure 4-3. NH_3-TPD for catalysts prepared via EISA (a) and impregnation (b)

4.2.5   DRIFT with pyridine adsorption for acid site characterization

DRIFT pyridine adsorption was utilized to discriminate the nature of surface acid species. DRIFT spectra for samples with different WO_3 loadings prepared by EISA and impregnation are illustrated in Figure 4-4. Bands at 1540 and 1440 cm^{-1} indicate the presence of Brönsted and Lewis acid centers. As for EISA, a single band at 1440 cm^{-1} arises for a loading range of 0 to 10 wt.% indicating only Lewis acid sites to be present on the surface. After incorporating 15 wt.% WO_3, a weak and broad band appears at 1540 cm^{-1}

associated to Brönsted acid sites. This band further develops along with the WO_3 enrichment from 20 to 30 wt.%. It is important to note that Lewis acidity can still be witnessed for the different WO_3 loadings. Meanwhile, somewhat different results are obtained for impregnation. The evolution of Brönsted acidity can be detected as early as 5 wt.% WO_3. In a range of WO_3 content between 5 and 15 wt.% the intensification of Brönsted acid sites is accompanied by the depletion of the signals associated with Lewis acid centers. The Lewis acidity is nearly unrecognized for the sample with 15 wt.% WO_3. Furthermore Lewis acid sites can be again observed after enriching WO_3 loading to 20 and 30 wt.%. Moreover, a semi quantitative analysis is carried out enabling a further assessment of the evolution of the relative concentration of Brönsted acid centers (Figure 4-5). As for EISA, the concentration of Brönsted acid centers is very low at 0 – 10 wt.% WO_3 loading. A substantial improvement of the Brönsted acid population takes place along with an increasing WO_3 concentration from 15 – 20 wt.% before it levels off at 30 wt.% WO_3. For the impregnation, a significant increase of Brönsted acid population already occurs together with WO_3 loading from 5 to 15 wt.%. However, increased loadings from 20 to 30 wt.% decline the population of Brönsted acidity. Even higher WO_3 loadings of 20 to 30 wt.% result in an appreciable depletion of the Brönsted acid site population. For the two synthesis methods, the difference in WO_3 content for the onset of Brönsted acid site formation could be caused by the different polymerization characteristic of WO_x species over the ZrO_2 support surface. In case of impregnation, the WO_3 precursor is deposited right over the support during synthesis leading to a facile WO_x polymerization. For EISA, the condensation of WO_x species is more difficult as the one pot synthesis can trap W atoms inside the ZrO_2 lattice. Based on Raman spectra for samples prepared via EISA, a Raman shift located at 989 cm^{-1} is observable at 15 wt.% WO_3 concentration. For samples synthesized by impregnation, the band at 989 cm^{-1} is already detectable at a very low loading of about 5 wt.% and no further shift can be detected for higher WO_3 loadings. Nevertheless for those two different synthesis methods, the results from DRIFT and Raman spectroscopy emphasize that the highest population of Brönsted acidity correlates with the incipient formation of WO_3-NP. Interestingly, the highest concentrations of Brönsted acid sites, occur at 20 and 15 wt.% WO_3 for EISA and impregnation, respectively. According to Raman spectroscopy, the highest population of

Brönsted acidity is accompanied by the development of WO_3-NPs indicated by the arise of bands at 714 and 808 cm^{-1}.
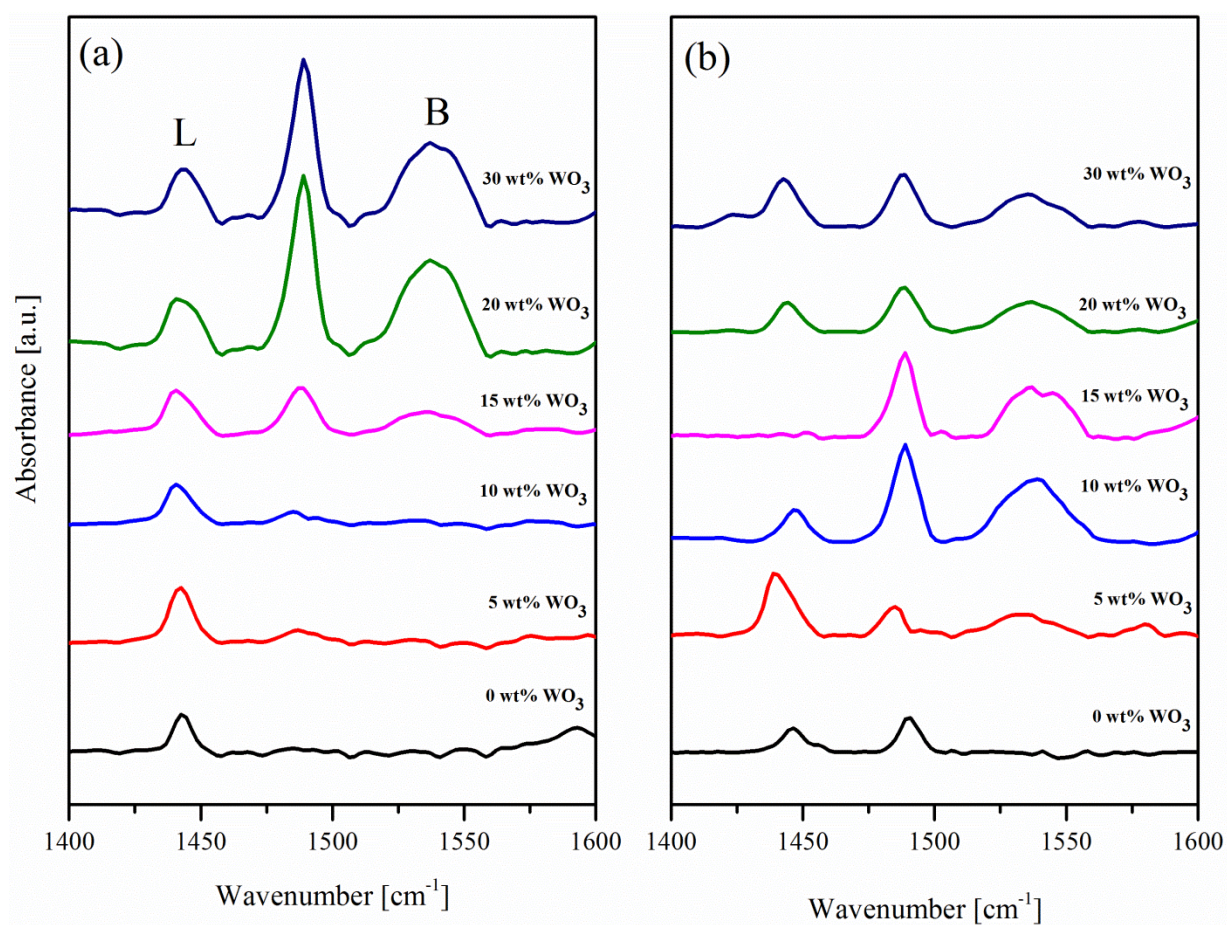

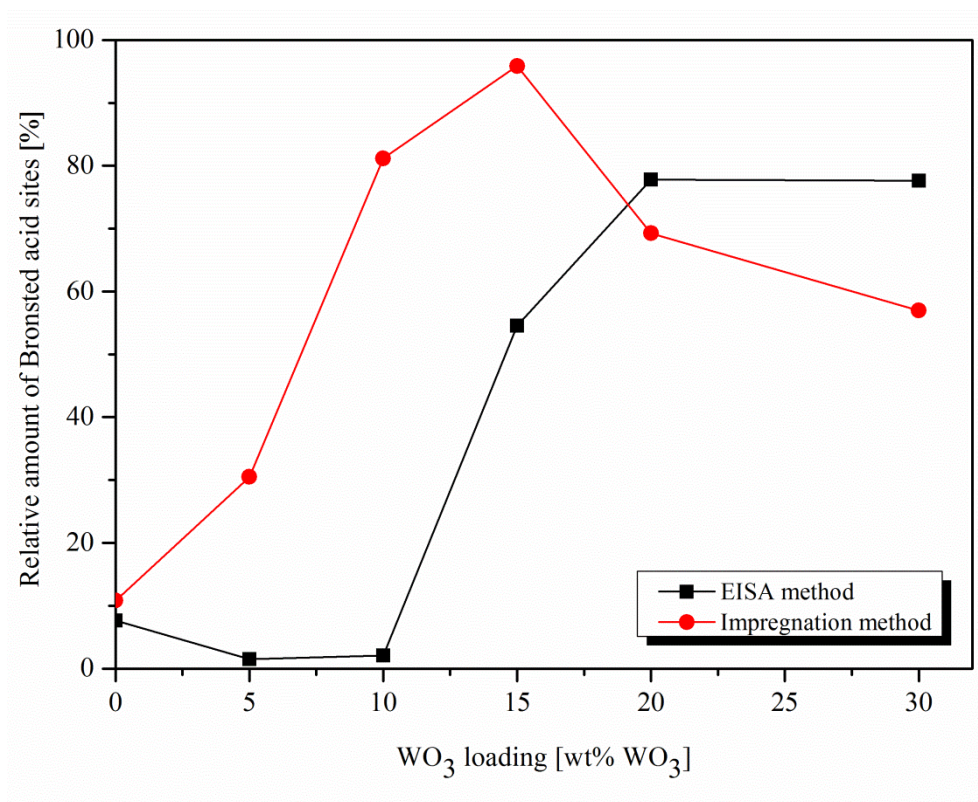**Figure 4-4. DRIFT spectra for pyridine adsorption of catalysts prepared via EISA (a) and impregnation (b)**

Figure 4-5. Semi-quantitative analysis of the relative concentration of Brönsted acid sites

4.2.6 Catalytic activity test
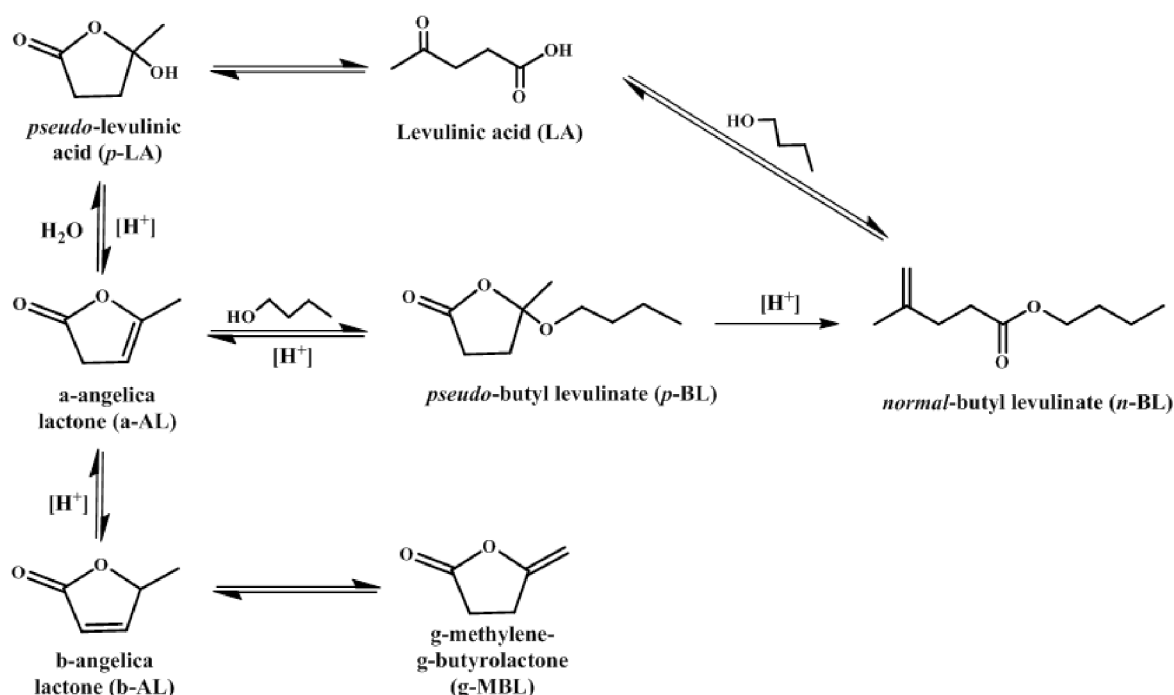
Scheme 4-1. Transformation of a-AL in the presence of acid catalysts

Esters of levulinic acid can be prepared from both a-AL and LA over solid acids. Al-Shaal et al recently proposed a reaction mechanism for the transformation of a-AL to *n*-BL through *p*-BL as an intermediate [134]. Their study emphasized the production of *p*-BL to be highly favorable because of a very low activation energy leading to a high yield of *p*-BL at a low temperature. Figure 4-6 shows the influence of WO_3 loading on a-AL conversion and ester selectivity for catalysts prepared via EISA and impregnation. In addition to esters, trace amount of γ-methylene-γ-butyrolactone (g-BL) and levulinic acid (LA) are also detected but are not included in the plots. G-BL is produced via a consecutive isomerization of a-AL in which b-AL is generated as an intermediate product Scheme 4-1. In the following, catalyst performance is monitored through a-AL conversion and *n*-BL yield. A blank test was firstly carried out providing no a-AL conversion which indicates the need of an efficient catalyst to initiate the reaction. The catalyst synthesized via EISA with $0 - 5$ wt.% WO_3 are inactive in the reaction. The activity can be improved after incorporation of 10 wt.% WO_3 allowing 23 % a-AL conversion and 5% *n*-BL yield. Substantial improvement in the activity can be obtained by the addition of 15 and 20 wt.% WO_3 leading to 91 and 99 % a-AL conversion together with

9 and 12 % *n*-BL selectivity, respectively. The activity remains comparable after increasing WO$_3$ concentration to 30 wt.%. A somewhat different trend occurs for catalysts prepared by impregnation. 15% a-AL conversion accompanied by 4% *n*-BL yield can be achieved with only 5 wt.% WO$_3$ content. Furthermore, a slightly higher WO$_3$ loading of 10 wt.% results in a drastic improvement of catalytic activity leading to 100% a-AL conversion and 34% *n*-BL yield. Increasing WO$_3$ loading further creates a maximum activity at 15 wt.% WO$_3$ resulting in 100% a-AL conversion with a *n*-BL selectivity of 43%, which subseqeuntly declines after incorporation of 20 and 30 wt.% WO$_3$ with 28 and 26% *n*-BL selectivity.

A number of catalyst property has been considered to study the factors influencing the activity. First of all, nearly no catalytic correlation can be inferred with the specific surface areas. Moreover, the activity is also independent to the acid strength and capacity. Therefore, a correlation based on the surface acid species determined by DRIFT pyridine spectroscopy is considered. The relative amount of Brönsted acid centers is highly decisive to control the activity and selectivity. For catalysts prepared via EISA, a low a-AL conversion at 0 – 10 wt.% WO$_3$ can be attributed to a poor concentration of Brönsted acid centers. Subsequently, the increase of a-AL conversion at WO$_3$ concentrations between 15 and 20 wt.% is in agreement with a rising concentration of Brönsted acid sites. The activity and selectivity remain constant between 20 and 30 wt.% which correspond to a comparable population of Brönsted acid population at this loading range. The same applies as well for impregnation. A fair increase of the Brönsted acid concentration from 0 to 5 wt.% results in 18% a-AL conversion. Thereafter, a considerable growth of Brönsted acid site concentration for 10 – 15 wt.% WO$_3$ is accompanied by an improving a-AL conversion and n-BL selectivity, respectively. Activity and selectivity establish a maximum at 15 wt.% WO$_3$ before they decline for 20 to 30 wt.% WO$_3$. Overall, these results confirm a correlation between Brönsted acid concentration and catalytic activity.

In comparison to EISA, catalysts prepared via impregnation exhibit significantly higher catalytic activity. For instance the maximum *n*-BL selectivity for impregnation can reach 43 % (15 wt.%, ρ_W = 7.5 W/nm^2) whereas materials prepared via EISA only facilitate a maximum *n*-BL selectivity of 12 % (20 wt.%, ρ_W = 7.7 W/nm^2). It is interesting that both catalysts exhibit maxima at similar ρ_W. According to Raman spectroscopy, this value is related to the first development of a sharp band at 808 and 714 cm^{-1} assigned to the

appearance of WO_3-NPs. It supports the fact that the incipient development WO_3-NPs positively effects catalytic activity by providing the highest concentration of Brönsted acid sites. The same observation was also obtained by Lopez et al [76], dos Santos et al [77] and our previous findings that the onset formation of WO_3-NPs could be responsible for the highest catalytic activity for the esterification.
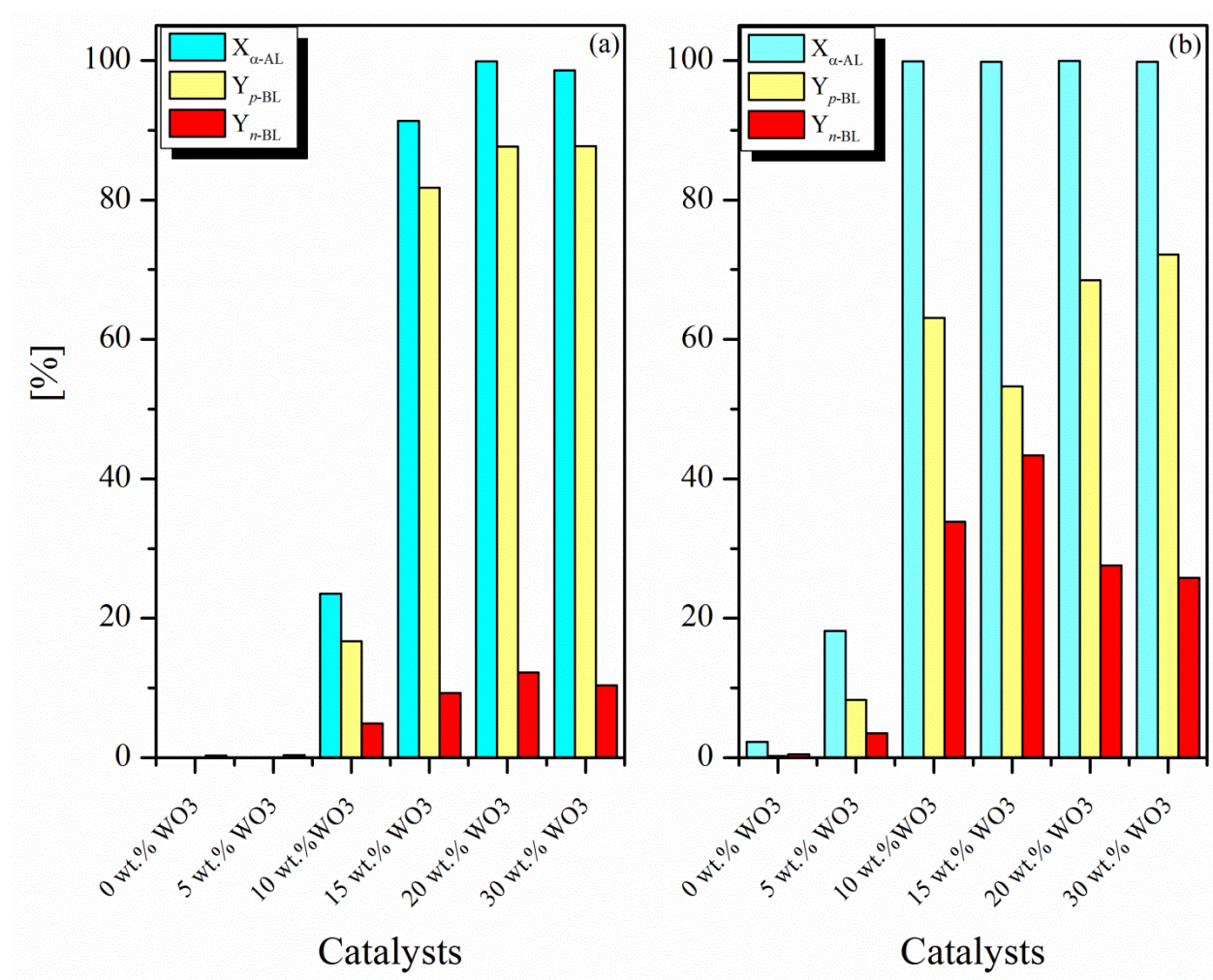
Figure 4-6. Catalytic activity of catalysts with different WO_3 loadings prepared by EISA (a) and impregnation (b). Reaction conditions: mole ratio of 1-BuOH/LA = 1 with 5 wt.% catalyst loading (respective to a-AL), at 75 °C for 6 h reaction under an agitation of 350 rpm

4.3 Summary

WO_x/ZrO_2 catalysts has been produced via EISA and wet impregnation. For both methods the WO_3 loading influences the resulting textural properties substantially including crystallinity and the surface state of the materials. XRD and Raman spectroscopy confirm

that a delayed transformation of tetragonal to monoclinic ZrO_2 as well as late formation of WO_3-NPs is promoted by employing EISA. For EISA, WO_3-NPs are initially developed at 7.7 W/nm^2, while a ρ_W as high as 4.3 W/nm^2 is able to promote the incipient formation of WO_3-NP in case of impregnation. The surface acidity varies with the amount of WO_3. DRIFT spectra suggests that the evolution of Brönsted acid sites occurs at 15 wt.% WO_3, which is 5 wt.% higher in WO_3 loading for impregnation. Applying these materials for catalysis, the highest activity occurs after doping 20 − 30 wt.% WO_3 for EISA and 15 wt.% WO_3 for impregnation. Overall impregnation enables higher catalytic activity than EISA. Irrespective of the preparation method, a similar ρ_W of 7.5 -7.7 W/nm^2 is confirmed to provide superior catalytic activity for this reaction. The values correspond to the first appearance of a sharp band at 804 and 714 cm^{-1} in Raman spectra associated to the formation of WO_3-NPs.

General Summary

In the first part of this work, the one pot synthesis by evaporation induced self-assembly (EISA) has been applied successfully to synthesize WO_x/mesoporous-ZrO_2 catalysts (WmZr). Two synthesis parameters were used namely WO_3 loading and calcination temperatures. As for WO_3 loading, WO_3 addition considerably influences the textural properties of the catalysts. XRD and Raman spectroscopy indicate that WO_3 incorporation facilitates preserving tetragonal ZrO_2. Raman spectra suggest particularly that the development of WO_3-NPs takes place at 20 wt.% (7.7 W/nm^2). NH_3-TPD confirms that WO_3 positively affects surface acidity. Different amounts of WO_3 also alter the relative ratio of Brönsted/Lewis acid sites. Generally applying higher temperatures negatively influences the textural properties of catalyst. Calcination at an extremely high temperature (900 °C) can partially transform tetragonal to monoclinic ZrO_2 with the intense formation of WO_3-NPs. While the number of acid sites decreases with calcination temperature, a maximum concentration of Brönsted acid sites occurs at 800 °C. Furthermore, WmZr is applied to initiate LA esterification suggesting a high dependency of catalytic activity on Brönsted acid site concentration. Maximum catalytic activity is enabled by 20 wt.% WmZr calcined at 800 °C (7.7 W/nm^2)

The second part elaborates more on the reaction mechanism of α-angelica lactone (a-AL) to levulinic acid esters (LAE). LAE can readily be produced employing a-AL as substrate. Two ester products are detectable namely pseudo- (*p*-BL) and normal-butyl levulinate (*n*-BL). The selectivity to *n*-BL can be enhanced at higher temperatures. LA is also formed during the reaction as a result of rehydration of a-AL in the presence of water. The development of LA negatively impacts on ester formation because the ester production will be limited by the equilibrium in LA esterification because the reaction will be reversible. Different types of acid catalysts were investigated demonstrating that Amberlyst 36 possesses superior catalytic activity. For catalysts with strong acid sites (HBEA zeolites and SO_4/ZrO_2), *n*-BL can be detected at different yields whereas weakly acidic catalysts result in high selectivity towards the formation of *p*-BL. Nevertheless, among the strong solid acids, no correlation between the number of acid sites and the catalytic activity could be established. A kinetic study at various temperatures reveals that 3 and 50 kJ/mol are

required to form *p*-BL and *n*-BL, respectively. It implies the consecutive transformation of *p*- to *n*-BL is the rate determining step.

Furthermore, structure-activity relations influencing the catalytic acticity in a-AL addition are elucidated in the third part. To facilitate the investigation, WO_x/ZrO_2 catalysts with different WO_3 loadings and synthesized via two different methods, EISA and wet impregnation, are applied for a-AL addition with 1-BuOH. For the two different methods, the WO_3 loadings influence the textural properties. Catalysts prepared via EISA have the ability to delay the transformation of tetragonal to monoclinic ZrO_2. Additionally, WO_3-NPs are formed at lower WO_3 loading (10 wt.%) for catalysts prepared via impregnation. NH_3-TPD confirms rising acid site concentration with an increasing WO_3 loading for both synthesis routes. The WO_3 loading influence the relative population of Brönsted acid centers in a different way. For EISA, the number of Brönsted acid sites increases up to 20 wt.% WO_3 loading. Higher WO_3 amounts of 30 wt.% do not significantly alter the Brönsted acid concentration. For impregnation, the increase of WO_3 concentration to 15 wt.% is followed by an increase of Brönsted acid site concentration followed by the decrease as the WO_3 content rises from 20 to 30 wt.%. Applying WZr catalysts in a-AL addition, a strong relationship between catalytic activity and WO_3 loading can be affirmed. It is noteworthy that the impregnation route provides higher catalytic activity compared to EISA.

REFERENCE

[1]   E.F. Gallei, M. Hesse, E. Schwab, Preparation of solid catalysts, in: Handbook of Heterogeneous Catalysis, Wiley-VCH Verlag GmbH, 2008: pp. 57 – 66.

[2]   R. Schlögl, Inorganic reactions: Ammonia Synthesis, in: Handbook of Heterogeneous Catalysis, Wiley-VCH Verlag GmbH, 2008: pp. 2501–2575.

[3]   B. Todic, L. Nowicki, N. Nikacevic, D.B. Bukur, Fischer-Tropsch synthesis product selectivity over an industrial iron-based catalyst: Effect of process conditions, Catal. Today. 261 (2016) 28–39.

[4]   H.M.T. Galvis, K.P. De Jong, Catalysts for Production of Lower Olefins from Synthesis Gas : A Review, ACS Catal. 3 (2013) 2130–2149.

[5]   V.M. Akhmedov, S.H. Al-Khowaiter, Recent Advances and Future Aspects in the Low-Temperature Conversion Of, Catal. Rev. Sci. Eng. 44 (2002) 455–498.

[6]   H. Deldari, Suitable catalysts for hydroisomerization of long-chain normal paraffins, Appl. Catal. A Gen. 293 (2005) 1–10.

[7]   Z.M. Liu, J.H. Li, S.I. Woo, Recent advances in the selective catalytic reduction of NO_x by hydrogen in the presence of oxygen, Energy Environ. Sci. 5 (2012) 8799–8814.

[8]   H. Hamada, M. Haneda, A review of selective catalytic reduction of nitrogen oxides with hydrogen and carbon monoxide, Appl. Catal. A Gen. 421-422 (2012) 1–13.

[9]   A. Galadima, O. Muraza, Catalytic upgrading of vegetable oils into jet fuels range hydrocarbons using heterogeneous catalysts: A review, J. Ind. Eng. Chem. 29 (2015) 12–23.

[10]   M. Besson, P. Gallezot, C. Pinel, Conversion of biomass into chemicals over metal catalysts, Chem. Rev. 114 (2014) 1827–1870.

[11]   G. Busca, Heterogeneous Catalytic Materials, Elsevier, 2014.

[12]   G. Busca, Acid catalysts in industrial hydrocarbon chemistry, Chem. Rev. 107 (2007) 5366–5410.

[13]   E.T.C. Vogt, B.M. Weckhuysen, Fluid catalytic cracking: recent developments on the grand old lady of zeolite catalysis, Chem. Soc. Rev. 44 (2015) 7342–7370.

[14]   F. Kollmer, H. Hausmann, W.F. Hoelderich, (NH4)2SiF6-modified ZSM-5 as catalysts for direct hydroxylation of benzene with N_2O. 2. A comparative study with ferrisilicalite and dealuminated and iron-exchanged ZSM-5, J. Catal. 227 (2004) 408–418.

[15]   K. Tanabe, Industrial application of solid acid–base catalysts, Appl. Catal. A Gen. 181 (1999) 399–434.

[16]   C.C. Holm, G.C. Bailey, Sulfate treated ZrO_2 gel catalyst, 3,032,599, 1962.

[17]   J. Oh, S. Dash, H. Lee, Selective conversion of glycerol to 1,3-propanediol using Pt-sulfated zirconia, Green Chem. 13 (2011) 2004.

[18]   R.S. Drago, N. Kob, Acidity and reactivity of sulfated zirconia and metal-doped sulfated zirconia, J. Phys. Chem. B. 101 (1997) 3360–3364.

[19]   I.I. Abu, D.D. Das, H.K. Mishra, A.K. Dalai, Studies on platinum-promoted sulfated zirconia alumina: Effects of pretreatment environment and carrier gas on n-butane isomerization and benzene alkylation activities, J. Colloid Interface Sci. 267 (2003)

382–390.

[20]   M. Hino, K. Arata, Synthesis of solid superacid of tungsten oxide supported on zirconia and its catalytic action for reactions of butane and pentane, J. Chem. Soc. Chem. Commun. (1988) 1259.

[21]   J. Livage, K. Doi, C. Mazieres, Nature and Thermal Evolution of Amorphous Hydrated Zirconium Oxide, J. Am. Ceram. Soc. 51 (1968) 349–353.

[22]   J. Livage, M. Henry, C. Sanchez, Sol-gel chemistry of transition metal oxides, Prog. Solid State Chem. 18 (1989) 259–341.

[23]   R.C. Garvie, Occurrence of Metastable Tetragonal Zirconia As a Crystallite Size Effect, J. Phys. Chem. 69 (1965) 1238–1243.

[24]   G.K. Chuah, S. Jaenicke, T.H. Xu, Acidity of high-surface-area zirconia prepared from different precipitants, Surf. Interface Anal. 28 (1999) 131–134.

[25]   P.F. Manicone, P. Rossi Iommetti, L. Raffaelli, An overview of zirconia ceramics: Basic properties and clinical applications, J. Dent. 35 (2007) 819–826.

[26]   L. Shi, K.C. Tin, N.B. Wong, Thermal stability of zirconia membranes, J. Mater. Sci. 34 (1999) 3367–3374.

[27]   R.L. Jones, F. Va, India stabilized ZrO_2 coating for composites, 1995US005418060A, 1995.

[28]   T. Van Gestel, H. Kruidhof, D.H.A. Blank, H.J.M. Bouwmeester, ZrO_2 and TiO_2 membranes for nanofiltration and pervaporation. Part 1. Preparation and characterization of a corrosion-resistant ZrO_2 nanofiltration membrane with a MWCO < 300, J. Memb. Sci. 284 (2006) 128–136.

[29]   D. Panthi, A. Tsutsumi, Micro-tubular solid oxide fuel cell based on a porous yttria-stabilized zirconia support., Sci. Rep. 4 (2014) 5754.

[30]   K. Pokrovski, K.T. Jung, A.T. Bell, Investigation of CO and CO_2 adsorption on tetragonal and monoclinic zirconia, Langmuir. 17 (2001) 4297–4303.

[31]   K.T. Jung, Y.G. Shul, A.T. Bell, The preparation and surface characterization of zirconia polymorphs, Korean J. Chem. Eng. 18 (2001) 992–999.

[32]   E. Rodriguez-Castellon, A. Jimenez-Lopez, P. Maireles-Torres, D.J. Jones, J. Roziere, M. Trombetta, et al., Textural and structural properties and surface acidity characterization of mesoporous silica-zirconia molecular sieves, J. Solid State Chem. 175 (2003) 159–169.

[33]   T. Yamaguchi, H. Sasaki, K. Tanabe, High selectivities of zirconium oxide catalyst for isomerization of 1-butene and dehydration of sec-butanol, Chem. Lett. 2 (1973) 1017–1018.

[34]   K. Tanabe, Surface and catalytic properties of ZrO_2, Mater. Chem. Phys. 13 (1985) 347–364.

[35]   Y. NAKANO, Surface properties of zirconium oxide and its catalytic activity for isomerization of 1-butene, J. Catal. 57 (1979) 1–10.

[36]   A. Satoh, H. Hattori, K. Tanabe, Selective formation of 1-butene in elimination of ammonia from 2-butanamine catalysed by ZrO_2, Chem. Lett. 12 (1983) 497–498.

[37] S. Letichevsky, P.C. Zonetti, P.P.P. Reis, J. Celnik, C.R.K. Rabello, A.B. Gaspar, et al., The role of m-ZrO2 in the selective oxidation of ethanol to acetic acid employing PdO/m-ZrO$_2$, J. Mol. Catal. A Chem. 410 (2015) 177–183.

[38] G.-Y. Yang, Y.-H. Ke, H.-F. Ren, C.-L. Liu, R.-Z. Yang, W.-S. Dong, The conversion of glycerol to lactic acid catalyzed by ZrO$_2$-supported CuO catalysts, Chem. Eng. J. 283 (2016) 759–767.

[39] F. Menegazzo, M. Signoretto, D. Marchese, F. Pinna, M. Manzoli, Structure-activity relationships of Au/ZrO$_2$ catalysts for 5-hydroxymethylfurfural oxidative esterification: Effects of zirconia sulphation on gold dispersion, position and shape, J. Catal. 326 (2015) 1–8.

[40] S. Foraita, J.L. Fulton, Z.A. Chase, A. Vjunov, P. Xu, E. Barath, et al., Impact of the oxygen defects and the hydrogen concentration on the surface of tetragonal and monoclinic ZrO2 on the reduction rates of stearic acid on Ni/ZrO$_2$, Chemistry. 21 (2015) 2423–2434.

[41] B.M. Reddy, M.K. Patil, Organic Syntheses and Transformations Catalyzed by Sulfated Zirconia, Chem. Rev. 109 (2009) 2185–2208.

[42] M.A. Al-Daous, A. Stein, Preparation and catalytic evaluation of macroporous crystalline sulfated zirconium dioxide templated with colloidal crystals, Chem. Mater. 15 (2003) 2638–2645.

[43] K. Shimizu, N. Kounami, H. Wada, T. Shishido, H. Hattori, Isomerization of *n*-butane by sulfated zirconia: the effect of calcination temperature and characterization of its surface acidity, Catal. Letters. 54 (1998) 153–158.

[44] D. Tichit, D. El Alami, F. Figueras, Influence of the Preparation and of the Activation Treatments on the Catalytic activity of mechanical mixtures of sulfated zirconia and Pt/Al$_2$O$_3$, J. Catal. 27 (1996) 18–27.

[45] D. Tichit, B. Coq, H. Armendariz, F. Figueras, One-step sol-gel synthesis of sulfated-zirconia catalysts, Catal. Letters. 38 (1996) 109–113.

[46] M. Signoretto, F. Pinna, G. Strukul, P. Chies, G. Cerrato, S. Di Ciero, et al., Platinum-Promoted and Unpromoted Sulfated Zirconia Catalysts Prepared by a One-Step Aerogel Procedure, J. Catal. 167 (1997) 522–532.

[47] S.K. Das, M.K. Bhunia, A.K. Sinha, A. Bhaumik, Self-Assembled Mesoporous Zirconia and Sulfated Zirconia Nanoparticles Synthesized by Triblock Copolymer as Template Self-Assembled Mesoporous Zirconia and Sulfated Zirconia Nanoparticles Synthesized by Triblock Copolymer as Template, J. Phys. Chem. C. 113 (2009) 8918–8923.

[48] Y. Sun, L. Yuan, W. Wang, C. Chen, F. Xiao, Mesostructured sulfated zirconia with high catalytic activity in n -butane isomerization, Catal. Letters. 87 (2010) 57–61.

[49] X. Yang, F.C. Jentoft, R.E. Jentoft, F. Girgsdies, T. Ressler, Sulfated zirconia with ordered mesopores as an active catalyst for n -butane isomerization, Catal. Letters. 81 (2002) 25–31.

[50] H. Pu, L. Zhang, D. Du, C. Han, H. Li, J. Li, et al., One-step synthesis of mesoporous sulfated zirconia nanoparticles with anionic template, Korean J. Chem. Eng. 29 (2012)

1285–1288.

[51] A. Khodakov, J. Yang, S. Su, E. Iglesia, A.T. Bell, Structure and properties of vanadium oxide-zirconia catalysts for propane oxidative dehydrogenation, J. Catal. 177 (1998) 343–351.

[52] D.A. Ward, E. Ko, One step synthesis and characterization of Zr-sulfate aerogels as solid superacids, J. Catal. 150 (1994) 18–33.

[53] A. Sayari, A. Dicko, The state of Pt in platina on sulfated zirconia super acid catalysts, J. Catal. 145 (1994) 561–564.

[54] K. Ebitani, J. Tsuji, H. Hattori, H. Kita, Dynamic modification of surface acid properties with hydrogen molecule for zirconium oxide promoted by platinum and sulfate ions, J. Catal. 135 (1992) 609–617.

[55] S.T. Wong, C.C. Hwang, C.Y. Mou, Tungstated zirconia catalyzed bromination of phenol red under nearly neutral solution, Appl. Catal. B Environ. 63 (2006) 1–8.

[56] M. Scheithauer, R.K. Grasselli, H. Knözinger, Genesis and Structure of WO_x/ZrO_2 Solid Acid Catalysts, Langmuir. 14 (1998) 3019–3029.

[57] M. Scheithauer, T.K. Cheung, R.E. Jentoft, R.K. Grasselli, B.C. Gates, H. Knozinger, Characterization of WO_x/ZrO_2 by vibrational spectroscopy and n-pentane isomerization catalysis, J. Catal. 180 (1998) 1–13.

[58] R.A. Boyse, E.I. Ko, Crystallization Behavior of Tungstate on Zirconia and Its Relationship to Acidic Properties, J. Catal. 179 (1998) 100–110.

[59] D.G. Barton, M. Shtein, R.D. Wilson, S.L. Soled, E. Iglesia, Structure and Electronic Properties of Solid Acids Based on Tungsten Oxide Nanostructures, J. Phys. Chem. B. 103 (1999) 630–640.

[60] E.I. Ross-Medgaarden, W. V. Knowles, T. Kim, M.S. Wong, W. Zhou, C.J. Kiely, et al., New insights into the nature of the acidic catalytic active sites present in ZrO_2-supported tungsten oxide catalysts, J. Catal. 256 (2008) 108–125.

[61] D. Masure, P. Chaquin, C. Louis, M. Che, M. Fournier, Polyoxometallates as Models for Oxide Catalysts, J. Catal. 119 (1989) 415–425.

[62] D.G. Barton, S.L. Soled, G.D. Meitzner, G.A. Fuentes, E. Iglesia, Structural and Catalytic Characterization of Solid Acids Based on Zirconia Modified by Tungsten Oxide, J. Catal. 181 (1999) 57–72.

[63] A. Martinez, G. Prieto, M.A. Arribas, P. Concepcion, J.F. Sanchez-Royo, Influence of the preparative route on the properties of WO_x-ZrO_2 catalysts: A detailed structural, spectroscopic, and catalytic study, J. Catal. 248 (2007) 288–302.

[64] I. V. Kozhevnikov, A. Sinnema, H. van Bekkum, Proton sites in Keggin heteropoly acids from 17O NMR, Catal. Letters. 34 (1995) 213–221.

[65] Y. Song, J. Zhang, X. Zhou, J.A. Wang, L. Xu, G. Yu, WO3 microcrystallites: One of the crucial factors controlling the isomerization activity of Pt/WO_3-ZrO_2, Catal. Today. 166 (2011) 67–72.

[66] M. Busto, J.M. Grau, J.H. Sepulveda, O.M. Tsendra, C.R. Vera, Hydrocracking of Long Para ffi ns over Pt–Pd/WO_3–ZrO_2 in the Presence of Sulfur and Aromatic Impurities,

Energy and Fuels. 27 (2013) 6962–6972.

[67] M. Busto, L.A. Dosso, C.R. Vera, J.M. Grau, Composite catalysts of Pt/SO4^{2-}-ZrO$_2$ and Pt/WO$_3$-ZrO$_2$ for producing high octane isomerizate by isomerization-cracking of long paraffins, Fuel Process. Technol. 104 (2012) 128–135.

[68] D.C. Calabro, J.C. Vartuli, J.G. Santiesteban, The characterization of tungsten-oxide-modified zirconia supports for dual functional catalysis, Top. Catal. 18 (2002) 231–242.

[69] Y. Liu, Y. Guan, C. Li, J. Lian, G.J. Gan, E.C. Lim, et al., Effect of ZnO additives and acid treatment on catalytic performance of Pt/WO$_3$/ZrO$_2$ for n-C7 hydroisomerization, J. Catal. 244 (2006) 17–23.

[70] D.G. Barton, S.L. Soled, E. Iglesia, Solid acid catalysts based on supported tungsten oxides, Top. Catal. 6 (1998) 87–99.

[71] C.D. Baertsch, K.T. Komala, Y.-H. Chua, E. Iglesia, Genesis of Brønsted Acid Sites during Dehydration of 2-Butanol on Tungsten Oxide Catalysts, J. Catal. 205 (2002) 44–57.

[72] T.N. Vu, J. Van Gestel, J.P. Gilson, C. Collet, J.P. Dath, J.C. Duchet, Platinum-tungstated zirconia isomerization catalysts: Part II. Effect of platinum and tungsten loading on the mechanism of isomerization of n-hexane: A kinetic study, J. Catal. 231 (2005) 468–479.

[73] K. Song, H. Zhang, Y. Zhang, Y. Tang, K. Tang, Preparation and characterization of WO$_x$/ZrO$_2$ nanosized catalysts with high WOx dispersion threshold and acidity, J. Catal. 299 (2013) 119–128.

[74] N.R. Shiju, M. Anilkumar, W.F. Hoelderich, D.R. Brown, Tungstated zirconia catalysts for liquid-phase Beckmann rearrangement of cyclohexanone oxime: Structure-activity relationship, J. Phys. Chem. C. 113 (2009) 7735–7742.

[75] S. Zhu, Y. Zhu, X. Gao, T. Mo, Y. Zhu, Y. Li, Production of bioadditives from glycerol esterification over zirconia supported heteropolyacids, Bioresour. Technol. 130 (2013) 45–51.

[76] D.E. López, K. Suwannakarn, D.A. Bruce, J.G. Goodwin, Esterification and transesterification on tungstated zirconia: Effect of calcination temperature, J. Catal. 247 (2007) 43–50.

[77] V.C. dos Santos, K. Wilson, A.F. Lee, S. Nakagaki, Physicochemical properties of WO$_x$/ZrO$_2$ catalysts for palmitic acid esterification, Appl. Catal. B Environ. 162 (2015) 75–84.

[78] W. Zhou, E.I. Ross-Medgaarden, W. V Knowles, M.S. Wong, I.E. Wachs, C.J. Kiely, Identification of active Zr–WOx clusters on a ZrO$_2$ support for solid acid catalysts, Nat. Chem. 1 (2009) 722–728.

[79] C. Liu, J. Sun, H.M. Brown, O.G. Marin-Flores, T. Bays, A.M. Karim, et al., Aqueous Phase Hydrodeoxygenation of Polyols over Pd/WO$_3$-ZrO$_2$: Role of Pd-WO$_3$ Interaction and Hydrodeoxygenation Pathway, Catal. Today. 1 (2015) 1–11.

[80] L.-Z. Qin, M.-J. Song, C.-L. Chen, Aqueous-phase deoxygenation of glycerol to 1,3-propanediol over Pt/WO$_3$/ZrO$_2$ catalysts in a fixed-bed reactor, Green Chem. 12 (2010) 1466–1472.

[81]   T. Kurosaka, H. Maruyama, I. Naribayashi, Y. Sasaki, Production of 1,3-propanediol by hydrogenolysis of glycerol catalyzed by Pt/WO$_3$/ZrO$_2$, Catal. Commun. 9 (2008) 1360–1363.

[82]   S. Zhu, X. Gao, Y. Zhu, J. Cui, H. Zheng, Y. Li, SiO2 promoted Pt/WO$_x$/ZrO$_2$ catalysts for the selective hydrogenolysis of glycerol to 1,3-propanediol, Appl. Catal. B Environ. 158-159 (2014) 391–399.

[83]   P. Wongmaneenil, B. Jongsomjit, P. Praserthdam, Solvent effect on synthesis of zirconia support for tungstated zirconia catalysts, J. Ind. Eng. Chem. 16 (2010) 327–333.

[84]   S. Lecarpentier, J. van Gestel, K. Thomas, J.P. Gilson, M. Houalla, Study of Ir/WO$_3$/ZrO$_2$-SiO$_2$ ring-opening catalysts: Part II. Reaction network, kinetic studies and structure-activity correlation, J. Catal. 254 (2008) 49–63.

[85]   C. Hahn, M. Endisch, F.J.P. Schott, S. Kureti, Kinetic modelling of the NOx reduction by H2 on Pt/WO$_3$/ZrO$_2$ catalyst in excess of O$_2$, Appl. Catal. B Environ. 168-169 (2015) 429–440.

[86]   G.W. Huber, S. Iborra, A. Corma, Synthesis of transportation fuels from biomass: Chemistry, catalysts, and engineering, Chem. Rev. 106 (2006) 4044–4098.

[87]   J.N. Chheda, G.W. Huber, J.A. Dumesic, Liquid-phase catalytic processing of biomass-derived oxygenated hydrocarbons to fuels and chemicals, Angew. Chemie - Int. Ed. 46 (2007) 7164–7183.

[88]   C.E. Wyman, B.E. Dale, R.T. Elander, M. Holtzapple, M.R. Ladisch, Y.Y. Lee, Coordinated development of leading biomass pretreatment technologies, Bioresour. Technol. 96 (2005) 1959–1966.

[89]   C.E. Wyman, B.E. Dale, R.T. Elander, M. Holtzapple, M.R. Ladisch, Y.Y. Lee, Comparative sugar recovery data from laboratory scale application of leading pretreatment technologies to corn stover, Bioresour. Technol. 96 (2005) 2026–2032.

[90]   D.W. Rackemann, W.O. Doherty, The conversion of lignocellulosics to levulinic acid, Biofuels, Bioprod. Biorefining. 5 (2011) 198–214.

[91]   D.J. Hayes, J. Ross, M.H.B. Hayes, S. Fitzpatrick, The Biofine process: production of levulinic acid, furfural and formic acid from lignocellulosic feedstocks, in: Biorefineries-Industrial Process. Prod., Wiley-VCH Verlag GmbH, 2005: pp. 139–164.

[92]   M.M. Bomgardner, Interest In Biobased Levulinic Acid Grows, Chem. Eng. News. (2015). http://cen.acs.org/articles/93/web/2015/03/Interest-Biobased-Levulinic-Acid-Grows.html.

[93]   K. Laird, GFBiochemicals achieves commercial scale production of levulinic acid, Plast. Today. (2015). http://www.plasticstoday.com/gfbiochemicals-achieves-commercial-scale-production-levulinic-acid/80608969822562.

[94]   A. Demolis, N. Essayem, F. Rataboul, Synthesis and applications of alkyl levulinates, ACS Sustain. Chem. Eng. 2 (2014) 1338–1352.

[95]   N. Bayarri Ferrer, Degreasing compositions derived from levulinic acid (a compound obtainable from biomass) and process for degreasing metal surfaces, EP2540871A1,

2013.

[96] R.H. Clark, A.P. Groves, C. Morley, J. Smith, FUEL COMPOSITIONS, US2004/0128905A1, 2004.

[97] L. Manzer, Preparation of levulinic acid esters from alpha-angelica lactone and alcohols, US2006/0063948A1, 2006.

[98] E. Christensen, A. Williams, S. Paul, S. Burton, R.L. McCormick, Properties and performance of levulinate esters as diesel blend components, Energy and Fuels. 25 (2011) 5422–5428.

[99] B.D. Mullen, V. Badarinarayana, E.S. Hall, M.J. Tjossas, C. Leibig, Stabilized levulinic ester ketals, US2013/0087073A1, 2013.

[100] D.J. Yontz, G. Valley, Fragrant Formulations, Methods of manufacture thereof and Articles Comprising the Same, CA2792018A1, 2012.

[101] D.J. Yontz, L.R. Rieth, N. Morante, I. Palefsky, Personal care formulations containing alkyl-ketal esters and method of manufacture, US2015/0064124A1, 2015.

[102] D.R. Fernandes, A.S. Rocha, E.F. Mai, C.J.A. Mota, V. Teixeira Da Silva, Levulinic acid esterification with ethanol to ethyl levulinate production over solid acid catalysts, Appl. Catal. A Gen. 425-426 (2012) 199–204.

[103] Y. Kuwahara, W. Kaburagi, K. Nemoto, T. Fujitani, Esterification of levulinic acid with ethanol over sulfated Si-doped ZrO_2 solid acid catalyst: Study of the structure-activity relationships, Appl. Catal. A Gen. 476 (2014) 186–196.

[104] K.C. Maheria, J. Kozinski, A. Dalai, Esterification of levulinic acid to n-butyl levulinate over various acidic zeolites, Catal. Letters. 143 (2013) 1220–1225.

[105] K.Y. Nandiwale, S.K. Yadava, V. V. Bokade, Production of octyl levulinate biolubricant over modified H-ZSM-5: Optimization by response surface methodology, J. Energy Chem. 23 (2014) 535–541.

[106] S. Dharne, V. V. Bokade, Esterification of levulinic acid to n-butyl levulinate over heteropolyacid supported on acid-treated clay, J. Nat. Gas Chem. 20 (2011) 18–24.

[107] F. Su, L. Ma, D. Song, X. Zhang, Y. Guo, Design of a highly ordered mesoporous $H_3PW_{12}O_{40}$/ZrO_2-Si(Ph)Si hybrid catalyst for methyl levulinate synthesis, Green Chem. 15 (2013) 885–890.

[108] K.Y. Nandiwale, S.K. Sonar, P.S. Niphadkar, P.N. Joshi, S.S. Deshpande, V.S. Patil, et al., Catalytic upgrading of renewable levulinic acid to ethyl levulinate biodiesel using dodecatungstophosphoric acid supported on desilicated H-ZSM-5 as catalyst, Appl. Catal. A Gen. 460-461 (2013) 90–98.

[109] K. Yan, G. Wu, J. Wen, A. Chen, One-step synthesis of mesoporous H4SiW12O40-SiO2 catalysts for the production of methyl and ethyl levulinate biodiesel, Catal. Commun. 34 (2013) 58–63.

[110] F.G. Cirujano, A. Corma, F.X. Llabr??s i Xamena, Conversion of levulinic acid into chemicals: Synthesis of biomass derived levulinate esters over Zr-containing MOFs, Chem. Eng. Sci. 124 (2015) 52–60.

[111] F.D. Pileidis, M.-M. Titirici, Levulinic Acid Biorefineries: New Challenges for Efficient

Utilization of Biomass, ChemSusChem. 9 (2016) n/a–n/a. doi:10.1002/cssc.201501405.

[112] C.R. Patil, P.S. Niphadkar, V. V. Bokade, P.N. Joshi, Esterification of levulinic acid to ethyl levulinate over bimodal micro-mesoporous H/BEA zeolite derivatives, Catal. Commun. 43 (2014) 188–191.

[113] J.A. Melero, G. Morales, J. Iglesias, M. Paniagua, B. Hernandez, S. Penedo, Efficient conversion of levulinic acid into alkyl levulinates catalyzed by sulfonic mesostructured silicas, Appl. Catal. A Gen. 466 (2013) 116–122.

[114] B.L. Oliveira, V. Teixeira Da Silva, Sulfonated carbon nanotubes as catalysts for the conversion of levulinic acid into ethyl levulinate, Catal. Today. 234 (2014) 257–263.

[115] F. Su, Q. Wu, D. Song, X. Zhang, M. Wang, Y. Guo, Pore morphology-controlled preparation of ZrO_2-based hybrid catalysts functionalized by both organosilica moieties and Keggin-type heteropoly acid for the synthesis of levulinate esters, J. Mater. Chem. A. 1 (2013) 13209–13221.

[116] G. Pasquale, P. Vázquez, G. Romanelli, G. Baronetti, Catalytic upgrading of levulinic acid to ethyl levulinate using reusable silica-included Wells-Dawson heteropolyacid as catalyst, Catal. Commun. 18 (2012) 115–120.

[117] E. Siva Sankar, V. Mohan, M. Suresh, G. Saidulu, B. David Raju, K.S. Rama Rao, Vapor phase esterification of levulinic acid over ZrO_2/SBA-15 catalyst, Catal. Commun. 75 (2016) 1–5.

[118] D.E. López, J.G. Goodwin, D.A. Bruce, S. Furuta, Esterification and transesterification using modified-zirconia catalysts, Appl. Catal. A Gen. 339 (2008) 76–83.

[119] K. Ngaosuwan, B. Jongsomjit, P. Praserthdam, The role of zirconia surface on catalytic activity of tungstated zirconia via two-phase esterification of acetic acid and 1-heptanol, Catal. Letters. 136 (2010) 134–140.

[120] X. Hu, Z. Zhou, D. Sun, Y. Wang, Z. Zhang, Esterification of fatty acid by zirconic catalysts, Catal. Letters. 133 (2009) 90–96.

[121] Y.M. Park, S.H. Chung, H.J. Eom, J.S. Lee, K.Y. Lee, Tungsten oxide zirconia as solid superacid catalyst for esterification of waste acid oil (dark oil), Bioresour. Technol. 101 (2010) 6589–6593.

[122] C. Zhang, T. Liu, H.J. Wang, F. Wang, X.Y. Pan, Synthesis of acetyl salicylic acid over WO3/ZrO2 solid superacid catalyst, Chem. Eng. J. 174 (2011) 236–241.

[123] I. Jimenez-Morales, J. Santamaria-Gonzalez, P. Maireles-Torres, A. Jimenez-Lopez, Zirconium doped MCM-41 supported WO3 solid acid catalysts for the esterification of oleic acid with methanol, Appl. Catal. A Gen. 379 (2010) 61–68.

[124] S.M. Morris, P.F. Fulvio, M. Jaroniec, Ordered mesoporous alumina-supported metal oxides, J. Am. Chem. Soc. 130 (2008) 15210–15216.

[125] X. Chen, T. Yu, X. Fan, H. Zhang, Z. Li, J. Ye, et al., Enhanced activity of mesoporous Nb_2O_5 for photocatalytic hydrogen production, Appl. Surf. Sci. 253 (2007) 8500–8506.

[126] G.J. de Soler-Illia, A. Louis, C. Sanchez, Synthesis and Characterization of Mesostructured Titania-Based Materials through Evaporation-Induced Self-Assembly, Chem. Mater. 14 (2002) 750–759.

[127] Z. Miao, H. Song, H. Zhao, L. Xu, L. Chou, One-pot synthesis of mesoporous ZrPW solid acid catalyst for liquid phase benzylation of anisole, Catal. Sci. Technol. 4 (2014) 838.

[128] I.M. Hung, D.T. Hung, K.Z. Fung, M.H. Hon, Synthesis and characterization of highly ordered mesoporous YSZ by tri-block copolymer, J. Porous Mater. 13 (2006) 225–230.

[129] L. Xu, H. Song, L. Chou, Carbon dioxide reforming of methane over ordered mesoporous $NiO-MgO-Al_2O_3$ composite oxides, Appl. Catal. B Environ. 108-109 (2011) 177–190.

[130] C.C. Hwang, X.R. Chen, S.T. Wong, C.L. Chen, C.Y. Mou, Enhanced catalytic activity for butane isomerization with alumina-promoted tungstated mesoporous zirconia, Appl. Catal. A Gen. 323 (2007) 9–17.

[131] S. Li, H. Zhou, C. Jin, N. Feng, F. Liu, F. Deng, et al., Formation of Subnanometer Zr-WOx Clusters within Mesoporous W–Zr Mixed Oxides as Strong Solid Acid Catalysts for Friedel–Crafts Alkylation, J. Phys. Chem. C. 118 (2014) 6283.

[132] C.S. Triantafillidis, A.G. Vlessidis, N.P. Evmiridis, Dealuminated H–Y Zeolites: Influence of the Degree and the Type of Dealumination Method on the Structural and Acidic Characteristics of H–Y Zeolites, Ind. Eng. Chem. Res. 39 (2000) 307–319.

[133] K.A. Michalow-Mauke, Y. Lu, K. Kowalski, T. Graule, M. Nachtegaal, O. Kröcher, et al., Flame-Made WO_3/CeO_x-TiO $_2$ Catalysts for Selective Catalytic Reduction of NO_x by NH_3, ACS Catal. 5 (2015) 5657–5672.

[134] M.G. Al-Shaal, W. Ciptonugroho, F.J. Holzhäuser, J.B. Mensah, P.J.C. Hausoul, R. Palkovits, Catalytic upgrading of α-angelica lactone to levulinic acid esters under mild conditions over heterogeneous catalysts, Catal. Sci. Technol. 5 (2015) 5168–5173.

[135] R. Kourieh, V. Rakic, S. Bennici, A. Auroux, Relation between surface acidity and reactivity in fructose conversion into 5-HMF using tungstated zirconia catalysts, Catal. Commun. 30 (2013) 5–13.

[136] J. Weitkamp, Zeolites and catalysis, Solid State Ionics. 131 (2000) 175–188.

[137] M.G. Al-Shaal, P.J.C. Hausoul, R. Palkovits, Efficient, solvent-free hydrogenation of α-angelica lactone catalysed by Ru/C at atmospheric pressure and room temperature., Chem. Commun. 50 (2014) 10206–10209.

[138] R. Cao, J. Xin, Z. Zhang, Z. Liu, X. Lu, B. Ren, et al., Efficient Conversion of \upalpha-Angelica Lactone into \upgamma-Valerolactone with Ionic Liquids at Room Temperature, ACS Sustain. Chem. Eng. 2 (2014) 902–909.

[139] O.A. Abdelrahman, A. Heyden, J.Q. Bond, Analysis of Kinetics and Reaction Pathways in the Aqueous-Phase Hydrogenation of Levulinic Acid To Form gamma-Valerolactone over Ru/C, ACS Catal. 4 (2014) 1171–1181.

[140] M. Mascal, S. Dutta, I. Gandarias, Hydrodeoxygenation of the angelica lactone dimer, a cellulose-based feedstock: Simple, high-yield synthesis of branched C7-C10 gasoline-like hydrocarbons, Angew. Chemie - Int. Ed. 53 (2014) 1854–1857.

[141] D.P. Langlois, H. Wolff, 2624 David P. Langlois, Pseudo esters of levulinic acid, J. Am. Chem. Soc. 70 (1944) 2624–2626.

[142] E.I. Ross-medgaarden, I.E. Wachs, Structural Determination of Bulk and Surface

Tungsten Oxides with UV - vis Diffuse Reflectance Spectroscopy and Raman
Spectroscopy, J. Phys. Chem. C. 111 (2007) 15089–15099.

Appendix 1 Experimental

Used chemicals

Compounds	Supplier	Purity
F127	Sigma-aldrich	-
Citric acid	ROTH	>99.5%
Ethanol	Chemsolute	99.5 %
Hydrochloric acid	Chemsolute	35-37%
Zirconium(IV) butoxide	Sigma Aldrich	80 wt.%
Zirconium hydroxide	Sigma Aldrich	97%
Tungsten(VI) chloride	ABCR	99%
Ammonium meta-tungstate	Sigma Aldrich	99%
Levulinic acid	Sigma Aldrich	>98%
α-angelica lactone	Sigma Aldrich	98%
1-butanol	Sigma Aldrich	>99.7%
1-octanol	Sigma Aldrich	99.9%
1,4-dioxane	Sigma Aldrich	99.8%
Diethylene glycol diethyl ether	Sigma Aldrich	>99.5%
γ-methylene-γ-butyrolactone	TCI Chemicals	98%
normal-butyl levulinate	Sigma Aldrich	98%
normal-ethyl levulinate	Sigma Aldrich	99%
15 wt%. WO_3/ZrO_2	Saint Gobain	-
SO_4/ZrO_2	Saint Gobain	-
HBEA-25	Süd Chemie	-
HBEA-150	Süd Chemie	-
HMFI-40	Süd Chemie	-
Amberlyst-15	The Dow Chemicals	-
Amberlyst-36	The Dow Chemicals	-
γ-Al2O3	Sasol	-
Monoclinic ZrO_2	Saint Gobain	-

Catalyst preparation via evaporation induced self-assembly method

$WO_x/mesoZrO_2$ (WmZr) was prepared by firstly dissolving 2.43 g template together with 1.53 g citric acid and 73 ml ethanol in a polypropylene bottle under vigorous stirring until a clear mixture was achieved. This procedure took normally 3 h for complete dissolution of the template. Subsequently, 3.65 g HCl (35%) was added into the mixture after which a corresponding amount of WCl6 was introduced. It is noticeable that WCl_6 was firstly weighed under protected atmosphere. After a clear yellowish solution was obtained, 5.84 g zirconium (IV) butoxide was gently added under strong agitation. The agitation was then carried out for 3 hours until a milky homogeneous sol was observed. Next, the sol was poured into two Petri-dishes at the same height to allow solvent evaporation for 48 h at room temperature. The partially dried samples were then stored overnight in the oven for complete drying and solidification. The dried solid was peeled off from the Petri-dish before being calcined at different calcination temperatures for 5 h with a slow ramping rate of 1 K/min. The final catalyst was then denoted as xWmZr-T where x and T stands for WO_3 loading and calcination temperatures, respectively. For instance 5WmZr-700 means that the catalyst is loaded with 5 wt.% WO_3 and subjected to 700 °C for the calcination. As a note, tungsten loading (x) is defined as nominal mass percentage of WO_3 per 1 g of ZrO_2 support.

Catalyst preparation via impregnation method

The impregnating solution was prepared by dissolving the respective amount of ammo-nium meta-tungstate in 5 ml double distilled water. Into this solution, 2 g $Zr(OH)_4$ was soaked and stirred for 3 h at room temperature. Furthermore, the mixture was dried in the oven at 100 °C overnight before being calcined at 800 °C for 5 h under 5 K/min ramping rate.

Isothermal N$_2$ physisorption

Isothermal physisorption was performed on Quadrasorb SI automated surface area and pore size analyser. Before measuring, the sample was degassed at 120 °C overnight to liberate the catalyst surface from impurities. N2 adsorption was carried out at -196 °C.

Catalyst surface areas were calculated applying multi-point BET in the partial pressure range from 0.05 – 0.3. The pore size distribution (PSD) was determined from the desorption branch using a non-linear DFT method (NLDFT).

X-ray diffraction (XRD)

X-ray reflection of the samples was collected on Siemens D-5000 equipped with Cu-Kα light source.

Laser Fourier Transform Raman spectroscopy (Laser FT Raman spectroscopy)

FT-Raman spectra were collected by a Bruker RFS100/S-instrument with 4 cm^{-1} spectra resolution. Nd:YAG (with 1064 nm wavelength) was used as a laser generator. Prior to measurement, the catalyst powder was pressed into an aluminum pin. During the measurement, the detector was cooled down by liquid N_2.

NH$_3$-temperature program desorption (NH$_3$-TPD)

For Chapter 2 & 3:

ChemBET Pulsar TPR/TPD automated chemisorption analyzer was employed to carry out NH$_3$-TPD. The sample was firstly flushed with a 20 ml/min pure He stream at 400 °C for 30 min. NH$_3$ was adsorbed onto the sample by passing a mixture of 50 % Ar – 50 % NH$_3$ and held for 15 -20 min. The stream was switched back to He for 30 min after NH$_3$ dosing. The intensity of desorbed NH$_3$ was recorded by progressively heating the sample up with a ramping rate of 20 K/min.

For Chapter 4:

NH_3-TPD was carried out on a micromeritics AutoChem II (Chemisorption Analyzer). Be-fore measurement, 50 – 70 mg catalyst were firstly flushed with 20 ml/min pure He gas stream at 400 °C for 30 min. Thereafter, NH_3 adsorption was performed by passing a 50 % NH_3 – 50 % Ar gas mixture at 100 °C for 20 min. To release physisorbed NH_3, the sample was subjected to a pure He gas at 100 °C for 30 min. Then, the data were collected by ramping the desorption tem-perature with a rate of 20 K/min.

Diffuse reflectance infra-red Fourier Transform (DRIFT) with pyridine adsorption

DRIFT-pyridine adsorption was conducted by Vertex-70 BRUKER. The catalyst was at first preheated to 400 °C under N_2 flow in 30 min to liberate the surface from any impurities. Having preheated, the catalyst was brought to 35 °C to record the background spectra and to allow pyridine adsorption. Pyridine was dosed by bubbling liquid pyridine with a N_2 flow leading via the sample chamber. The sample was saturated with pyridine for 15 – 20 min. The adsorbed pyridine was then partially removed in a N_2 flow by increasing the temperature to 150 °C for 20 min. For collecting the spectra of adsorbed pyridine, the sample was then cooled back to 35 °C.

Scanning tunneling electron microscopy (STEM)

Scanning transition electron microscopy (STEM) images were captured on Hitachi HD2700 microscope. The acceleration voltage was set to 200 kV. Prior to being measured, the sample was prepared by scooping dry powder with Cu/lacey carbon grid. The images were gen-erated from SE, ZC, and TEM detectors.

Esterification of levulinic acid with 1-butanol

LA and 1-butanol (1-BuOH) together with catalyst (10 wt.%) were introduced into a 100 ml two neck round bottom flask. The flask was then immersed into an oil bath, which

has been heated previously to the desired temperature. Vigorous stirring (750 rpm) was applied during the reaction. In order to do a time resolved experiment, the sampling was performed by withdrawing approximately 50 mg liquid product followed by quenching into an ice bath. The liquid product was then diluted with 15 mg/g diethylene glycol dimethyl ether (DGDME) as internal standard in 1,4-dioxane before GC analysis.

The product quantification was performed on Hewlett Packard 6890 GC series equipped with FID detector and a CP-Wax 52 column (60 m × 250 μm × 0.5 μm). The sample was carried by a N_2 flow with 1.5 ml/min and heated from 50 to 200 °C with a ramping rate 8 K/min. Two product peaks were observed in the chromatograms namely pseudo- (*p*-BL) and normal-butyl levulinate (*n*-BL). In the GC chromatogram, the peak related to LA shows a distinct tailing leading to inaccurate quantification resulting in slight underestimation of conversion. Therefore, the presented discussion is based on the observation of *p* and *n*-BL. No other products were detected in the reactions. Therefore, the selectivity of ($S_{n\text{-BL}}$) is evaluated according to the following equation:

$$S_{n-BL} = \frac{Y_{n-BL}}{Y_{n-BL} + Y_{p-BL}} \times 100 \%$$

$Y_{n\text{-BL}}$ and $Y_{p\text{-BL}}$ are defined as the yield of *n*-BL and *p*-BL. The specific catalytic activity is expressed as the turn over frequency (TOF) and based on the formation of products. As the reaction can even proceed without any presence of a catalyst, the total yield is normalized to obtained yields from the blank test at corresponding reaction times. The TOF will later be calculated as below:

$$TOF = \frac{(\frac{\Delta Y_T}{\Delta t}) \times C_{EST}}{C_{WO3}}$$

($\Delta Y_T/\Delta t$), C_{Est} and C_{WO3} are assigned to the normalized rate of esters production, total molar ester concentration per gram of product and WO_3 molar concentration per gram of catalyst, respectively.

Addition of alpha angelica lactone with alcohol

To carry out the reaction, a 50 ml three neck round flask equipped with a condenser was charged with LA (51 mmol), alcohol (51 mmol) and the catalyst (250 mg) under inert gas. The flask was soaked into a preheated oil bath and the mixture was agitated by a magnetic stirrer at 350 rpm. For a kinetic study, 50 mg product solution was withdrawn by a syringe and centrifuged to separate the solid catalyst from liquid products. The product was then diluted with 1,4-dioxane containing diethylene glycol dimethyl ether as internal standard. The identification of reaction products was confirmed by GC-MS analysis and compared with authentic samples. Furthermore, quantitative analysis was performed by GC-FID using a CP-wax-52 column (60 m × 250 μm × 0.25 μm). Qualitative analysis was performed by GC-MS on a Trace GC chromatograph 1310 equipped with a Restek Rxi-1 MS column (60 m × 250 μm × 0.5 μm) and a Thermo Scientific ISQ mass spectrometer (EI+, 70 eV, 250°C).

GC quantification

Substrate and product quantification was carried out using gas chromatography. Next the quantity of compound n is obtained as follows:

$$m_n = \frac{m_i \times A_n \times CF_n}{A_s}$$

Where:

m_n : mass of compound n in solution (mg/g)

m_i : mass of internal standard in solution (mg/g)

A_n : peak area of compound n

A_s : peak area of internal standard

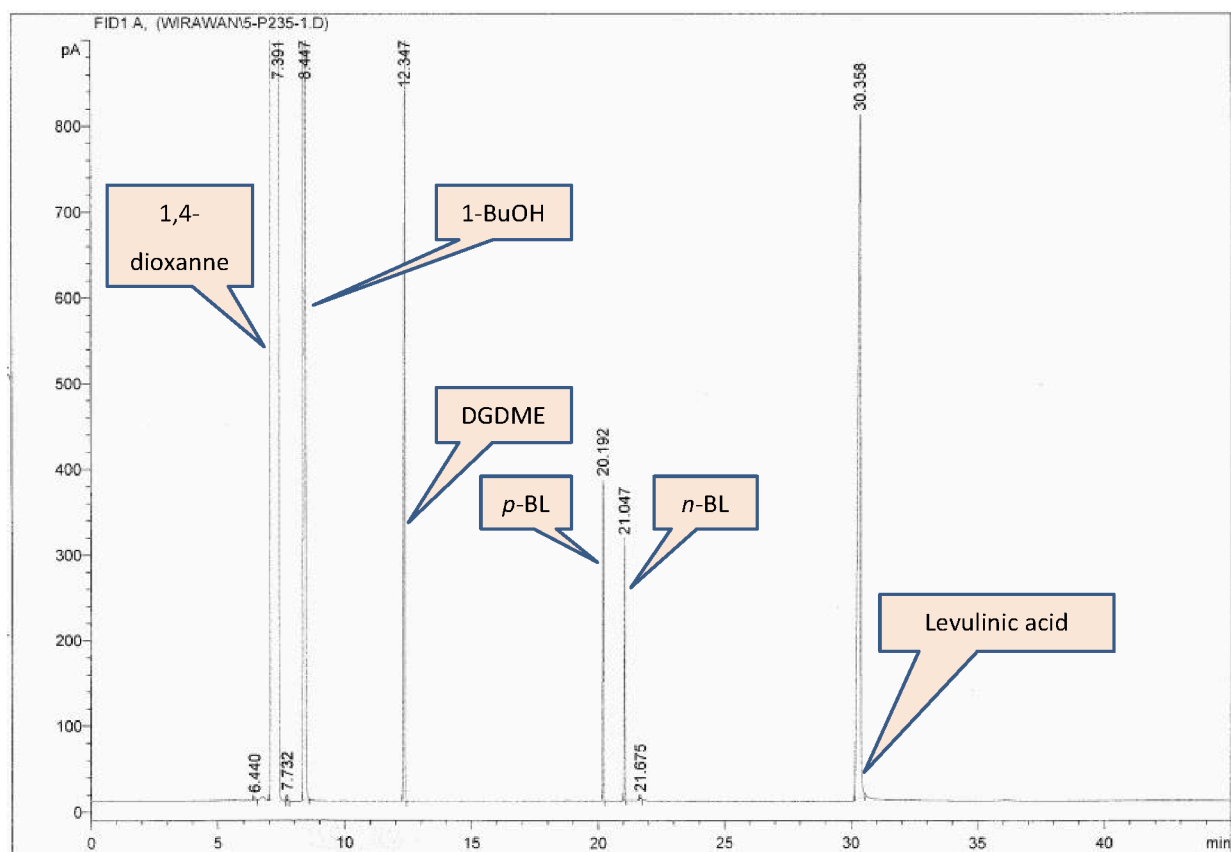CF_n : correction factor of compound n

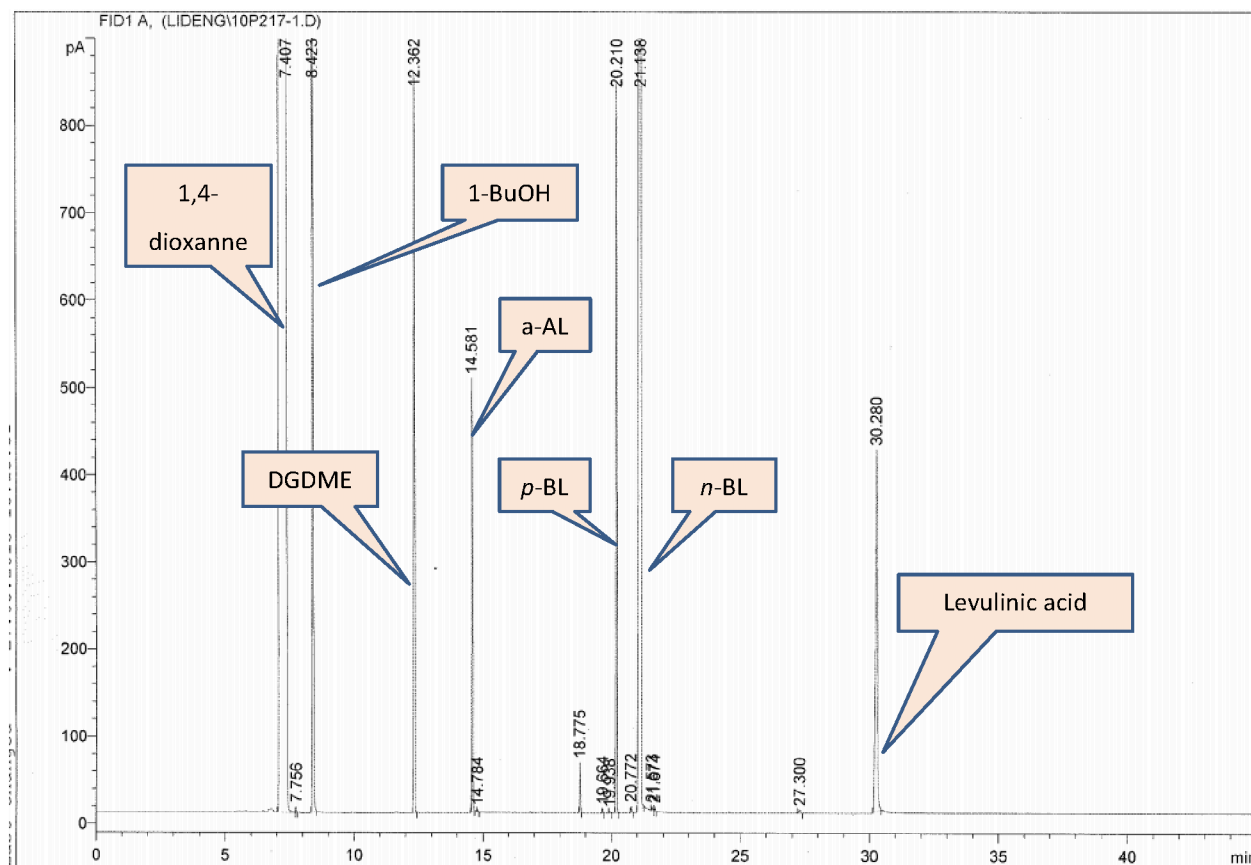Figure A1-1 Typical chromatogram of levulinic acid esterification

Figure A1-2 Typical chromatogram of a-AL addition with 1-BuOH

Appendix 2 Results

Determination of W surface density (ρ_W)

$$\rho_W = \frac{wt\%.\,WO_3 \times N_{AV}}{MW_{WO3} \times S_{BET}}$$

ρ_W : W surface density [W-atoms/nm^2]

N_{Av} : Avogadro number [$6.02 \cdot 10^{23}$ atoms/mol]

MW_{WO3} : molecular weight of WO_3 [g/mol]

S_{BET} : BET surface area [m^2/g]

Calculation for turn over frequency (TOF)
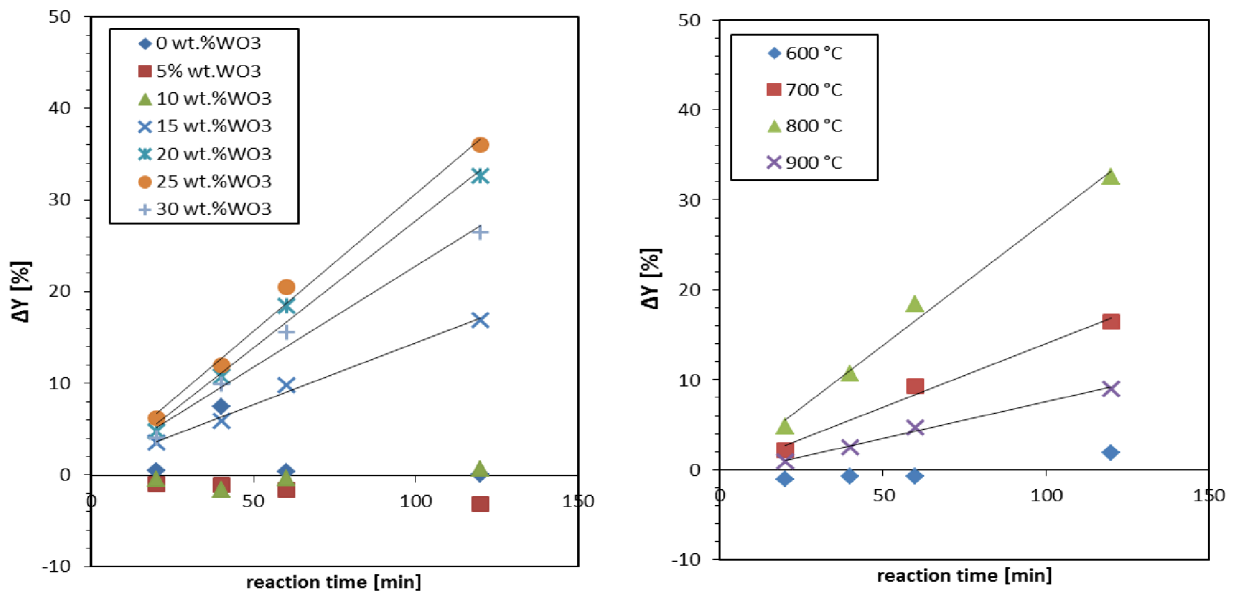
Figure A2-1 Determination of TOF$_{eff}$ of LA esterification with 1-BuOH

Kinetic modelling

In order to determine the kinetic constant, a mathematical model is firstly proposed. Because of the negligible formation of g-BL and relatively constant yield of LA throughout

the time, the considered system will only involve the consecutive transformation of a-AL to *n*-BL through which *p*-BL is generated as an intermediate. The irreversible reaction will be expressed as follows:

$$a - AL + 1 - BuOH \xrightarrow{k_1} p - BL \xrightarrow{k_2} n - BL \qquad \text{(Eq A2-1)}$$
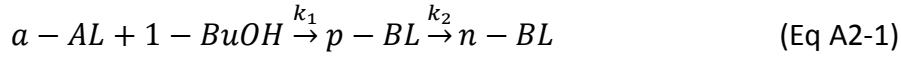
where a-AL, 1-BuOH, *p*-BL and *n*-BL represent α-angelica lactone, 1-butanol, pseudo- and normal-butyl levulinate and normal respectively. Based on Equation A2-1, the consumption and formation rate of corresponding compounds can be derived as follows:

$$\frac{d[a-AL]}{dt} = -k_1[a - AL][1 - BuOH] \qquad \text{(Eq A2-2)}$$

$$\frac{d[p-BL]}{dt} = k_1[a - AL][1 - BuOH] - k_2[n - BL] \qquad \text{(Eq A2-3)}$$

$$\frac{d[n-BL]}{dt} = k_2[n - BL] \qquad \text{(Eq A2-4)}$$

Furthermore, the reaction rates were solve by minimizing the sum square of the corresponding concentration obtained from the model and experimental data as demonstrated by Eq A2-5.

$$S = \sum_{i=1}^{n}(C_{exp-i} - C_i)^2 \qquad \text{(Eq A2-5)}$$

Where C_{exp-i} and C_i are assigned to the actual concentration from the experiment and predicted concentration from the model.

Kinetic profiles of a-AL addition over A-36 at different reaction temperatures
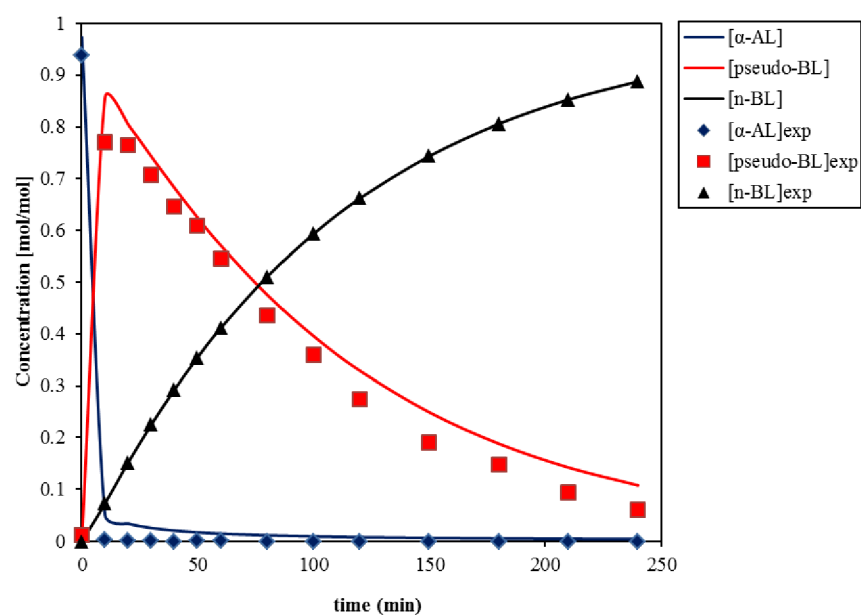
Figure A2-2 Kinetic of a-AL addition over A-36 at 50 °C
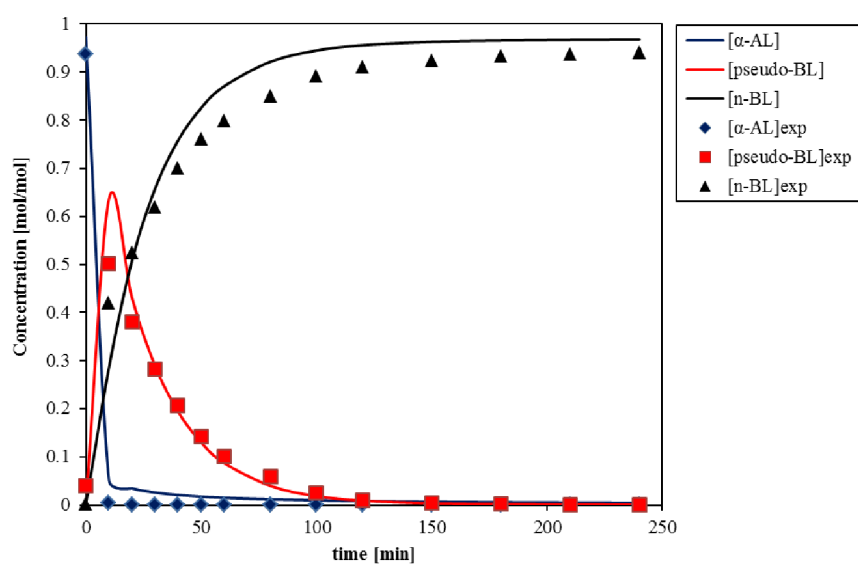
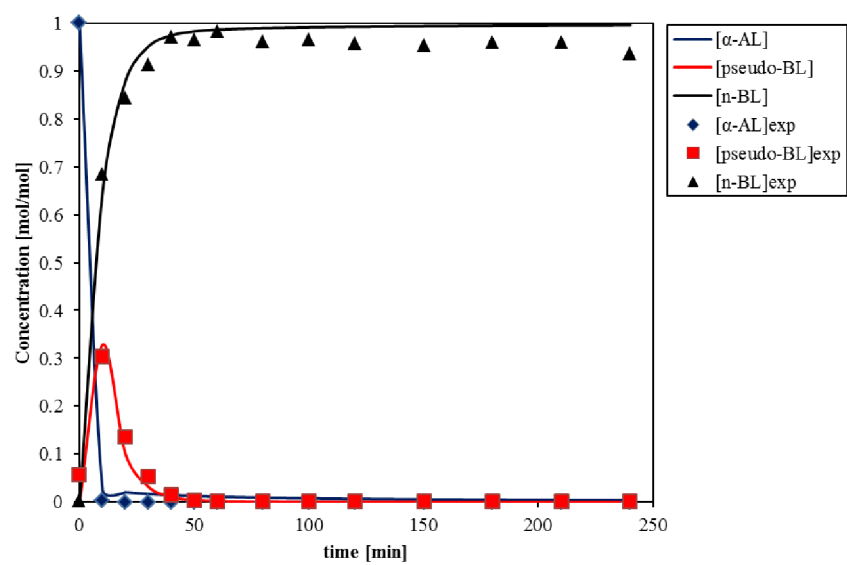Figure A2-3 Kinetic of a-AL over A-36 at 75 °C

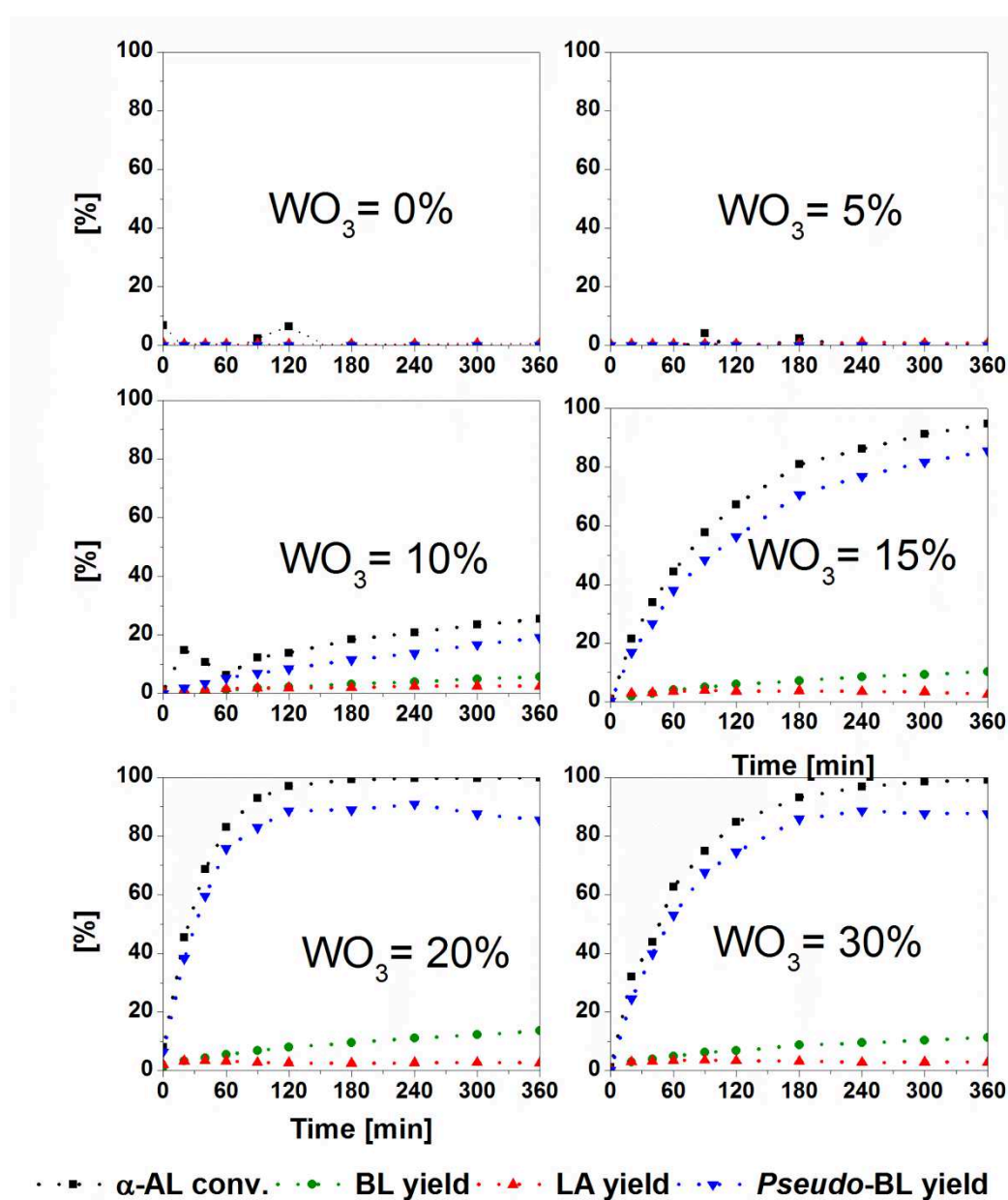**Figure A2-4 Kinetic of a-AL over A-36 at 100 °C**

Kinetic of a-AL addition over WO_3/ZrO_2 prepared via EISA

Figure A2-5 Kinetics of a-AL with 1-BuOH over WZr catalysts with different loadings prepared via EISA route. Reaction conditions: T = 75 °C, stirring rate = 350 rpm, and $R_{1-BuOH}/LA = 1$
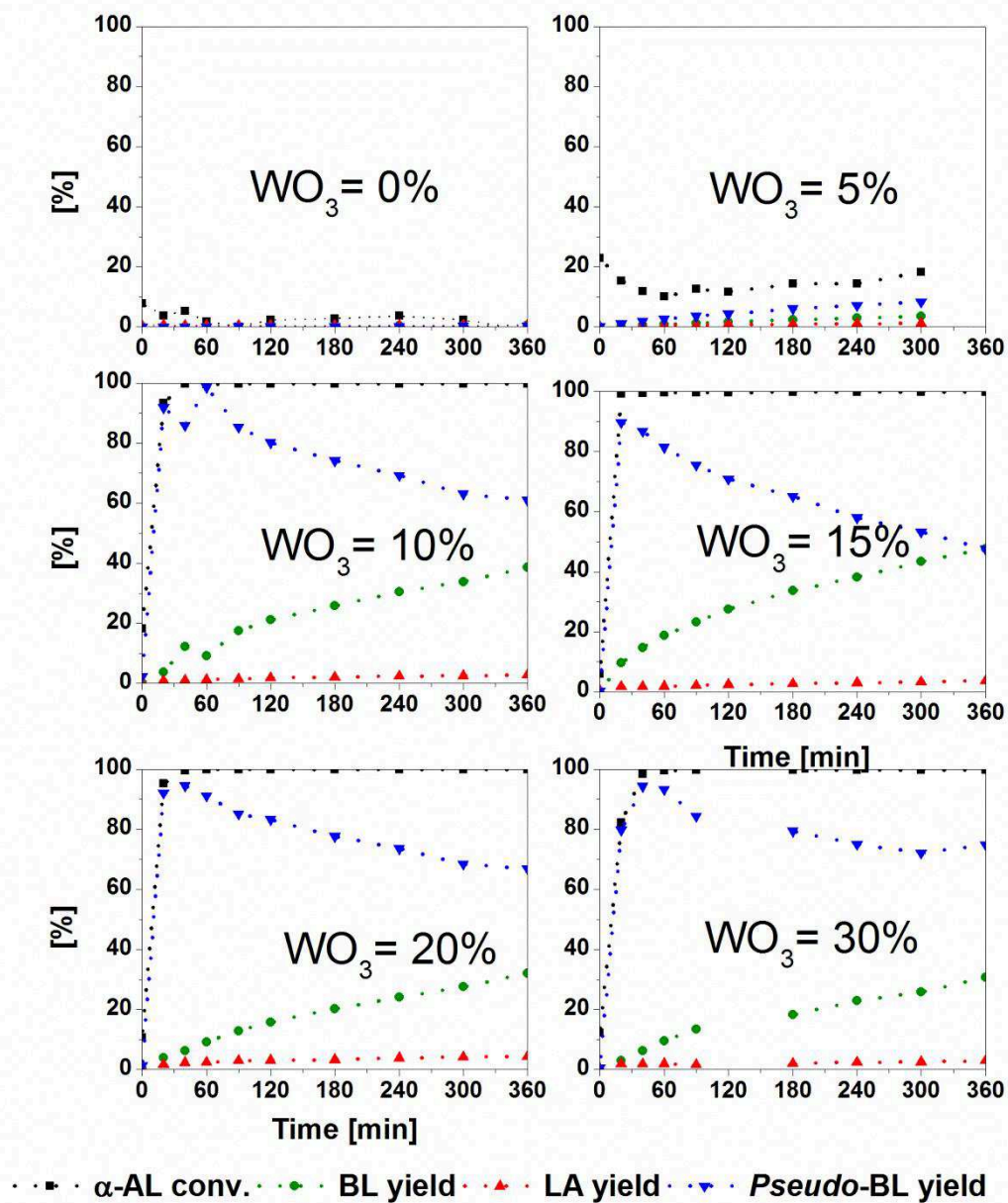
Kinetic of a-AL addition over WO$_3$/ZrO$_2$ prepared via impregnation

Figure A2-6 Kinetics of a-AL with 1-BuOH over WZr catalysts with different loadings prepared via impregnation method. Reaction conditions: T = 75 °C, stirring rate = 350 rpm, and R1-BuOH/LA = 1

List of Publications

1. W. Ciptonugroho, G. M. Al-Shaal, J. B. Mensah and R. Palkovits. One pot synthesis of WO_x/mesoporous-ZrO_2 catalyst for the production of levulinic-acid esters, J. Catal. 340 (2016) 17-29.
2. M. G. Al-Shaal, W. Ciptonugroho, F. J. Holzhäuser, J. B. Mensah, P. J. C. Hausoul, R. Palkovits. Catalytic upgrading of α-angelica lactone to levulinic acid esters under mild conditions over heterogeneous catalysts, Catal. Sci. Technol 5 (2015) 5168 - 5173
3. W. Ciptonugroho, J. B. Mensah, G. M. Al-Shaal and R. Palkovits. Catalytic conversion of α-angelica lactone - a potential biobased platform chemical - to levulinic acid esters over WO_x/ZrO_2, submitted in Appl. Catal. B: Environmental.
4. W. Ciptonugroho, R. Palkovits, Preparation of mesoporous-ZrO_2 and its application in the esterification of levulinic acid and butanol, Aachen 6th annual new year's symposium, Aachen (Germany), January 10th 2014 (poster contribution)
5. W. Ciptonugroho, R. Palkovits, One pot synthesis of WO_3/mesoporous-ZrO_2 as a potential catalyst for levulinic acid esterification, 6th International FEZA conference, Leipzig (Germany), September 8th 2014 (poster contribution)
6. W. Ciptonugroho, M. G. Al-Shaal, J. B. Mensah, R. Palkovits, Production of alkyl-levulinates over WO_3/mesoporous-ZrO_2 , the Netherlands catalysis and chemistry conference XVI, Noordwijkerhout (the Netherlands), March 2nd 2015 (poster contribution)
7. P. J. C. Hausoul, M.G. Al-Shaal, W. Ciptonugroho, C. Broicher, R. Vegliante, R. Palkovits, Application of Metallic and Molecular Heterogeneous Ru-catalysts for Biomass , 49. Jahrestreffen Deutscher Katalytiker, Weimar (Germany), March 16th 2016 (oral presentation)
8. W. Ciptonugroho, Joel B. Mensah, M. G. Al-Shaal, R. Palkovits, WO_x/ZrO_2 in the catalytic upgrading of α-angelica lactone to levulinic acid esters: structure-activity relationship, 17th Nordic Symposium on Catalysis 2016, Lund (Sweden) June 14th - 16th 2016 (poster contribution)

Curiculum Vitae

Wirawan Ciptonugroho was born in Jakarta, Indonesia on December 23rd 1983. Having accomplished his senior high school in 2002, he entered a bachelor program in chemical engineering at the Institut Teknologi Sepuluh-Nopember (ITS), Indonesia and graduated in 2007. In the last semester of his bachelor program, he joined the chemical reaction engineering laboratory to conduct his bachelor thesis which was related to the kinetic investigation of oleic acid esterification over acidic zeolites under supervision of Dr. Lailatul Qadariyah and Prof. Dr. Achmad Roesyadi. Afterwards, he was awarded a scholarship from the Taiwan government to pursue his master degree (M.Sc.) in chemical engineering from 2007 – 2009 at National Cheng-Kung University (NCKU), Taiwan. For his master thesis, he conducted research in the group of Prof. Dr. Dong-Hwang Chen developing a synthesis method for the preparation of Pt modified silicon nanowires for a photo-electrochemical application. Coming back to Indonesia in 2009, he was appointed as a junior lecturer at the chemical engineering department, Sebelas Maret University where he joined the research group of advanced materials led by Dr. Agus Purwanto. He then carried out his PhD research in the group of Prof. Dr. Regina Palkovits at the ITMC RWTH Aachen, Germany from September 2012 to October 2016. Starting from November 2016, he has been a postdoctoral researcher at BCI TU Dortmund working with Dr. Andreas J. Vorholt, Prof. Dr. Arno Behr and Prof. Dr. Dieter Vogt.